Crustal contamination recorded by zoned plagioclase in primitive Karoo flood basalts, Luenha River, Mozambique

Master's thesis

University of Helsinki

5/12/2018

Milla Aaltonen

Tiedekunta – Fakultet – Faculty	Laitos – Institution – Department
Faculty of Science	Department of Geosciences and Geography

Tekijä – Författare – Author

Milla Aaltonen

Työn nimi – Arbetets titel – Title

Crustal contamination recorded by zoned plagioclase in primitive Karoo flood basalts, Luenha River, Mozambique

Oppiaine – Läroämne – Subject

Geology

Työn laji – Arbetets art – Level	Aika – Datum – Month and year	Sivumäärä – Sidoantal – Number of pages
MSc. Thesis	12/2018	89

Tiivistelmä – Referat – Abstract

Jurassic (182 Ma) Karoo flood basalt province shows great variety in geochemistry. The complexity is thought to be inherited from distinct mantle sources. Luenha River exposure in northern parts of Mozambique includes primitive picrites possibly representing the still undefined parental magma type for the North Karoo Lavas. The previously determined whole-rock data revealed chondritic to very radiogenic $^{87}Sr/^{86}Sr$ ratios and nearly chondritic ε_{Nd} values. The diverse $^{87}Sr/^{86}Sr$ ratios can result from processes such as e.g. subsolidus alteration, contamination, magma mixing or source heterogeneities, which complicates assessment of petrogenetic processes.

To make a contribution to this, plagioclase phenocrysts from six Luenha samples were used as tracers of magma chamber processes. In situ studies on plagioclase growth zones were performed using the CIS methods (*crystal isotope stratigraphy*). Cold-cathode cathodolumenescence microscopy (CL) was used to visually reveal zonation, the electron microprobe (EMPA) was utilized for major element content (core-to-rim), and laser ablation-multicollector-inductively coupled plasma- mass spectrometry (LA-MC-ICP-MS) was used for in situ $(^{87}Sr/^{86}S)_i$ ratio measurements.

The anorthite content of plagioclase cores (n = 65) is $An_{65–90}$ and core to rim variations alternate between normal oscillatory to reverse zoning. Is situ isotope examination revealed isotopic disequilibrium in $(^{87}Sr/^{86}Sr)_i$ between phenocrysts (cores 0.70511–0.70671, n = 10; rims 0.70539–0.70709, n = 11) and bulk groundmass (0.70660–0.71061, n = 12). Plagioclase cores are always less radiogenic compared to whole rock (0.70690–0.71019), but internal variation within and between lava flows exists. Core-to-rim microsampling revealed four different $(^{87}Sr/^{86}Sr)_i$ evolution paths reflecting heterogeneous crystallization conditions.

An, open complex magma plumbing system with progressing contamination is the likely scenario. The relatively radiogenic plagioclase cores compared with the uncontaminated plume-like sample ($^{87}Sr/^{86}Sr$ 0.70410) indicate that contamination was ongoing prior to plagioclase crystallization and continued until eruption. Phenocryst migration between compositionally and thermally distinct reservoirs at crustal depths could explain the heterogeneous plagioclase (An and $(^{87}Sr/^{86}Sr)_i$) of Luenha picrites.

Avainsanat – Nyckelord – Keywords

Karoo flood basalts, Assimilation, Plagioclase phenocryst, Geochemistry, In situ, LA-MC-ICP-MS, Sr isotopes, Crustal fingerprinting

Ohjaaja tai ohjaajat – Handledare – Supervisor or supervisors

Arto Luttinen, Tapani Rämö

Säilytyspaikka – Förvaringställe – Where deposited

University of Helsinki

Muita tietoja – Övriga uppgifter – Additional information

Tiedekunta – Fakultet – Faculty	Laitos – Institution – Department
Matemaattis-luonnontieteellinen tiedekunta	Geotieteiden ja maantieteen laitos

Tekijä – Författare – Author

Milla Aaltonen

Työn nimi – Arbetets titel – Title

Kuorellisen kontaminaation tallentuminen vyöhykkeelliseen plagioklaasiin primitiivisissä Karoon laakiobasalteissa, Mozambikin Luenha-joella

Oppiaine – Läroämne – Subject

Geologia

Työn laji – Arbetets art – Level	Aika – Datum – Month and year	Sivumäärä – Sidoantal – Number of pages
Pro Gradu	12/2018	89

Tiivistelmä – Referat – Abstract

Jurakautinen (182 Ma) Karoon laakiobasalttiprovinssi on geokemialtaan erittäin heterogeeninen. Heterogeenisyyden on ajateltu olevan peräisin kahdesta toisistaan eriävästä vaippalähteestä. Mozambikin koillisosassa sijaitseva Luenha joen paljastuma sisältää primitiivistä pikriittejä, joiden koostumuksen ajatellaan edustavan toistaiseksi tuntematonta North Karoon kantamagmaa. Kokokivianalyysit paljastivat näiden pikriittien $^{87}Sr/^{86}Sr$ suhteen vaihtelevan kondriittisesta radiogeeniseen, ε_{Nd} arvot ovat lähes kondriittisia. Vaihtelevat $^{87}Sr/^{86}Sr$ suhteet voivat johtua kiteytymisen jälkeisestä muuttumisesta, kontaminaatiosta, magmojen sekoittumisesta tai lähteen heterogeenisuudesta, mitkä voivat vaikeuttaa petrogeneettisten prosessien ja olosuhteiden määrittämistä.

Tähän kysymykseen vastatakseni tutkin plagioklaasihajarakeita kuudesta Luenhan kivinäytteestä magmakammio-prosessien jäljittämiseksi. Plagioklaasin kasvuvyöhykkeitä tutkittiin CIS-metodeihin (kiteen isotooppi stratigrafia) sopeutuvilla in situ -menetelmillä. Kylmäkatodi katodoluminesenssi (CL) -mikroskoopiaa käytettiin vyöhykkeellisyyden kuvantamiseen, elektronimikroanalysaattoria (EMPA) pää-alkuaine pitoisuuksien määrittämiseen (ytimestä reunoille) ja multikollektorilla varustetulla laserablaatioon perustuvalla induktiivisesti kytketyllä plasmamassaspektrometrillä mitattiin in situ $(^{87}Sr/^{86}Sr)_i$ suhteet.

Plagioklaasihajarakeiden ytimien (n = 65) anortiittipitoisuus vaihtelee välillä An_{65-90} ja vyöhykkeellisyys ytimestä reunoille vaihtelee normaalista oskilloivaan ja käänteiseen. In situ Sr isotooppimittaukset paljastivat isotooppiepätasapainon initiaalisen $^{87}Sr/^{86}Sr$ suhteen osalta hajarakeiden (ytimet 0.70511–0.70671, n = 10; reunat 0.70539–0.70709, n = 11) ja perusmassan (0.70660–0.71061, n = 12) välillä. Plagioklaasin ytimet ovat kokokiven isotooppikoostumukseen nähden ($(^{87}Sr/^{86}Sr)_i$ 0.70690–0.71019) aina vähemmän radiogeenisia ja yksittäisten laavavirtojen välillä on hajontaa, joka ylittää mittaustarkkuuden. Mikrotutkimukset kiteiden ydinten ja reunojen välillä osoittavat kiteytymisolojen olleen hyvin heterogeeniset.

Progressiivinen kontaminaatio avoimessa ja kompleksisessa magmakammiosysteemissä voi selittää havaitut $^{87}Sr/^{86}Sr$ vaihtelut hajarakeiden ydinten välillä. Kontaminaatio vaikuttaa alkaneen ennen plagioklaasin kiteytymisen alkamista ja jatkuneen purkautumiseen asti. Lisäksi vuorovaikutusta primitiivisemmän koostumuksen sulan kanssa havaittiin. Luenhan pikriittien plagioklaasien pääalkuaine- ja Sr-isotooppi koostumukset voidaan selittää magmasysteemillä, jossa plagioklaasihajarakeet kulkeutuvat koostumuksen ja lämpötilan suhteen toisistaan eroavien magmakammioiden välillä kuoren syvyydellä.

Avainsanat – Nyckelord – Keywords

Karoo laakiobasaltit, Assimilaatio, Plagioklaasi hajarae, Geokemia, In situ, LA-MC-ICP-MS, Sr isotoopit, Kuorellinen sormenjälki

Ohjaaja tai ohjaajat – Handledare – Supervisor or supervisors

Arto Luttinen, Tapani Rämö

Säilytyspaikka – Förvaringställe – Where deposited

Helsingin yliopisto

Muita tietoja – Övriga uppgifter – Additional information

TABLE OF CONTENTS

1. INTRODUCTION

1.1. Continental flood basalts

Continental flood basalts (CFBs) are tremendous volcanic formations that form when millions of cubic kilometers of primarily low viscosity tholeiitic basalts erupt through fissure vents within a few million years or even less (Carlson 1991, Courtillot and Renne 2003, Silver et al. 2006). These basaltic flows often form stacks of individual lava flows called traps (*swe. trappa, eng. stairs*). One trap can reach a volume from 100 km^3 up to >1000 km^3 and thickness by the order of a kilometer while taking less than one million years to pile up (Carlson 1991, Courtillot and Renne 2003). CFBs spread across all modern continents creating extensive volcanic provinces (Fig. 1) that, together with oceanic plateaus (OPs), form large igneous provinces (LIPs). Despite of their wide existence, there is currently only a handful (~16) of identified Phanerozoic CFB provinces (Courtillot and Renne 2003).

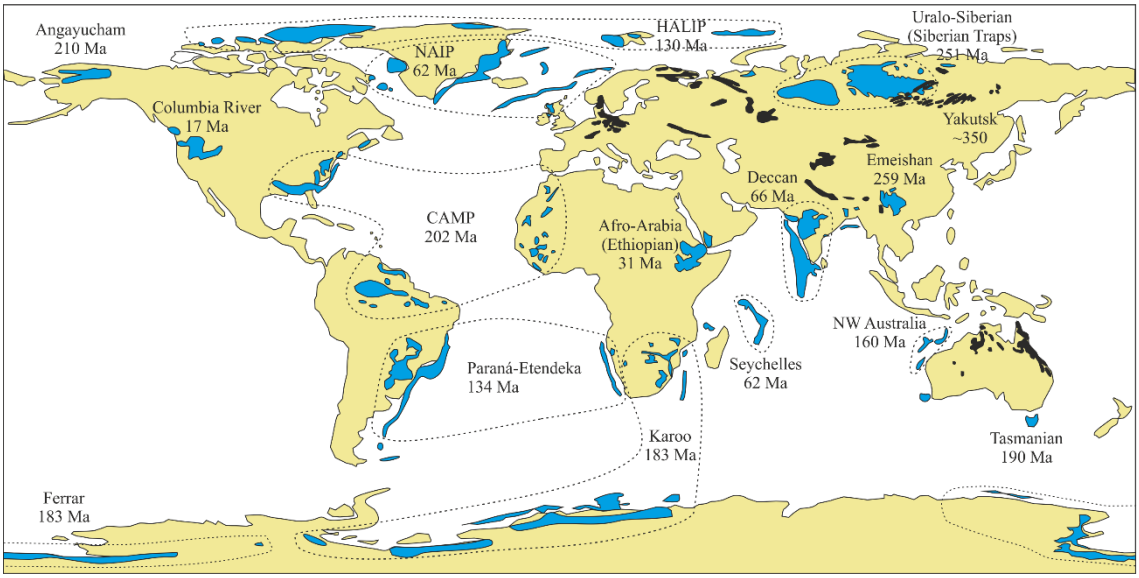

Figure 1. Phanerozoic continental flood basalts (CFBs) presented in current continental configuration after Bryan and Ernst (2008). Blue areas are Mesozoic to Cenozoic flood basalts and black areas are older Paleozoic flood basalts. Abbreviations: NAIP = North Atlantic Igneous Province, CAMP = Central Atlantic Magmatic Province, HALIP = High Arctic Large Igneous Province.

CFBs have erupted throughout the geological time and they seem to be temporally associated with the supercontinent cycle (King and Anderson 1995, Courtillot and Renne 2003). Whereas some CFB provinces are linked to successful continental breakups, others are related to rifting in stable craton without terminal breakup (Silver et al. 2006). The CFB magmatism is also considered as one of the possible causes to global-scale mass extinctions (e.g. Siberian traps for Permian-Triassic, Deccan traps for Cretaceous-Tertiary; Renne et al. 1995), mainly due to high amounts of aerosols forming from volatiles and dusts released into the atmosphere (Courtillot and Renne 2003). Despite extensive research inspired by the significant global-scale impacts, there is no common agreement on from where (e.g. ancient primitive mantle; Jackson and Carlson 2011) and how they originate (e.g. Anderson 1994). Multiple geodynamic models trying to explain CFB magmatism (Fig. 2) have been proposed during the last decades. The most significant models are reviewed below.

1.2. CFB models

The CFB models should be able to comprehensively explain the following physical constraints; a short duration (~1 Ma) of voluminous eruptions in continental breakup areas and in non-breakup cratonic areas (Silver et al. 2006), a relatively long-lasting magmatism of some provinces (e.g. Karoo flood basalt province; Jourdan et al. 2005), and the post breakup magmatism (e.g. Iceland; Meyer et al. 2007). Models presented for the CFB magmatism include: 1) high-temperature mantle plume (plume incubation; White and McKenzie 1989 and plume initiation; Richards et al. 1989) (Fig. 2); 2) thermal incubation of supercontinents (Anderson 1994); 3) two-stage drainage system (Silver et al. 2006, Fig. 2); 4) delamination (e.g. Meyer et al. 2007, Fig. 2); 5) meteorite impact (Rogers 1982); 6) small-scale rift-related, edge-driven convection (King and Anderson 1995, Fig. 2), and 7) high degree melting of heterogeneous mantle source (Korenaga 2004, Fig. 2).

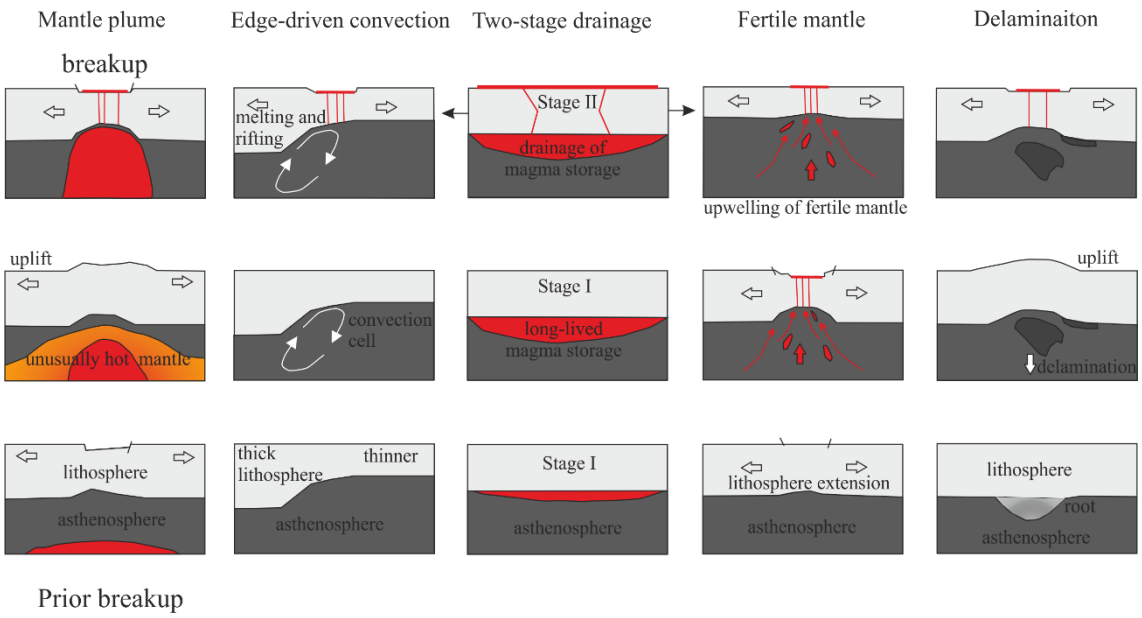

Figure 2. Five different geodynamic mechanisms for CFB magmatism. In the mantle plume model anomalously hot magma rises adiabatically from asthenosphere (White and McKenzie 1989, Richards et al. 1989). The edge-driven convection model of King and Anderson (1995) explains CFB magmatism by melting of mantle caused by convection cell between thinner and thicker lithosphere. In the two-stage drainage model of Silver et al. (2007), magma first pools under lithosphere (stage I) and then rapidly erupts (stage II). Melting of fertile mantle is caused by lithospheric extension and thinning (Korenaga 2004). In the lithosphere delamination models, base of the thick lithosphere becomes dense, detaches, and sinks into the mantle. This causes melting by decompression (e.g. Mayer et al. 2007). Modified after Silver et al. (2006) and Meyer et al. (2007).

None of the models have been able to provide an undisputable explanation for CFB magmatism. Short but voluminous melt production is not explained by the delamination model (e.g. Meyer et al. 2007) and the presence of xenoliths from sub-continental lithospheric mantle (SCLM) in many CFBs does not support this model (Silver et al. 2006). The heterogeneous mantle source model (Korenaga 2004) could explain the versatility in the CFB geochemistry by high degree melting of subduction modified fertile mantle sources, but falls short in explaining the brief period of volcanism (e.g. Meyer et al. 2007). Small-scale rift-related convection between thicker Archean craton lithosphere and thinner lithosphere causes mantle material to melt and is capable of producing LIP scale outpourings of melt (King and Anderson 1995). Although geodynamic modelling of melt production rates supports the small-scale convection model (King and Anderson 1995), the short duration of eruption events is not explained (Meyer et al. 2007). Thermal insulation beneath supercontinents model suggested by Anderson (1994) is questioned by laboratory tests and modelling problematics (Lenardic et al. 2011). The two-stage drainage model of Silver et al. (2006), in which magma is rapidly released from long-term sub-lithospheric magma storage system, was presented to explain rapid magmatism

of cratonic CFBs with thick lithosphere. Evidence of supersolidus state in the lithospheric mantle and heat source are questionable (Silver et al. 2006). Extraterrestrial meteorite impacts are not commonly supported in lack of tectonic evidence of impacts and problematics in geodynamic modelling of melt production (Meyer et al. 2007).

A high-temperature, mantle plume has long been the main explanation for the origin of CFBs. The theory was first introduced by Morgan (1971) and has been adopted by numerous researches since (e.g. Richards et al. 1989, White and McKenzie 1989, Campbell and Griffiths 1990, Beccaluva et al. 2009). One of the most long-lived hypotheses is the plume incubation model by White and McKenzie (1989), which explains flood basalt magmatism with a thermal anomaly caused by a mantle derived plume and passive rifting of the lithosphere, with simultaneous adiabatic decompression melting of mantle. Instead, the plume initiation model of Richards et al. (1989), suggests that the fast onset for rapid magmatism of CFBs is caused by a hot plume head, which melts via decompression when introduced to upper mantle. No pre-plume rifting is required as in the plume incubation model (but can be a consequence of it) and the volume of CFB is comparative with the size of the plume head (Richards et al. 1989). Based on spatial distribution of geochemically variable rock types, the plume incubation model is more prominent for CFB provinces than the plume initiation model (Kent et al. 1992).

Arguments against the plume model have been proposed. Regional hotspot relations with CFBs supports the plume sources (Carlson 1991). Many CFB provinces, however, lack a hotspot connection, or conversely, many hotspots are not accompanied with CFB provinces (King and Anderson 1995). The plume theory also struggles to explain the rapid ~1 Ma melt production in areas with thick cratonic lithosphere (King and Anderson 1995). Some questions have also been raised about the plumes as the driving force of extended magmatism in some provinces (Carlson 1991).

Many potential alternative hypotheses have been issued, yet none of the non-plume theories are able to explain the high rate production of basaltic melts and the continuing post-breakup melt production (Meyer et al. 2007). Thus the origin for their major magmatic events still remains controversial.

In addition to the aforementioned physical features, CFB provinces show a wide distribution in isotope and incompatible element compositions between provinces and within a single province (Carlson 1991). On the one hand, the geochemical similarities between oceanic island basalts (OIBs) and some CFBs imply a deep mantle plume related source, and slight differences could be explained by contamination by continental crust (e.g. Arndt et al. 1993, Beccaluva et al. 2009). On the other hand, certain geochemical features (e.g. low Nb/La, Sr, Nb, and Pb isotopes; Peate and Hawkesworth 1996) of many CFBs are not OIB-like (Coffin and Eldholm 1994), but correspond to a mean value of oceanic and continental sources (Pik et al. 1999). Whether this compositional similarity to crust stems from a source originating from SCLM or from efficient crustal contamination is an outstanding question (e.g. Greenough et al. 1989, Arndt et al. 1993, Lightfoot et al. 1993, Coffin and Eldholm 1994, Peate and Hawkesworth, 1996).

1.3. Unveiling contamination

Fractional crystallization of mantle- derived magmas (OIB or SCLM) alone is not capable of generating the geochemical heterogeneities in CFBs, therefore AFC (assimilation-fractional crystallization; DePaolo 1981) processes are needed. The geochemistry of many CFBs is strongly affected by contamination during magma ascent through relatively cool and thick continental lithosphere, exposing magma to contamination (e.g. Carlson et al. 1981, Ginibre and Wörner 2007, Jackson and Carlson 2011). Contamination signature in flood basalts can be studied by isotope, major element and trace element compositions (e.g. Davidson et al. 1998, Ramos et al. 2005). AFC processes probably have only a mild influence on major element composition, whereas trace elements are strongly affected (Taylor 1980). Thus, in order to unveil contamination, the most useful parameters are the contamination-sensitive incompatible elements and respective initial isotope ratios.

Isotopes are the fingerprints of the end-members involved in an igneous system (Davidson et al. 1998) as radiogenic isotopes do not fractionate during crystallization and thus are a powerful tool for the study of open magma chamber processes (Allègre 2008). The commonly used heavy radiogenic isotope systems (e.g. $^{87}Sr/^{86}Sr$, $^{143}Nd/^{144}Nd$, $^{207}Pb/^{206}Pb$) are based on incompatible elements and therefore pursue in melt phase during partial melting. For example, Rb is more incompatible than Sr and preferably goes to melt

generating Rb-enriched melts compared to Sr (higher Rb/Sr ratio). Parent isotope ^{87}Rb radioactively decays into radiogenic ^{87}Sr and leads to higher $^{87}Sr/^{86}Sr$ ratios over time. Hence, as older continental crust is enriched in Rb and consequently has notably high $^{87}Sr/^{86}Sr$ ratios, thus is the sedimentary detritus from therm (Taylor 1980).

Isotope ratios of a magma change when material with different $^{87}Sr/^{86}Sr$ ratios is added. Replenishment of new mafic magma usually is less evolved (low Rb/Sr), whereas crustal fragments, introduced to host magma via bulk assimilation or mixing of partial melts from wall rocks, have high Rb/Sr (e.g. Faure and Powell 1972, Andrews et al. 2008). The isotope equilibration assumption also allows isotopes to exchange between members without any material assimilation (kinetic phenomena), especially between high temperature liquids (Allègre 2008).

Contamination fingerprints have generally been examined using whole-rock data that represents the average chemical composition of erupted magma. Instead, in situ methods provide information prior to the eruption by studying minerals that crystallized in the preceding magma chamber, revealing details of the magma system prior to eruption.

1.3.1. Whole-rock approach to contamination

In search of ample precision, the majority of Sr isotope measurements have been conducted utilizing the thermal-ionization mass spectrometry (TIMS) on whole-rock or mineral separates (Jochum et al. 2009). This method provides only the bulk data of the rock building components (e.g. phenocrysts ± groundmass), and thus is not able to obtain information recorded within individual crystals during crystallization, complicating the reconstruction of petrogenetic events (Ramos et al. 2005, Browne et al. 2006).

1.3.2. In situ approach to contamination

In the crystal isotope stratigraphy (CIS), the isotope ratios are measured from growth zones of a crystal from core-to-rim. According to Davidson et al. (1998), the preferable conditions to perform CIS for selected mineral need to accomplish two major conditions: firstly, the selected mineral must be large enough for core-to-rim measurement and recommendable sampling size must be small enough for analysing individual zones; secondly, mineral should have a high enough ratio of the isotope in question for sufficient

precision. In situ methods suitable for CIS studies, such as laser ablation multi-collector inductively coupled mass spectrometry (MC-LA-ICP-MS) (Ramos et al. 2004, Borges et al. 2014) or microdrilling (Tepley et al. 1999, Tepley and Davidson 2003, Ginibre and Davidson 2014) enable examination of specific Sr bearing minerals in interest with ample precision and accuracy (Davidson et al. 1998, Ramos et al. 2004, Munoz et al. 2016).

Crystallizing minerals can effectively record isotopic changes in magma composition, if the parent or daughter isotope is compatible in the crystal lattice of the precipitating phases (Faure and Powell 1972, Rollinson 1993). Consequently, isotope fingerprints of differentiation events (tied to specific end-members) are recorded within progressive growth zones of crystals in the system (i.e. no isotopic re-equilibration between solid crystal zones takes place afterwards), or as inclusions within crystals reflecting growth in an open system (Davidson et al. 1998, Tepley et al. 1999).

Considering whole-rock data with in situ analyses, can produce more information of open system processes through the lithosphere (Font et al. 2008). Continental crust, depleted mantle (DM), enriched mantle (EM) and SCLM can contribute to magmatism in a single CFB system (Arndt et al. 1993). The mission is to evaluate whether the isotopic composition represents the mantle source, or whether the contamination fingerprint is inherited *en route* through lithosphere to surface (Carlson 1991). It is important to take into account that isotopic and trace element "crustal" signatures can traverse to the mantle source from earlier subduction processes (Lightfoot et al. 1993, Anderson 1994).

1.4. Plagioclase composition as a tracer for magmatic evolution

Major differentiation events have widespread influence on plagioclase texture and composition (Tepley et al. 1999). Differentiation processes have been studied based on plagioclase phenocrysts using combined high resolution geochemical analysis with petrographic observations (e.g. Davidson and Tepley 1997, Davidson et al. 1998, Tepley et al. 1999, Tepley and Davidson 2003, Browne et al. 2006, Ginibre and Wörner 2007, Andrews et al. 2008, Churikova et al. 2013, Ginibre and Davidson 2014). The composition of plagioclase is usually expressed by anorthite content [An = Ca/(Ca+Na) mol.%], which can be used as an indicator of changing magma composition during

crystallization and temperature-pressure-H_2O-conditions. Plagioclase crystals can nucleate at high temperatures and remain stable during cooling (e.g. Davidson et al. 1998, Tepley et al. 1999, Tepley and Davidson 2003) under different pressure-H_2O conditions (Housh and Luhr 1991). The slow diffusivity in the Ca^{2+}, Al^{3+} versus Na^{+}, Si^{4+} exchange (Grove et al. 1984) and Sr isotopes makes it possible to capture the original composition of magma into the progressive plagioclase growth zones. Sr^{2+} is highly compatible in the crystal lattice of plagioclase (Faure and Powell 1972, Rollinson 1993). Furthermore, plagioclase phenocryst are not fractionated from primitive picritic melts and thus they may store the original Rb/Sr ratios of the source in crystal cores (Cox 1988), offering a great control point for more comprehensive understanding of magmatic differentiation processes.

1.5. Case study – Karoo CFB province

The Jurassic Karoo CFB province is characterized by a great diversity of magma compositions and the province is divided into two sub-provinces with differing geochemical features (Luttinen 2018). The North Karoo and South Karoo sub-provinces are thought to be derived from distinct sources (Luttinen 2018) but the complexity of magma types and probable interaction with lithospheric crust presents an outstanding problem.

The Luenha River area in the northern part of the Karoo is a relatively new sample site situated in Mozambique in the North Karoo sub-province. Pre-existing whole-rock isotope studies on the Luenha lavas revealed a pronounced variety in $(^{87}Sr/^{86}Sr)_i$ with close to chondritic ε_{Nd} values (Turunen 2015). Geochemical comparison suggests that the Luenha lavas may represent an important parental magma type for the North Karoo sub-province (Turunen 2015). Thus, understanding the origin of variably in radiogenic strontium in the Luenha lavas could unveil more of the North Karoo magmatic evolution. Differentiation processes complicate the characterization of the primary magma composition, but can be documented as changing isotope compositions of strontium in plagioclase (e.g. Foland et al. 2000, Ramos et al. 2005).

In this study, I examined plagioclase phenocrysts in picritic rocks (180 Ma) from the Luenha River, Mozambique. The aim was to execute in situ measurements on the plagioclase phenocrysts and the enclosing groundmass in order to investigate the processes that affected the Sr isotope composition during the magmatic evolution of the Luenha picrites. The $(^{87}Sr/^{86}Sr)_i$ ratios in Luenha picrites may be the consequence of subsolidus alteration after eruption. Alternatively, radiogeneity could be magmatic, affected by contamination, or inherited from distinct sources (source heterogeneities).

The in situ $^{87}Sr/^{86}Sr$ determinations of the plagioclase phenocrysts and groundmass of this study provide new, significant and more precise data. The measured plagioclase core ratios record the isotopic composition of the magma at plagioclase liquidus conditions and provide new insights into primary magma composition of Karoo in Mozambique.

2. GEOLOGICAL SETTING

2.1. Karoo CFB province

The Jurassic Karoo LIP is one of the most extensive igneous provinces extending for over 4000 km from southern Africa to northern Antarctica in Gondwana reconstructions (e.g. Courtillot and Renne 2003, Fig. 3). It is considered to be associated with the first stages of the break-up of the supercontinent, which led to the opening of the southern Indian Ocean (e.g. Cox 1988). The Karoo CFB magmatism (184–174 Ma; Duncan et al. 1997, Jourdan et al. 2007c) produced mainly low-MgO basaltic lavas, sills, and giant dyke swarms, along with subordinate high-MgO picrites and felsic lavas and intrusive rocks (Cox 1988, Jourdan et al. 2007a). Currently the Karoo basalts cover an area of $< 3\times10^6$ km^2 (e.g. Jourdan et al. 2007a) and it has been estimated that the total volume originally reached 2.5×10^6 km^3 (Courtillot and Renne 2003). At present, most of the tholeiitic Karoo CFB are exposed in Botswana and Lesotho (Peyve 2015), and along the Lebombo monocline (Fig. 3). The majority of magmatism occurred between 178 and 184 Ma (Jourdan et al. 2005) with duration of ~3.0 to 4.5 Ma for the peak basaltic magmatism (Jourdan et al. 2007b). The bulk of the magmatism occurred at 183 ± 1 Ma, prior to the rifting of Gondwana (Duncan et al. 1997).

The Karoo province is described with an extensive variety of rock types. The rock types of the Africa rifted margin consist of a variety of nephelinites, picrites, low-Ti and high-Ti basalts and rhyolites (Lebombo-Mwenezi-Save monocline), whereas chiefly homogenous tholeiitic basalts were erupted in southern Africa, Namibia, Lesotho and Botswana (Duncan et al. 1997).

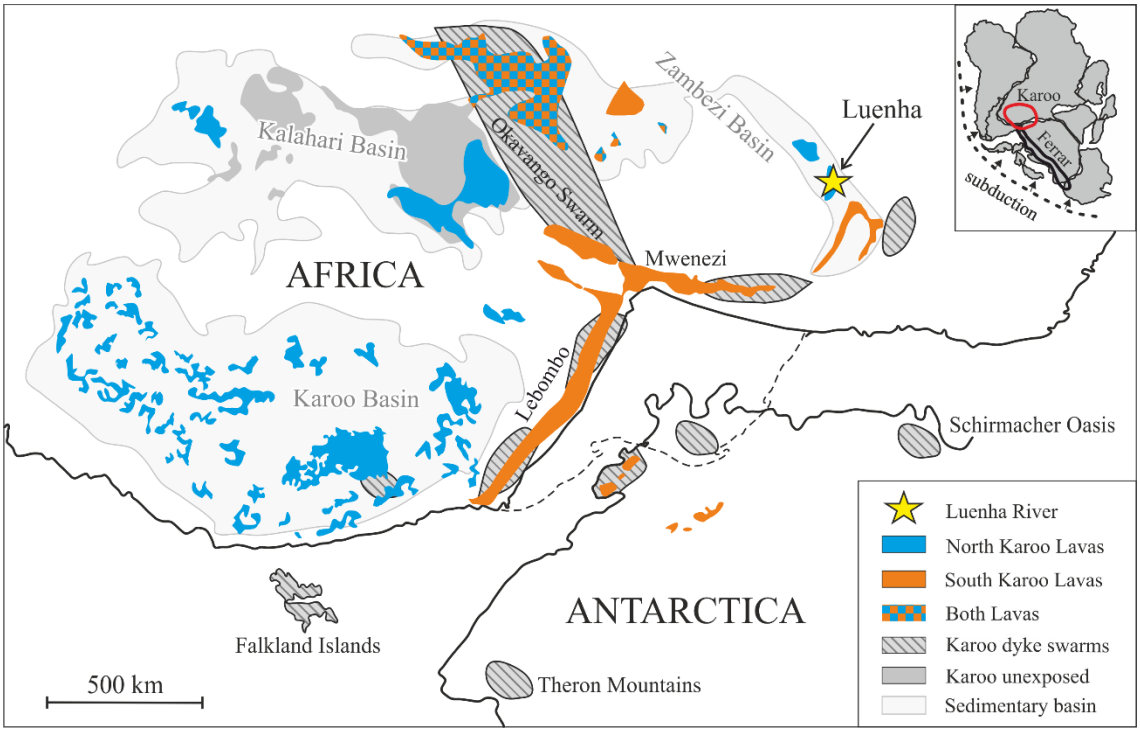

Figure 3. Karoo continental flood basalt province prior to the break-up of supercontinent Gondwana (inset). Volcanic products are categorized according to the latest division by Luttinen (2018) into the North Karoo Lavas with positive ΔNb and South Karoo Lavas with negative ΔNb. Yellow star marks the Luenha River exposure in current Mozambique.

2.1.1. Karoo provinciality

Conventionally, the Karoo flood basalts have been divided into low-Ti and "enriched" high-Ti lavas (Cox et al. 1967, Cox 1988). High-Ti lavas are strongly enriched, with high TiO_2 (> 2wt.%) and P_2O_5 and elevated K_2O and incompatible trace element concentrations, (e.g. Hawkesworth et al. 1986, Cox 1988, Jourdan et al. 2007a). Low-Ti lavas, on the contrary, are mildly enriched, having low TiO_2 (< 2wt.%) and P_2O_5 content with minor amounts of K_2O (e.g. Hawkesworth et al. 1986, Cox 1988, Jourdan et al. 2007a). Both low-Ti and high-Ti lavas show notably wide ranges of Nd and Sr isotopic compositions (e.g. ε_{Nd} from +9 to -18; Luttinen 2018).

Recently, Luttinen (2018) emphasized that the range in low-Ti and high-Ti compositions largely stem from magmatic differentiation processes and proposed a new division based on ΔNb (logarithmic plot of Nb/Y vs. Zr/Y; Fitton et al. 1997) values. Bimodally distributed ΔNb values divide the Karoo province into the North Karoo (positive ΔNb) and South Karoo (negative ΔNb) sub-provinces (Fig. 3). The bimodality in the ΔNb values is expected to originate from two different mantle sources (Luttinen 2018).

2.1.2. Source heterogeneities

Heterogeneous picrite compositions of the South Karoo sub-province have led to distinct interpretations for the mantle sources. Arndt et al. (1993) and Jourdan et al. (2007a) suggested that the high-Ti lavas originated below thick lithosphere. These high-Ti picrites formed when mantle derived melt assimilated subducted lithospheric material (Heinonen et al. 2014, Kamenetsky 2017) or by partial melting of hybrid source composed of SCLM and plume (Sweeney et al. 1991, Ellam et al. 1992, Jourdan et al. 2007a). The low-Ti lavas are considered to be the result of high-grade melting at the spinel-lherzolite stability field at shallow depths under thinner lithosphere (e.g. Jourdan et al. 2007a). For the origin of low-Ti lavas Jourdan et al. (2007a) propose metasomatically enriched SCLM mixed with mantle plume, however, the negative ΔNb-values are best explained by melting of Nb-depleted upper convective mantle (Luttinen 2018).

The North Karoo, which consist of low-Ti tholeiites with positive ΔNb-values, can be associated with a Nb-undepleted mantle origin (Luttinen 2018). The compositions of the least contaminated North Karoo low-Ti basalts suggest of a plume source (Peyve 2015, Luttinen 2018). The geochemical fingerprints of most low-Ti Karoo basalts (negative Ta and Nb anomaly, high $^{87}Sr/^{86}Sr$ ratios) could be inherited as the result of notable incorporation of upper crust (Lightfoot et al. 1993, Luttinen et al. 2015). Luttinen (2018) has pointed out that the low-Ti magmas belonging to the North Karoo (Fig. 3) were generated from different sources than the low-Ti magmas of South Karoo, however.

According to Peyve (2015) the duration of cratonic Karoo magmatism is atypical for a plume model and, for example, the small-scale edge-driven convection model of King and Anderson (1995) is considered plausible for the Karoo where ancient subduction in southwest Gondwana supercontinent (Fig. 3 inset) could supply the enriched signatures

of the sub-provinces without a plume or SCLM contribution. This could affect the composition of the South Karoo, but not the North Karoo, which is farther away from the subduction site (Luttinen 2018).

2.2. Luenha River picrite lava outcrop

Luenha River is situated in northwestern Mozambique, nearby the province of Tete (Fig. 4). Piles of mafic Karoo volcanites overlie a sedimentary basin covering Archean basement (Fig. 5). The bedrock in the province of Tete compose of Archean gneiss, mafic to ultramafic Neoarchean to Neoproterozoic intrusions, Mesoproterozoic supracrustal metamorphosed rocks and minor Neoproterozoic rocks, covered by Phanerozoic Karoo Supergroup rocks, volcanics and Cretaceous sediments (Pekkala et al. 2008).

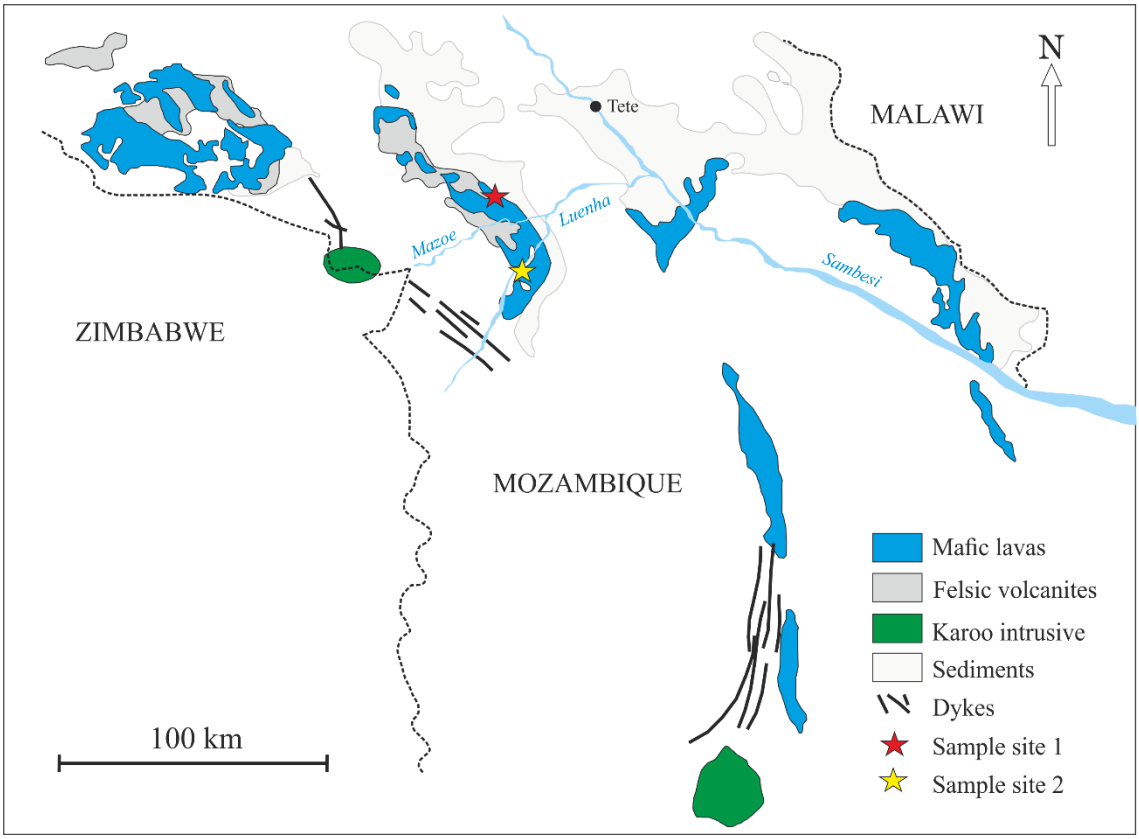

Figure 4. Simplified geological map of northwestern Mozambique. The Luenha sample sites of this study are marked with star symbols. Sample site 1 is for one separate sample AL-T042 north from Mazoe River, and Sample site 2 is for basalt sequence of samples AL-T026C to ALT026G. Modified after Manninen et al. (2008) and Turunen (2015).

The basalt sequence examined in this study is marked with star-symbols in Figure 4: Sample site 1 for a road cut exposure (sample AL-T042) and Sample site 2 for the main exposure (samples AL-T026C−AL-T026G). Slightly dipping 2−15 m thick lava flows in the surrounding of Rio Mazoe and Luenha River are fine-grained featuring pipe amygdules and ropy structure and other internal and surface structures typical to CFBs (Manninen et al. 2008).

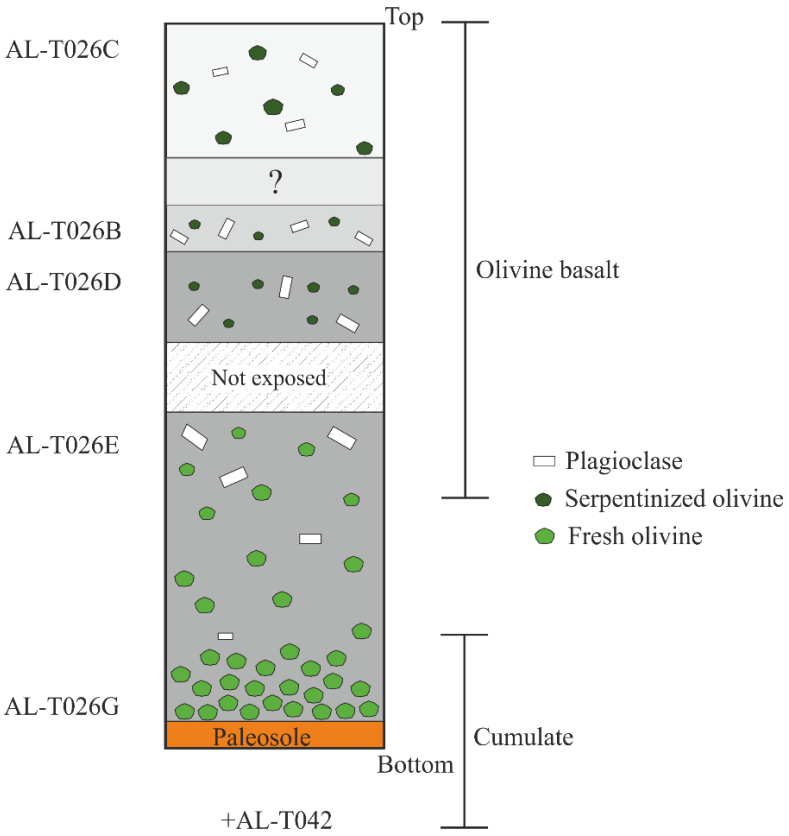

Figure 5. The stratigraphy of Luenha picrites (Sample site 2 in Fig. 4) and the one picrite sample from Mazoe road cut exposure AL-T042 (sample site 1 in Fig. 4). The field relations of Sample site 1 and 2 are unknown and therefore sample AL-T042 is not included in the stratigraphy. Bottoms contacts of lava units commonly have pipe vesicles and flow top contacts are vesicle-rich. The total thickness of the lava sequence is about 60 m. Modified after Turunen (2015).

Stratigraphy of the lava succession (Sample site 2) is present in Figure 5. Luenha lavas lay on paleosole and the stratigraphic units are slightly tilted. The distance between samples AL-T026C and AL-T026G which represent the topmost and lowermost samples in the Luenha River outcrop (Turunen 2015). The total thickness of the lava sequence is about 60 m and the thicknesses of individual flows range from 1m (AL-T026B) to 40 m (AL-T026G) (Turunen 2015). Most flows have pipe amygdules at the bottom contacts

and vesicle-rich flow tops. Northward from Sample site 2 is the road cut Sample site 1 from where sample AL-T042 is from. Field relation of the site 1 is unknown (Turunen 2015). All the flows have the same porphyritic anhydrous mineralogy consisting of olivine, plagioclase, clinopyroxene, and spinel and Fe-Ti oxides as accessory phases. Mineral abundances, groundmass textures and extent of alteration are slightly different between different flow units and are shortly explained in Samples-section.

2.2.1. Geochemical features of Luenha picrites and interpretation of mantle source

Highly magnesian Luenha picrites were studied by Turunen (2015). These examinations showed that some of the high MgO picrites are olivine cumulates but the others represent primitive picritic melt compositions with minimal fractionation. Whole-rock analysis of major element compositions, trace-elements and isotopes unveiled that the Luenha picrites have chondritic REE (rare earth elements) concentrations, chondritic to highly radiogenic $(^{87}Sr/^{86}Sr)_i$ ratios (Table 1) with nearly chondritic $(\varepsilon_{Nd})_i$ (+1.9 to -0.7) (Fig. 6).

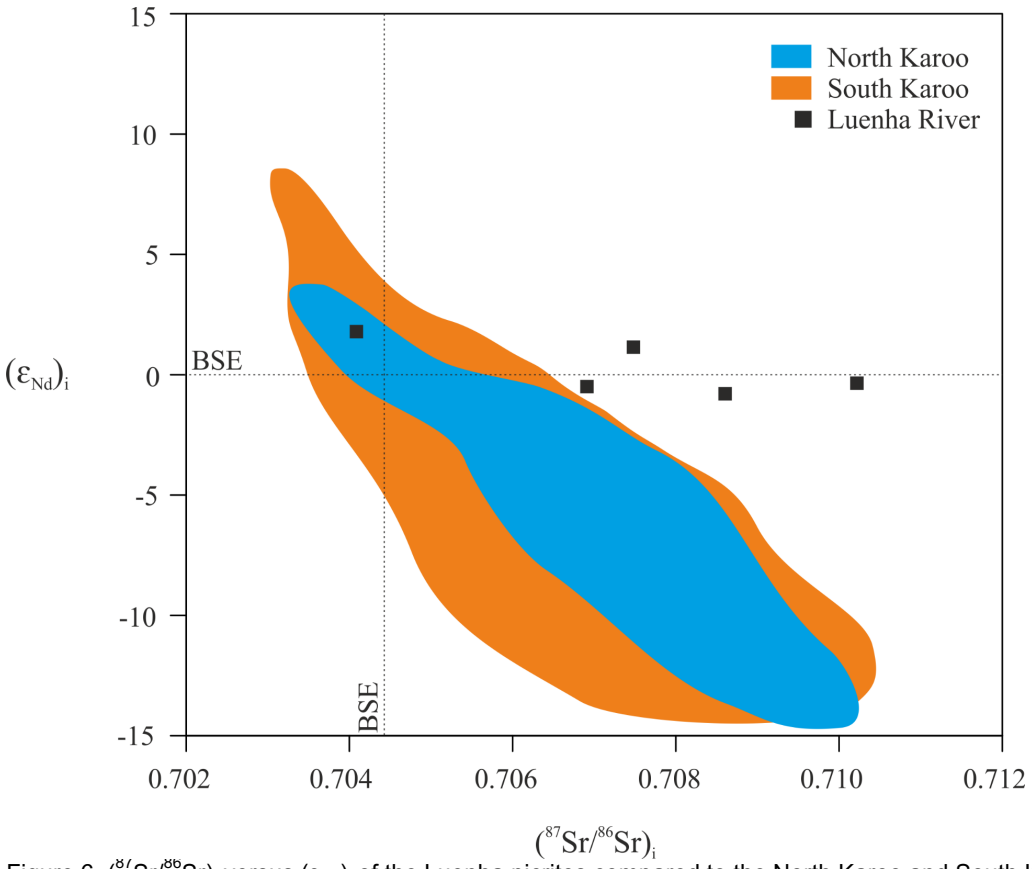

Figure 6. $(^{87}Sr/^{86}Sr)_i$ versus $(\varepsilon_{Nd})_i$ of the Luenha picrites compared to the North Karoo and South Karoo sub-provinces. The whole-rock $(^{87}Sr/^{86}Sr)_i$ data of Luenha picrites is extended from chondritic to highly radiogenic ratios maintaining nearly chondritic $(\varepsilon_{Nd})_i$ values (Turunen 2015). The North Karoo and South Karoo data is from GEOROC (last visited 24.4.2018).

The topmost lava flows (AL-T026B, AL-T026C and A-T026D) have relatively high MgO content (7.2–10.5wt.%, Table 1), low TiO_2 content (0.5–0.6wt.%, Table 1) and REE-patterns that conform to E-MORB (Turunen 2015). The whole-rock $(^{87}Sr/^{86}Sr)_i$ ratios measured for T026B, T026C and T026D are 0.71019, 0.70682 and 0.70847, respectively (Turunen 2015) (Table 1). The flow AL-T026E has relatively high MgO content (9.2wt.%, Table 1) and slightly elevated TiO_2 content (0.9wt.%, Table 1) relative to other samples of the sequence (Turunen 2015). The REE pattern of the flow AL-T026E resemble EMORB and whole-rock $(^{87}Sr/^{86}Sr)_i$ ratio is 0.70690 (Turunen 2015). The most magnesian samples are the olivine cumulates AL-T026G and AL-T042 with MgO content of 25.0wt.% and 26.8wt.%, respectively; TiO_2, however, remains low in both (0.3 and 0.4wt.%, respectively) (Turunen 2015). The REE pattern of T026G is equivalent with EMORB, but AL-T042 is more comparable to depleted-MORB like source; isotopically AL-T042 is the most chondritic, with $(^{87}Sr/^{86}Sr)_i$ ratio of 0.70410 whereas AL-T026G is relatively radiogenic $(^{87}Sr/^{86}Sr)_i$ of 0.70746 (Turunen 2015).

Table 1. General features of the studied samples from Luenha exposure presented in stratigraphic order. TiO_2, MgO, Sr and whole-rock data of $^{87}Sr/^{86}Sr$ is provided by Turunen (2015).

Sample	Rock-type*	Texture	Plagioclase phenocryst vol-%	TiO_2 wt.%	MgO wt.%	Sr ppm	$(^{87}Sr/^{86}Sr)_i$
AL-T026C	Basalt	Subophitic	5	0.50	10.50	107.49	0.70682
AL-T026B	Basalt	Subophitic	5	0.50	8.94	256.90	0.71019
AL-T026D	Basalt	Subophitic	5	0.57	7.22	132.12	0.70847
AL-T026E	Basalt	Nesophitic	5	0.94	9.18	126.15	0.70690
AL-T026G	Komatiite	Ophitic		0.29	25.00	72.96	0.70746
AL-T042	Komatiite	Ophitic		0.38	26.83	32.79	0.70410

* according to classification of Le Bas (2000) IUGS

The geochemistry of the Luenha picrites (very low TiO_2, very positive ΔNb, low La/Sm and Zr/Y) indicate that the parental magma of the Luenha picrites was generated by high-degree of melting in the spinel stability field and they segregated from the mantle source at less than 55 km depth (Turunen 2015). Based on the AFC modelling of Turunen (2015), the compositional variability at the Luenha picrites results from crustal contamination of a parental magma similar to the most primitive sample AL-T042. Because of miscellaneous compositional features e.g. MORB-like REE pattern, OIB-like positive Nb, and Nb-enrichment typical to SCLM, several source possibilities for Luenha picrites

have been proposed (Fig. 7), from a convective mantle (MORB or OIB-like plume source) to a heterogenic lithospheric mantle (SCLM) (Turunen 2015). Given that the Luenha picrites may be genetically related to the vast North Karoo sub-province (Fig. 6) the identity of the mantle source presents an outstanding key question.

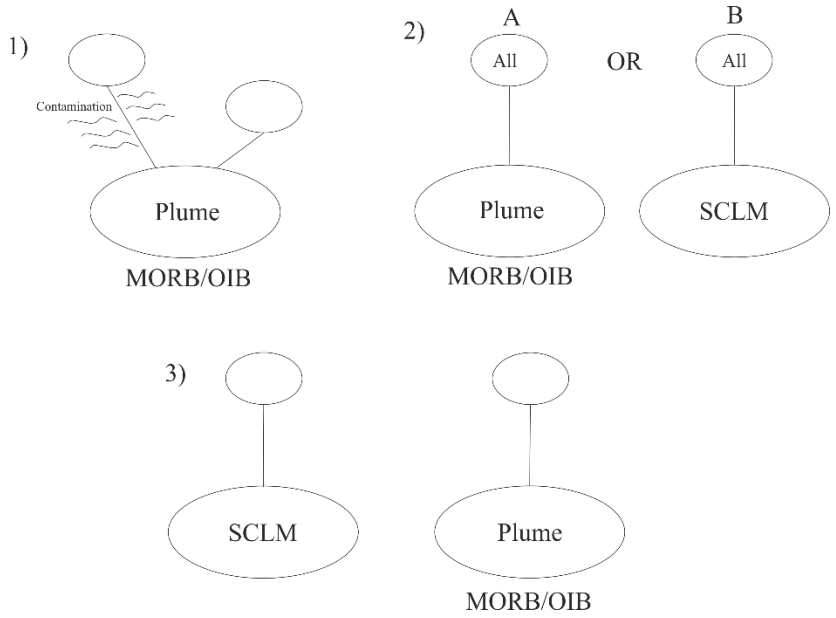

Figure 7. Possible mantle source scenarios for generating the geochemistry in Luenha picrites. **1.** One source from convective mantle introduced with magma plumbing and crustal contamination. **2.** MORB/OIB-like source or SCLM source generating the Luenha picrites. **3**. Heterogenic mantle with two distinct sources. After Turunen (2015).

3. SAMPLES

Samples selected for this study are plagioclase bearing picrites (n = 5), and one plagioclase phenocryst-free olivine cumulate. Picrite samples (AL-T026C, AL-T026B, AL-T026D, AL-T026E, AL-T026G and AL-T042) of six lava flows along the Luenha River were collected by Doctors Arto Luttinen and Jussi Heinonen in 2012. Current study is based on 332 chemical and 31 Sr isotope analyses of five polished thin sections (≥30μm) (AL-T026C, AL-T026B, AL-T026D, AL-T026E and AL-T042) and four thick sections (~300μm) of the same samples (AL-T026B, AL-T026D, AL-T026E, AL-T026G). Hereafter the samples will be referred to as abbreviated (e.g. AL-T026C as T026C). The petrographic and geochemical features of the studied samples described here

are based on studies of Turunen (2015). A summary of the main features is presented in Table 1.

Olivine basalts from top of the sequence (T026B, T026C and T026D) are all similar. Euhedral plagioclase and olivine phenocrysts are in subophitic groundmass with interstitial devitrified glass and opaque minerals. Plagioclase phenocrysts (0.5–3.0 mm) are commonly sieved and oscillating and olivine phenocrysts (0.2–3.0 mm) are completely altered into serpentine. Groundmass is pilotaxitic.

Sample T026E from the quenched layer at the bottom of the unit has euhedral plagioclase (0.5– 3.0 mm) and olivine phenocrysts (0.5–3.0 mm) in a microcrystalline nesophitic slightly trachytic groundmass with some amygdules. Olivine phenocrysts are fresh and some of the plagioclase phenocrysts show sieve texture.

The olivine cumulates T026G and T042 have fresh olivine phenocrysts in a pilotaxitic ophitic groundmass. Sample T026G from the bottom of the lowest unit and sample T042 has abundant coarse-grained fresh seriate olivine phenocrysts (5.0–7.0 mm, up to 10 mm), plagioclase phenocryst being absent. Olivine phenocrysts in the T042 have corroded grain boundaries.

4. METHODS

4.1. Cold-cathode cathodoluminescence microscopy (CL)

To reveal the chemical zoning patterns within plagioclase phenocrysts, both thin and thick sections were examined and imaged using the cold-cathode cathodoluminescence microscope at the University of Helsinki. The CL8200 Mk5-2 optical cathodoluminescence apparatus generates cathodoluminescence by electron gun equipped with vacuum chamber, which is coupled to a Leica optical microscope. The Leica optical microscope is equipped with camera for imaging. The acceleration voltage for electron beam was 7.5 kV with a vacuum from 0.07 to 0.04 mBar. The intensity of colors of cathodolumenescence images were adjusted to different shutter times, from ~ 6s. for thin sections up to 253s. (~4 min.) for thick sections.

4.2. Electron probe micro-analysis (EPMA)

The major element chemical composition of plagioclase was examined using a JEOL JXA-8600 Superprobe equipped with energy dispersive spectrometer (EDS) and four wavelength-dispersive spectrometers (WDS) at the Department of Geosciences and Geography, University of Helsinki. EDS was used for qualitative mineral phase recognition and WDS for quantitative chemical analysis for all plagioclase measurements. Acceleration voltage of 15 kV and beam current of 15 nA, with focused beam was used for all analyses. PAP (Pouchou and Pichoir 1984) correction for matrix was executed with the XMAs software, and stoichiometric calculations were conducted using the Formula Software. The standards used for plagioclase consisted of synthetic and natural silicates and oxides: Albite for Si and Na, Rutile for Ti, Plagioclase An_{65} for Al and Ca, Hematite for Fe, Periclase for Mg, Celestine for Sr, Barite for Ba, and Sanidine for K.

The analysed plagioclase phenocrysts (n = 66) were selected according to zonation observed with CL images, including all types of observed texture types. Analysis points were taken from different zones from phenocryst crystal cores to rims. Groundmass plagioclase grains (n = 22) were analysed as well. The analyses were performed on polished thin and thick sections, coated with carbon to stabilize the beam and cleaned with alcohol just prior to setting them to a sample holder.

4.3. Laser ablation multi-collector inductively coupled plasma mass spectrometry (LA-MC-ICP-MS)

Representative plagioclase phenocrysts were selected from carbon coated thick sections based on the CL images and EPMA results from the samples T026B, T026D, T026E and T026G.

In situ $^{87}Sr/^{86}Sr$ microanalyses of plagioclase phenocrysts (n = 11), the surrounding groundmass (n = 10) and one individual groundmass plagioclase grain were performed utilizing a Nu Plasma LA-MC-ICP-MS with high-resolution collectors (with nine Faraday detectors and amplifiers with 1011 Ω resistors) attached to a Photon Machine Analyte G2

laser microprobe at the Finnish Isotope Geological Laboratory in Espoo. All sections were ablated in a He gas filled HelEx ablation cell (Müller et al., 2009) (gas flows = 0.4 and 0.1 l/min). Pulse frequency of 10 Hz, and beam energy density of 3.5 J/cm^2 were used for every ablation. The data were collected in static mode using five collectors for ^{84}Sr-Kr, ^{85}Rb, ^{86}Sr-Kr, ^{87}Rb-Sr, and ^{88}Sr.

To obtain the quality of Sr isotope data, the following corrections were made to diminish influences of other factors. The exponential law and ^{86}Sr/^{88}Sr value of 0.1194 corrected the effect of instrumental mass fractionation (on measured Sr isotope ratios). After Jochum et al. (2009), the most interfering elements for LA-ICP-MS are Rb and Kr, and the overlap of ^{87}Rb on ^{87}Sr (isobaric interference) was eliminated by monitoring the ^{85}Rb ion signal on every ablation, and utilizing a ^{87}Rb/^{85}Rb value of 0.38571 in order to subtract the ^{87}Rb intensity from ^{87}Sr. ^{86}Kr, formed from He and Ar, has isobaric interference on ^{86}Sr, and therefore 30s-background measurement was performed prior to every ablation.

To obtain the internal precision (of $\leq \pm$ 0.00008 (2σ)), each ablations were scanned for 120s. Two standards were used to ensure the accuracy for laser ablation protocol by repeated scans. For plagioclase phenocrysts, an in-house standard Mir a (Rankenburg et al. 2004) obtained an average value for ^{87}Sr/^{86}Sr ratio of 0.703104 ± 0.000036 (2σ) (n = 5), and the average ratio for ^{84}Sr/^{86}Sr during the measurement day was 0.05638 ± 0.00022. The second standard BHVO-2G gave ^{87}Sr/^{86}Sr ratio of 0.703450 ± 0.000023 (1σ) (n = 3) setting within the certified value preferred by GEOREM database (0.703476 ± 0.000007). For bulk groundmass analyses, the in-house standard Mir a gave an average ^{87}Sr/^{86}Sr ratio of 0.702997 ± 0.000006 (1σ), and an average ^{84}Sr/^{86}Sr 0.056083 ± 0.000006 (1σ) (n = 5). The second standard BHVO-2G had an average ^{87}Sr/^{86}Sr ratio of 0.703612 ± 0.000020 (1σ), and an average ^{84}Sr/^{86}Sr 0.051853 ± 0.000050 (1σ) (n = 5). For both sessions, the measured Mir a values are comparable to the TIMS value of 0.703096 ± 0.000007 (2s) (Rankenburg et al. 2004), and ^{84}Sr/^{86}Sr ratios were similar with the approved values of Thirlwall (1991) (ca. 0.056 ± 0.0001). BHVO-2G ratios are within the certified value preferred by GEOREM database (0.703476 ± 0.000007). The standards and measured samples had similar laser ablation parameters.

The previously introduced isotope methodology (CIS) was followed. Yet, most of the individual composition zones in plagioclase were too narrow to be analysed with required precision, and thus their isotopic signatures are mixed with the signature of other, possibly isotopically different, zones. This may cause average ratios and loss of some spatial information for reconstructing the differentiation history in more detailed level. The Sr content (ppm) (Table 1) of these depleted samples is not high enough for smaller sampling size to gain enough Sr signal. To achieve the best Sr isotope results for plagioclase, a laser diameter of 220 µm is recommendable with the used apparatus (personal communication with Yann Lahaye, 2017) and under the conditions of this study, laser beam of ∅ 160 µm was chosen for phenocryst analyses to still have proper results, but maintaining the possibility to take more than one ablation pit from one phenocryst.

Analyses comprise two to three ablations from one plagioclase phenocryst and bulk groundmass ablations. Round laser spot of ∅ 220 µm was used for all but three bulk groundmass measurements, of which two were fulfilled with a spot of 160 µm. One individual groundmass plagioclase grain from T026D was analysed with spot of 110 µm.

5. RESULTS

5.1. Plagioclase petrography

Plagioclase is present both as phenocrysts and as groundmass in samples from T026C to T026G, and only as groundmass in T042.

5.1.1. Plagioclase phenocrysts

A total of 149 plagioclase phenocrysts were examined during this study, of which most show internal zoning observed in CL in addition to typical polysynthetic albite twinning and Carlsbad twinning. Euhedral crystal habits are the most common although, in many cases the crystal boundaries are irregular, commonly in consequence of overgrow. The grain size of plagioclase phenocrysts in the samples T026B, T026C and T026D is 0.5–4.5 mm. In the sample T026E phenocrysts are seriate at the overall 0.5– 4.0 mm range.

Secondary alteration products of plagioclase, most commonly sericite and saussurite, were observed in minor amounts within the phenocrysts, commonly along cracks. Bright-colored unrecognized minerals as seen in CL image in Figure 8-D, are probable secondary products and, when present, appear in or near inclusions. The secondary products are so diminutive that all plagioclase phenocrysts can be described unaltered and fresh.

Compositional zoning patterns in plagioclase phenocrysts observed with CL microscope show nearly always two concentric zones up to four individual zones (the outermost surface in contact with groundmass is not considered). Zoning is commonly systematic with regular zone boundaries, or zone boundaries are dissolved to irregular shape (usually the innermost). The thickness of an individual zone is typically thinner around crystal rims and thickest at crystal cores, with some exceptions. Fractures across phenocrysts have altered the composition making some zones look patchy-like.

Textural appearances of plagioclase phenocrysts are mostly controlled by the extent of sieve texture. Thin, (tens of microns) sieve-textured resorption zones with micron-scale melt inclusions are in some cases surrounding clear crystal cores (Fig. 8-B), or core zones are dissolved and sieved (Fig. 8-C). Sieve texture can also be extended throughout the grain (Fig. 8-D) in contrast to internally homogeneous grains. Resorption features as sieve texture and dissolution surfaces are commonly met, but in some samples more than in others. For example, sieve texture is pronounced in sample T026B, where strongly sieved cores are the most abundant and it has the smallest fraction of inclusions-free grains (6 out of 47 are inclusion-free). In contrary, sample T026D has the highest quantity of unresorpted crystals, and the crystals with resorption features, are sieved in cores. The sieve texture is not specifically correlated with grain size, with exception that the most coarse grained crystals (n = 7, $\varnothing$ <3 mm) have melt inclusions.

Detailed examination of the relation between inclusions and polysynthetic twin planes unveiled, that in multiple crystals with twin planes visible, the inclusions are parallel to the twinning and not cross-cutting. Cross-cutting resorption surfaces were not observed.

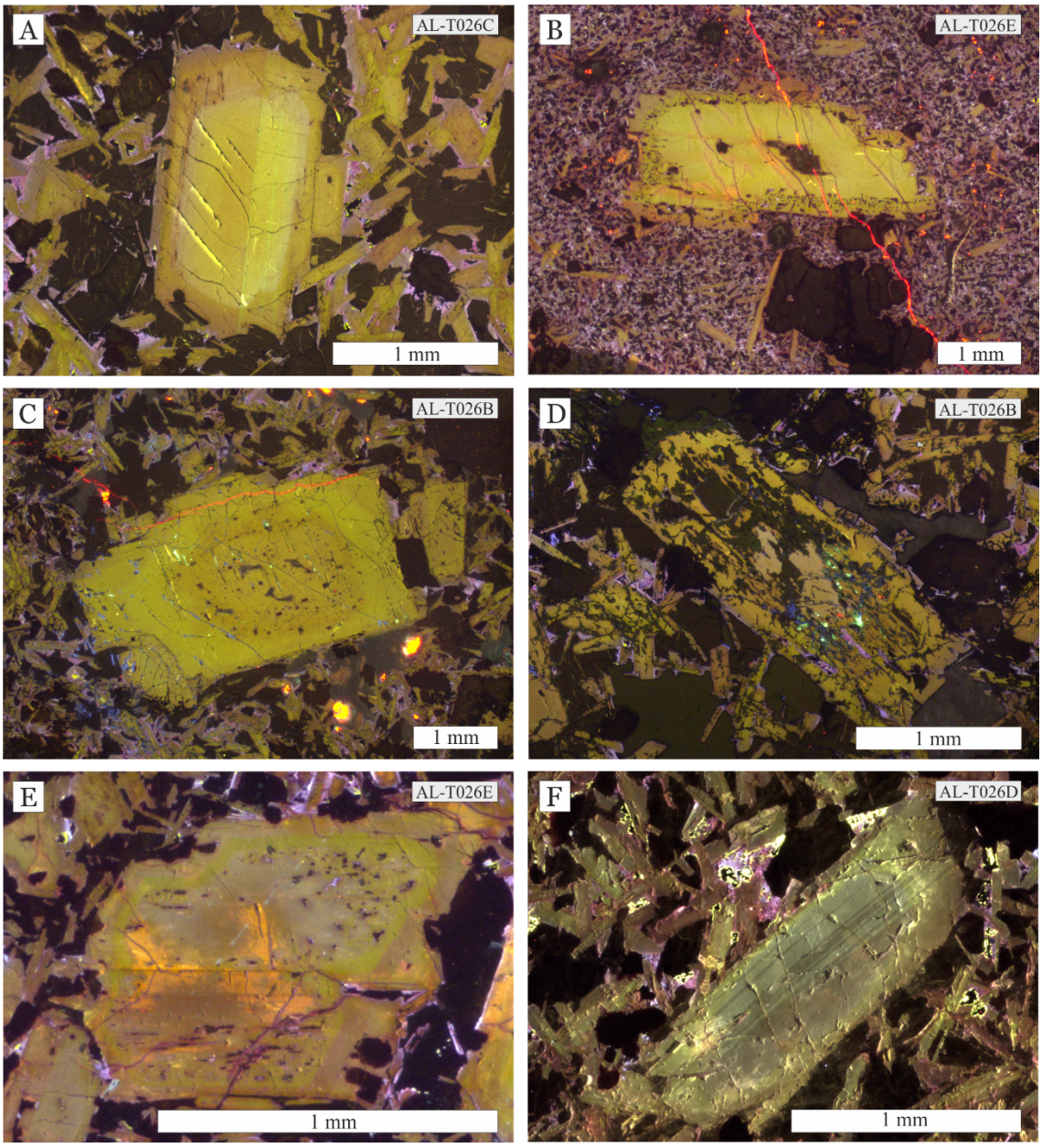

Figure 8. CL images of differentiation levels and habits in the plagioclase phenocrysts of the Luenha river lavas. A-D are thin section images and E-F are thick section images. Bright red grains in the groundmass are apatite and red veins are fractures through section. **A.** An unaltered phenocryst with clear chemical zoning and inclusion free core. Few small inclusions are restricted at the medial zone. Groundmass plagioclase is fresh. **B.** An unaltered, compositionally homogeneous phenocryst with a large inclusion at core. Thin, sieved rim consists of multiple micron-scale inclusions. **C.** Nearly nonexistent alteration (bright spots) in phenocryst with clear chemical zoning. The round inner zone is resorpted and accompanied with sieve texture. Inclusions are round and ameba-like **D.** Minor alteration (bright spots) and weak zoning in coarsely sieved phenocryst. Sieve texture extends throughout the phenocryst and inclusions are large (e.g. glass). Groundmass plagioclase is sieved as well. **E.** Relatively homogeneous core is surrounded by lighter zone accompanied with inclusions in differentiated subhedral phenocryst. A thin, very strongly yellow zone is inclusion free. **F.** Unaltered subhedral phenocryst with homogeneous core surrounded by a thin zone.

5.1.2. Groundmass plagioclase

Euhedral to subhedral groundmass plagioclase is mostly unaltered and fresh in all samples, sericite and saussurite were not present. The grain size of the groundmass plagioclase in the samples T026B and T026C is <0.3 mm, 1–0.08 mm in the sample T026D and 0.25–0.12 mm in the sample T026E. In the olivine cumulate samples (T026G and T042) the groundmass plagioclase is 0.2–0.4 mm.

In the sample T026B, the groundmass plagioclase is strongly sieved with melt inclusions accompanied with micro fractures through grains (Fig. 8-D). Micro fractures are also abundant in the groundmass plagioclase in the sample T026D in which sieve texture is less pronounced. The most texturally homogeneous groundmass plagioclases are in samples T026C and T026E (Fig. 8-A,E).

5.2. Major element composition of plagioclase

The major element composition was analysed from 66 plagioclase phenocrysts, 22 groundmass plagioclase grains and three plagioclase inclusions in olivine and spinel, resulting 332 spots in total. The microprobe measurement results are available in the Appendices (A-F). The results were screened at 96− 102% to dismiss analyses with marked secondary alteration (Deer et al. 1963: Fe_2O_3 > 1.2wt.%, MgO > 0.8wt.% considered impurities). The SiO_2 content is typically 45−48wt.% among all plagioclase phenocrysts and Al_2O_3 is around 32 to 33wt.%. The composition of plagioclase ranges from labradorite (An = 50 –70 mol.%) to anorthite (An = 90–100 mol.%), the most sodic phenocryst being An_{59} and the most calcic An_{90}. The alkali content (CaO vs. Na_2O) and SiO_2 relation to anorthite content of all phenocrysts and groundmass measurements are mostly consistent, with no marked differences between the stratigraphic units (Fig. 9).

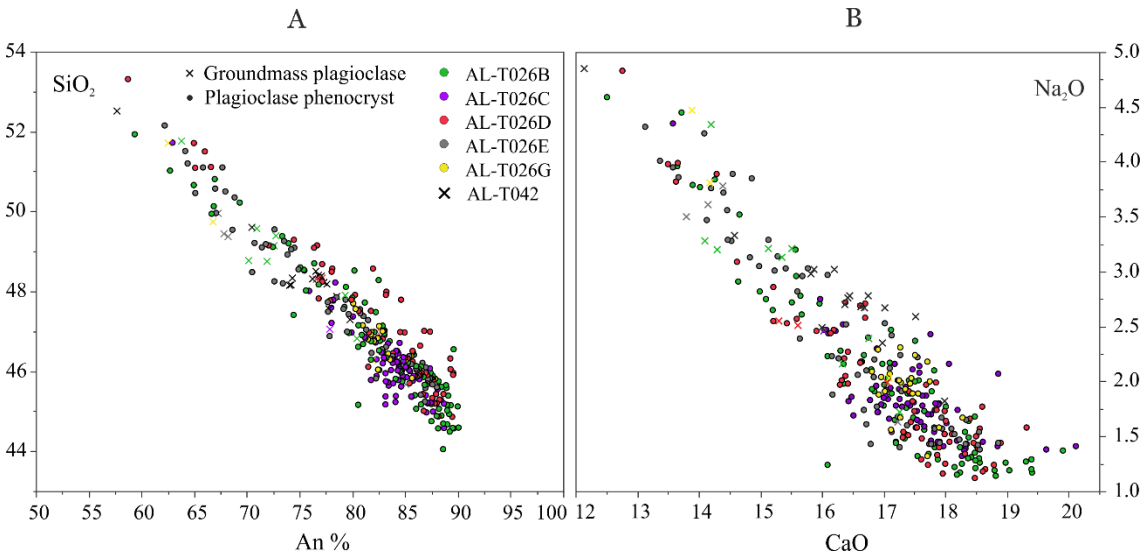

Figure 9. SiO_2 versus An content (**A**) and Na_2O versus CaO (**B**) of the plagioclase phenocrysts and groundmass plagioclase in the Luenha picrites (n = 332). SiO_2, and Na_2O are presented as wt.%. Sample labels in legend are presented in stratigraphic order.

5.2.1. The variation between phenocryst core and rim compositions

Core to rim major element compositions of the plagioclase phenocrysts are mainly systematic and differences are subtle. Generally the crystal rims have higher major element concentrations than crystal cores (Fig. 10). Anorthite variation is present in individual crystals from core to rim, and almost the whole An range can be found in one crystal (~An_{62-88}) (Table 2). In general, the lowest An% is observed in crystal rims in contact with groundmass and the highest in phenocryst cores (Fig. 10).

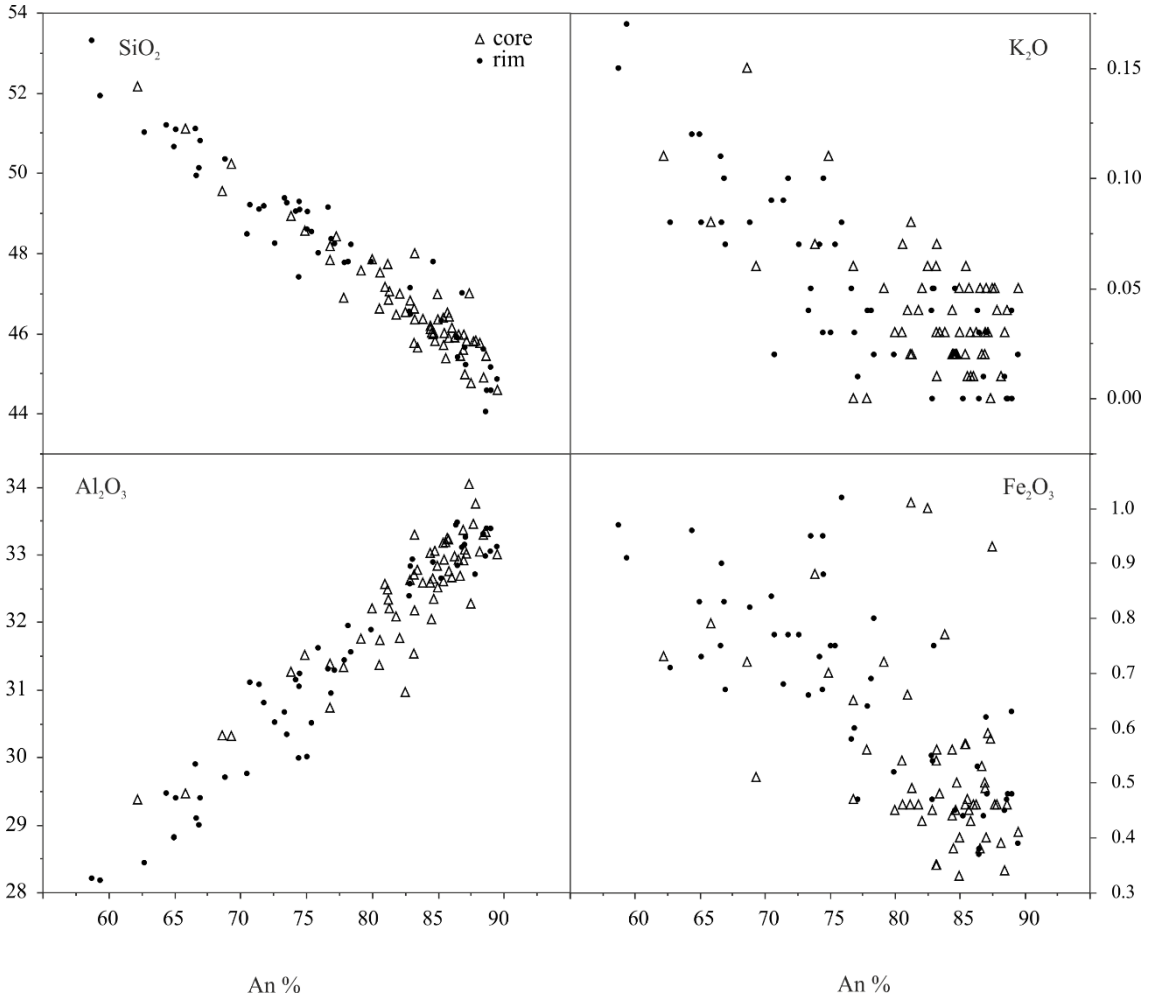

Figure 10. Major element comparisons (SiO_2, Al_2O_3, K_2O and Fe_2O_3) to An content of the plagioclase phenocryst cores (n = 59) and rims (n = 49) in the Luenha picrites. Samples from AL-T026C to AL-T026G. Anorthite is expressed as mol.% and oxides as wt.%.

Similarly, the anorthite content of phenocryst cores (n = 59) range from high An_{90} to low An_{62} (Fig. 11; orthoclase-albite-anorthite ternary diagram), the high An cores being the most abundant and low An cores are the minority; variation between individual lava flows, however exists (Fig. 12). For example, none of the studied phenocrysts from sample T026C have low An cores (all >An_{80}), and they are rare in the samples T026B and T026D as well. On the contrary, almost half of the analysed phenocrysts from sample T026E have low An cores (≤An_{79}). In total, 23 phenocrysts have cores of ≥An_{86} and 11 crystals have cores of ≤An_{79}. All low core crystals are under ∅ = 2.6 mm.

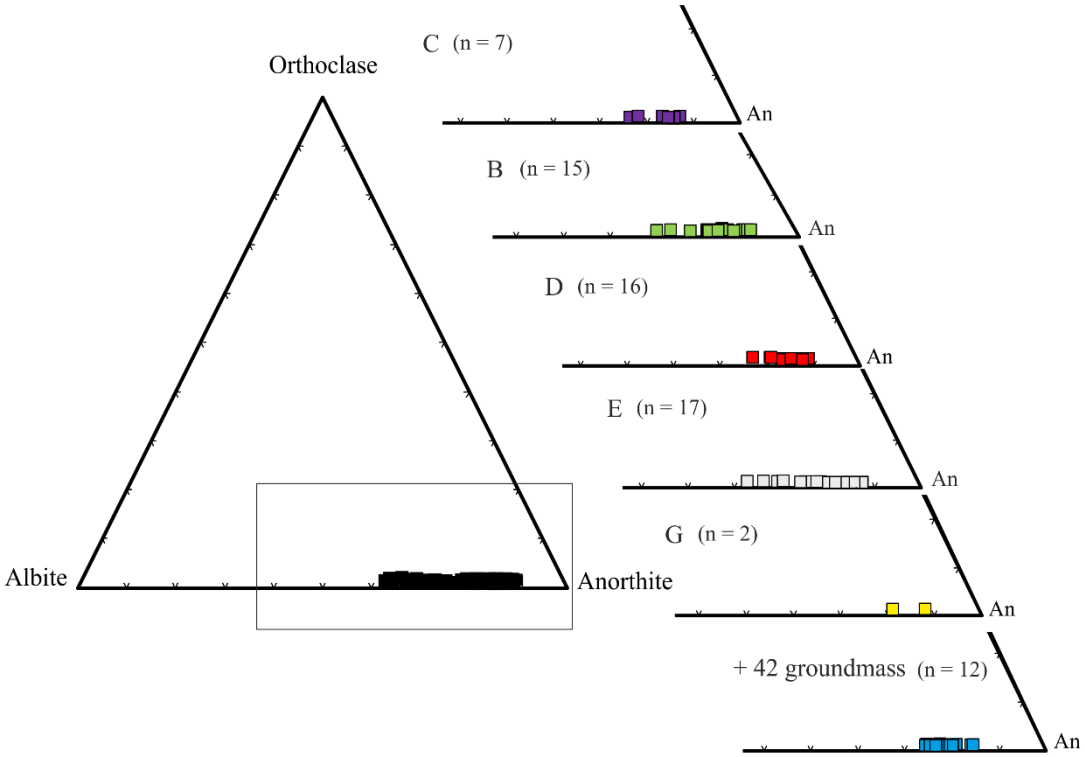

Figure 11. The core compositions of plagioclase phenocrysts (n = 59) plotted in the feldspar ternary diagram. Samples AL-T026C−AL-T026G are presented in stratigraphic order and the groundmass plagioclases of plagioclase phenocryst-free sample AL-T042 are included as well.

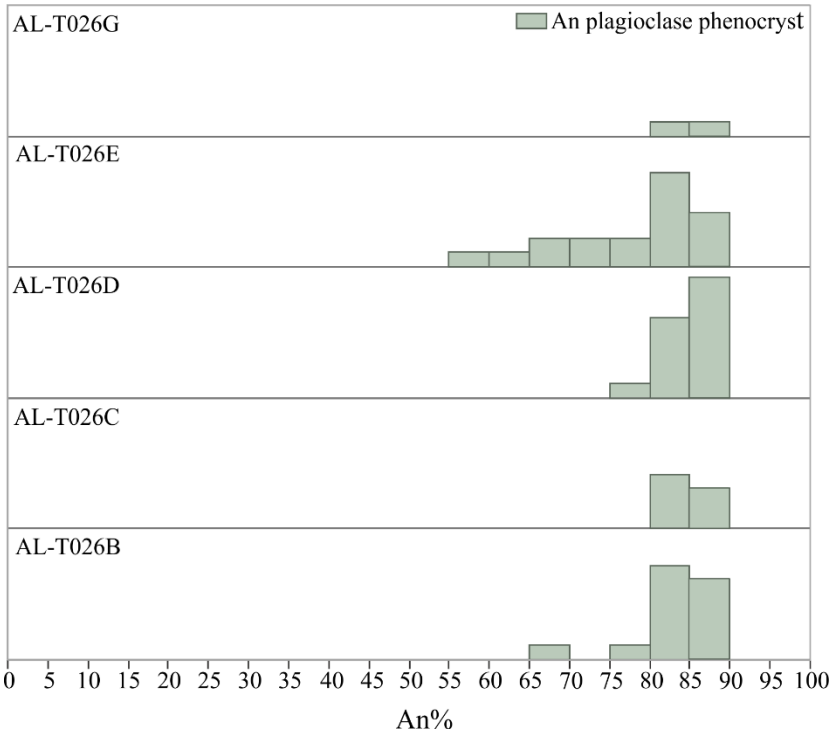

Figure 12. The An contents of plagioclase phenocryst cores (n = 59) in the Luenha picrites. The height of a histogram expresses the quantity of analysed cores.

5.2.2. Compositional zoning of plagioclase – general features

Core to rim analyses revealed three different types of zonation according to An content: normal-, reverse-, and oscillatory zonation. The measured spots that defines the zonings vary from three (from core, middle and rim) to more specific chemical profiles containing up to 40 spots. Such a profile was accomplished manually from subhedral oval shaped (resorpted) grain from T026G consisting of 19 analysis spots, resulting in the range of $An_{80–86}$ (Fig. 13-A) and from the euhedral grain in T026C including 40 spots ranging $An_{78–89}$ (Fig. 13-B).

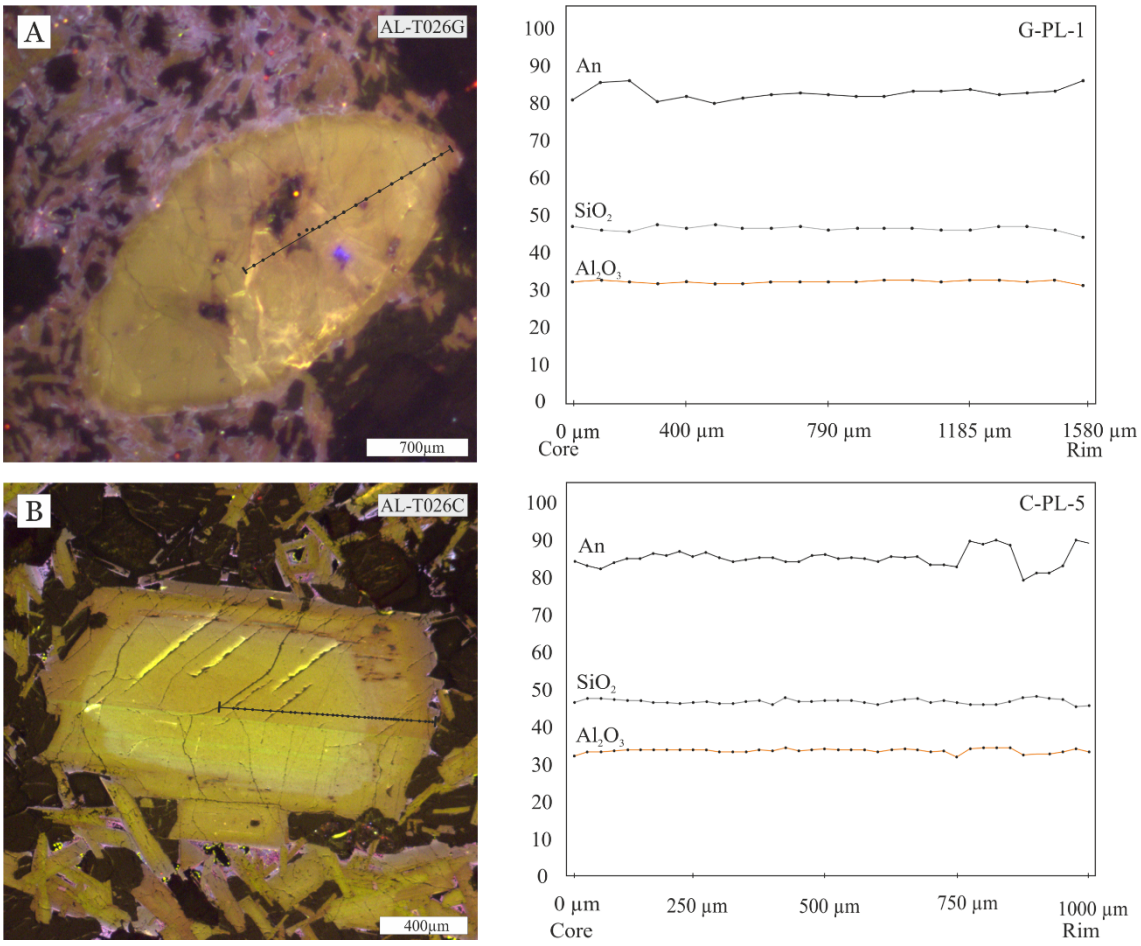

Figure 13. Core-to-rim chemical profiles of An, SiO_2 and Al_2O_3 in the plagioclase phenocrysts in the samples AL-T026G (A) and AL-T026C (B). The black solid line across the phenocrysts indicates the path of analyses and the distance (µm) from core to rim as an approximation. **A.** An oval phenocrysts with resorpted crystal rims. Compositional changes (n = 19) are relatively weak from core to rim, the range in An is from An_{80} to An_{86}. **B.** A euhedral phenocryst with slightly overgrown crystal boundaries. Compositionally heterogeneous core changes to compositionally oscillating zone. The An content is oscillating between An_{78} and An_{89} (n = 40).

The observed An zonings are summarized here, and examples of each type are presented in chapter 5.4.2. In normal zoning the An content decreases (decrease up to 25 An units) from core to rim, always initiating from high-An cores (>An_{81}). Reverse zoning is the opposite, with increasing An content from core to rim, having typically high An core with increase up to 17 An units. If the magnitude of total change in An is less than 10%, the zoning type is considered as normal after Ginibre and Wörner (2007), but in the classification of Pearce and Kolisnik (1990) the An change less than 10% is considered oscillatory. Here, zoning is considered oscillatory if the magnitude in An% variation within crystal is over 7 %. Complexly zoned oscillatory crystals have either high An core (≥An_{80}) or low An core (≤An_{79}); high An cores are the most abundant. Overall, the core-to-rim composition may vary from 1 to > 28 An units over very short distances, and the change in An between contiguous spots can more than 10 mol.%. Normal and oscillatory zonings are the predominant types of compositional variation in all the examined samples. In the following section, sample specific chemical features are presented. An

5.2.3. Plagioclase compositions by flows

In the olivine basalt T026C, 66 major element analyses of plagioclase phenocrysts (n = 11) range from An_{63} to An_{89} with 45–52wt.% of SiO_2 and 29−34wt.% of Al_2O_3 (Fig. 13-B). All the cores (n = 7) are calcic between $An_{83–87}$, rim values (n = 5) are between $An_{76–89}$, and one groundmass grain yielded An_{77} (Table 2). Grains are mostly normally and oscillatory zoned, one reversely zoned grain was also observed.

In the olivine basalt T026B, the compositions of total 87 measurement points from 18 plagioclase phenocrysts range from An_{59} to An_{90} with 44–53wt.% of SiO_2 and 29–34wt.% of Al_2O_3. Crystal cores (n = 15) are An_{69-89}, mostly exceeding An_{80}. Rims (n = 13) vary from $An_{59–67}$ to $An_{73–75}$, up to $An_{86–89}$ similar to the groundmass (n = 9) of $An_{64–84}$ (Table 2). In T026B, oscillatory and reverse zoning are the most abundant with only two crystals observed with normal zoning.

In the sample T026D, the An of plagioclase phenocrysts (n = 19; 63 spots) is $An_{59–90}$ with 45–53wt.% of SiO_2 and 28–34wt.% of Al_2O_3. Of the crystal core measurements (n = 16), the lowest is An_{77} and the most calcic is An_{89}. The rims (n = 14) vary from An_{59} to An_{80}, up to $An_{85–89}$, and groundmass plagioclase (n = 3) has $An_{77–82}$ (Table 2). In T026D, normally zoned crystals are common, and few are oscillatory and reversely zoned.

The plagioclase phenocrysts (n = 21; 64 spots) in the quenching layer T026E have An_{62-88} with 45−51wt.% of SiO_2 and 29–34wt.% of Al_2O_3. The An content of crystals cores (n= 17) is $An_{62–87}$, of which nearly half are less than An_{80}. Crystal rims (n = 10) have $An_{71–75}$ and $An_{83–87}$. Groundmass plagioclase (n = 3) has the An range of $An_{68–85}$ (Table 2). One inclusion measurement in olivine was succeeded (An_{68}). In T026E, oscillatory and normally-zoned crystals are the most numerous and two crystals have reverse zoning.

In olivine cumulate T026G, only two plagioclase phenocrysts were found, with a total of 23 measurements were fulfilled. Composition is consistent with only slight changes; total $An_{80–88}$ with 45–48wt.% of SiO_2 and 31–34wt.% of Al_2O_3. The cores of corresponding phenocrysts are An_{81} and An_{88}, with rims of An_{83} and An_{83}, respectively. Groundmass plagioclase (n = 2) is less calcic with $An_{63–82}$ (Table 2). One plagioclase inclusion yielded $An_{67.}$ The other phenocryst is normally zoned and the other one has low magnitude oscillation with weak compositional changes (Fig. 13-A).

From the olivine cumulate sample T042, 12 analyses were performed on groundmass plagioclase (n = 6), the results display a constant range of 46–49wt.% of SiO_2 and 30–32wt.% of Al_2O_3. The An content extends from An_{74} to An_{84} (Table 2). Iron content is elevated compared to the other samples (0.9–1.18wt.% of Fe_2O_3).

Table 2. Summary of the observed anorthite contents (An) of the plagioclase phenocrysts (core and rim) and groundmass plagioclases. Samples are in stratigraphic order. The number of total spots is the sum of phenocryst and groundmass analysis spots.

Sample	Core mol.% An	Rim mol.% An	Groundmass* mol.% An	Measured phenocrysts	n (total spots)
AL-T026C	83–87 (n = 7)	76–89 (n = 5)	77 (n = 1)	11	67
AL-T026B	69–89 (n = 15)	59–89 (n = 13)	64–84 (n = 9)	18	96
AL-T026D	77–89 (n = 16)	59–89 (n = 14)	77–82 (n = 3)	19	65
AL-T026E	62–87 (n = 17)	71–87 (n = 10)	63–85 (n = 3)	21	68
AL-T026G	85–88 (n = 2)	83–86 (n = 2)	62–82 (n = 2)	2	25
AL-T042			74–84 (n = 12)		12

*Groundmass = groundmass plagioclase

5.3. Sr isotope results of plagioclase

5.3.1. Plagioclase phenocrysts

The most representative plagioclase phenocrysts (n = 11) (Table 3) with different An zonings and variable core An contents were chosen for isotopic microanalysis. The aim of taking measurements from distinct zones was, however, almost never achieved from the rims, since the LA-ICP-MS spot size exceeded the width of a compositional zone. The core zones were large enough for successful measurements. Laser ablation locations can be somewhat distorted even though attention was paid to positioning. Core values were measured from the innermost chemical zone (based on CL images) and the rim values outside the inner zone but ablation pits possibly penetrated beyond the crystal surface. Ablations were visually monitored, and Sr signals > 0.25 V were accepted, and Rb/Sr ratios >0.06 were discarded (all but one has Rb/Sr <0.02), reducing the accepted ablations from 24 to 21.

The phenocryst in situ results are presented in Table 3. All measured $^{87}Sr/^{86}Sr$ ratios are back-calculated to initial ratios at 180 Ma. The similarity of the calculated and age corrected $^{87}Sr/^{86}Sr$ ratios imply that Rb interference is diminutive for the measurements (Munoz et al. 2016).

In situ analyses of plagioclase phenocrysts (n = 3; 4 spots) from the sample T026B yielded measured $^{87}Sr/^{86}Sr$ ratios of 0.70650 to 0.70710 ± 0.00006–5 (1σ) and calculated initial $^{87}Sr/^{86}Sr$ ratios range from 0.70649 to 0.70709 ± 0.00010–12 (2σ). Plagioclases (n = 3; 5 spots) from the sample T026D have measured $^{87}Sr/^{86}Sr$ ratios ranging from 0.70566 to 0.70655 ± 0.00004 –7 (1σ) and initial $^{87}Sr/^{86}Sr$ range from 0.70566 to 0.70654 ± 0.00009–0.00014 (2σ). Phenocrysts (n = 4; 9 spots) from the sample T026E gained measured $^{87}Sr/^{86}Sr$ ratios of 0.70511 to 0.70672 ± 0.00004–0.000007 (1σ) and age corrected $^{87}Sr/^{86}Sr$ ratios range from 0.70511 to 0.70671 ± 0.00009–0.00014 (2σ). Only one plagioclase phenocryst was analysed from the sample T026G (n = 1; 3 spots) with $^{87}Sr/^{86}Sr$ ranges from 0.70545 to 0.70601 ± 0.00006–5 (1σ) and calculated initial $^{87}Sr/^{86}Sr$ ranges from 0.70545 to 0.70600 ± 0.00010–12 (2σ).

The total range of analytical uncertainties (2σ) of the plagioclase phenocryst measurements are between 0.00007–0.00014, which is well within the common analytical

precision of 0.00015 by Allègre (2008) and 0.00005–0.00014 by Borges et al. (2014). If, however, the difference between two ablations (core and rim) are within the internal precision, the ratios of the two were considered equal.

Table 3. In situ LA-MC-ICP-MS $^{87}Sr/^{86}Sr$ determinations (n = 21) of the plagioclase phenocrysts (n = 11). Samples are in stratigraphic order. Used laser spot size is 160 µm for all. Measured $^{87}Sr/^{86}Sr$ ratios are back-calculated to 180 Ma with decay constant of 1.3968×10^{-11} yr^{-1}.

Sample	Phenocryst	Position	$^{87}Rb/^{86}Sr$ meas.	$^{87}Sr/^{86}Sr$ meas.	1σ	$^{87}Sr/^{86}Sr$ initial	2σ
AL-T026B	PL-11	Core	0.0158	0.70668	0.00005	0.70666	0.00010
		Rim	0.0046	0.70652	0.00006	0.70652	0.00012
	PL-6	Core	0.0087	0.70650	0.00006	0.70649	0.00012
	PL-3	Mid	0.0081	0.70710	0.00005	0.70709	0.00010
AL-T026D	PL-1	Rim	0.0013	0.70567	0.00004	0.70567	0.00009
		Core	0.0034	0.70649	0.00005	0.70648	0.00010
	PL-8	Core	0.0037	0.70647	0.00004	0.70646	0.00008
		Rim	0.0048	0.70652	0.00006	0.70651	0.00012
	PL-14	Core	0.0023	0.70566	0.00006	0.70566	0.00011
AL-T026E	PL-5a	Core	0.0012	0.70581	0.00007	0.70581	0.00013
		Rim	0.0520	0.70595	0.00006	0.70586	0.00011
	PL-5b	Core	0.0016	0.70521	0.00005	0.70521	0.00010
		Rim	0.0059	0.70540	0.00005	0.70539	0.00010
	PL-4	Core	0.0028	0.70511	0.00006	0.70511	0.00013
		Rim	0.0038	0.70593	0.00006	0.70592	0.00012
	PL-3	Core	0.0101	0.70672	0.00004	0.70671	0.00007
		Mid	0.0199	0.70628	0.00007	0.70625	0.00014
		Rim	0.0099	0.70593	0.00004	0.70592	0.00009
AL-T026G	PL-1	Core	0.0053	0.70601	0.00006	0.70600	0.00011
		Mid	0.0022	0.70570	0.00005	0.70569	0.00010
		Rim	0.0012	0.70545	0.00006	0.70545	0.00012

The most primitive phenocryst of the Luenha lavas is in the quenched layer of the unit T026E, where small (0.8 mm) inclusion free subhedral phenocryst yielded $(^{87}Sr/^{86}Sr)_i$ ratio of 0.70511. The most radiogenic phenocryst is small euhedral tabular phenocryst (1.1 mm) in the second uppermost unit T026B, with $(^{87}Sr/^{86}Sr)_i$ ratio of 0.70709. The isotopic difference between the most radiogenic and the least-radiogenic plagioclase phenocrysts is quite significant ($^{87}Sr/^{86}Sr$ difference of 0.00198). Although the extremes are from the opposite ends of the stratigraphy, isotope ratios are not coupled with the stratigraphic order or to a single lava flow.

The isotopic variation between phenocryst cores show gradual increase from the least to the most radiogenic compositions, but are not strictly following the stratigraphic order

(Table 4). There are similarities in crystal core ratios between different phenocrysts from different lava flows (Table 4). Plagioclases in samples D-PL-8, D-PL-1 and B-PL-6 have the same $(^{87}Sr/^{86}Sr)_i$ core ratio of ~0.7065. Also, phenocryst B-PL-11 has practically the same core $(^{87}Sr/^{86}Sr)_i$ ratio of ~0.7067 as in the phenocryst PL-3 from the sample T026E, which is from a much earlier magma batch. Further similarities are identified between core-to-rim $^{87}Sr/^{86}Sr$ isotopic evolution where some phenocrysts show increase in the isotope ratios form core to rim (up to 0.00081), some have descending isotope ratios towards rim (up to 0.00081).

Table 4. Core to rim $(^{87}Sr/^{86}Sr)_i$ ratios of the studied plagioclase phenocrysts (n = 11). The analyses are in the order of increasing core $(^{87}Sr/^{86}Sr)_i$ ratio. $^{87}Sr/^{86}Sr$ ratios are age corrected to 180 Ma.

Sample	Phenocryst	Core $(^{87}Sr/^{86}Sr)_i$	Mid $(^{87}Sr/^{86}Sr)_i$	Rim $(^{87}Sr/^{86}Sr)_i$
AL-T026E	PL-4	0.70511		0.70592
AL-T026E	PL-5b	0.70521		0.70539
AL-T026D	PL-14	0.70566		
AL-T026E	PL-5a	0.70581		0.70586
AL-T026G	PL-1	0.70600	0.70569	0.70545
AL-T026D	PL-8	0.70646		0.70651
AL-T026D	PL-1	0.70648		0.70567
AL-T026B	PL-6	0.70649		
AL-T026B	PL-11	0.70666		0.70652
AL-T026E	PL-3	0.70671	0.70592	0.70625
AL-T026B	PL-3		0.70709	

5.3.2. Bulk groundmass

Groundmass isotope analyses (n = 10) were performed on samples T026B, T026D and T026E. The analyses were performed to see how much more radiogenic the groundmass was compared to plagioclase phenocrysts and the whole-rock data. The total Sr content of T042 (33 ppm; Turunen 2015, Table 1) was not high enough for producing detectable signal for analyses (personal communication Yann Lahaye, 2017). Measured $^{87}Sr/^{86}Sr$ ratios are back-calculated to 180 Ma.

All ablations were visually monitored, and those disturbed by excess Rb or other factors (opaque minerals) were excluded, reducing the accepted ablations from 14 to 10. One groundmass plagioclase grain was successfully measured from T026D, but the majority of groundmass plagioclase grains are too small to be analysed individually, and, therefore,

the aim was to gather isotopic data from the bulk composition with varying groundmass mineral assemblies (Table 5). The intention was to ablate regions with secondary alteration minerals, regions with magmatic disequilibrium textures and regions with texturally fresh mineral assemblages (e.g. sieve-free groundmass plagioclase). Unfortunately it was very challenging to find spots with texturally fresh mineral assemblages because sieved plagioclase crystals (magmatic disequilibrium texture) dominate in the groundmass. The fine-grained nesophitic groundmass of T026E offered the most homogeneous choice of all samples.

Bulk groundmass ablations of the sample T026B (n = 3) yielded measured $^{87}Sr/^{86}Sr$ ratios of 0.70895 to 0.71031 ± 0.00002–0.00012 (1σ), and initial $^{87}Sr/^{86}Sr$ of 0.70874 to 0.71019 ± 0.00005–0.00025 (2σ). From the T026D groundmass ablations (n = 4) gave measured $^{87}Sr/^{86}Sr$ ratios between 0.70756 and 0.71073 ± 0.00005–0.00013 (1σ) and initial $^{87}Sr/^{86}Sr$ from 0.70707 to 0.71061 ± 0.00010–0.00025 (2σ). The least radiogenic ratios are gained from the sample T026E, where measured $^{87}Sr/^{86}Sr$ ratios (n = 3) are from 0.70682 to 0.70788 ± 0.00007–00010 (1σ) and $^{87}Sr/^{86}Sr$ initial from 0.70660 to 0.70751 ± 0.00015–0.00020 (2σ).

Table 5. In situ LA-MC-ICP-MS $^{87}Sr/^{86}Sr$ determinations of the bulk groundmass (n = 10) with different alteration levels and mineral assemblages. The samples AL-T026B-AL-T026E are in stratigraphic order. Used laser spot size for most is 220 µm, with few exceptions (with asterisk). Measured $^{87}Sr/^{86}Sr$ ratios are back-calculated to 180 Ma with decay constant of 1.3968×10^{-11} yr^{-1}.

Sample	Alteration	Assemblage	$^{87}Rb/^{86}Sr$ meas.	$^{87}Sr/^{86}Sr$ meas.	1σ	$^{87}Sr/^{86}Sr$ initial	2σ
AL-T026B	A	Pl+Cpx+Cb+Gl	0.0824	0.70895	0.00002	0.70874	0.00005
AL-T026B	A	Pl+Cpx	0.0473	0.71031	0.00003	0.71019	0.00005
AL-T026B	a	Pl+Cpx	0.0458	0.71016	0.00012	0.71004	0.00025
AL-T026D	U	Pl+Cpx	0.1670	0.70805	0.00006	0.70763	0.00011
AL-T026D	A	Pl+Cpx+Spl?*	0.0673	0.70724	0.00005	0.70707	0.00010
AL-T026D	A	Pl+Cpx+Gl*	0.0274	0.70756	0.00006	0.70749	0.00012
AL-T026D	U	Pl+Cpx	0.0474	0.71073	0.00013	0.71061	0.00025
AL-T026D	U	Pl**	0.0102	0.70655	0.00007	0.70654	0.00014
AL-T026E	U	Pl+Cpx+opaq.	0.0531	0.70764	0.00007	0.70751	0.00015
AL-T026E	a	Pl+Cpx+sec.	0.0885	0.70682	0.00009	0.70660	0.00017

*laser beam size 160 µm
**laser beam size 110 µm
Alteration symbols A = altered, a = minor alteration, U = unaltered
Abbreviations: Pl = plagioclase, Ol = olivine, Cpx = clinopyroxene, Spl = spinel, Cb = carbonate, Opaq = opaque mineral, Gl = glass

Rb/Sr ratios in the bulk groundmass samples are relatively high (<0.17) compared to plagioclase phenocrysts (Fig. 14). However, they are not as high as those measured earlier from whole-rock (Turunen 2015).

The results show that the assemblages that include secondary carbonate and glass and less plagioclase yield less radiogenic ratios than spots including plagioclase and clinopyroxene only. Generally, the bulk groundmass is more radiogenic than individual plagioclase phenocrysts.

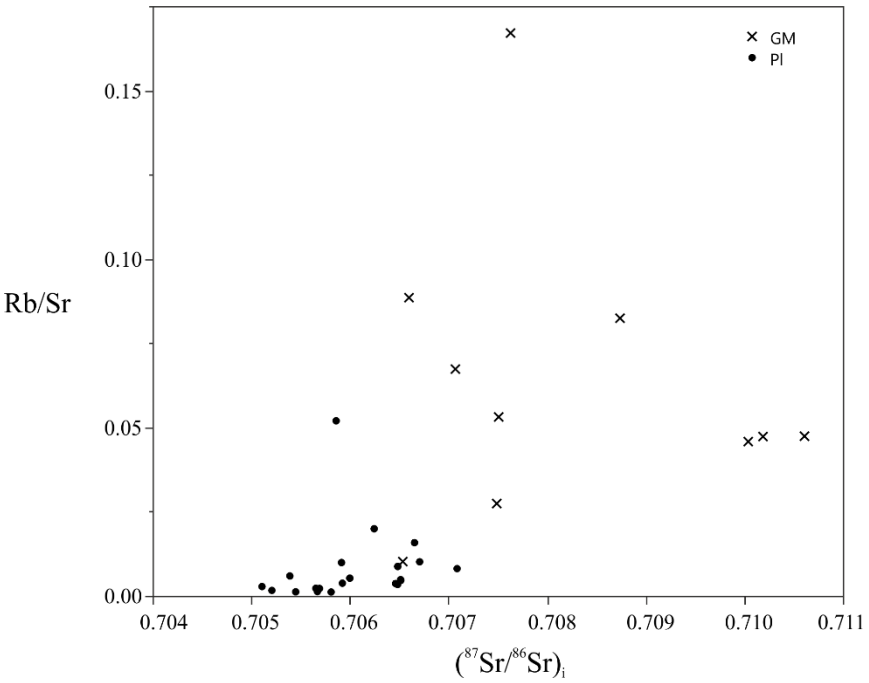

Figure 14. Measured in situ Rb/Sr versus $(^{87}Sr/^{86}Sr)_i$ ratios of the studied plagioclase phenocrysts and bulk groundmass in the samples AL-T026B, AL-T026D, AL-T026E and AL-T026G.

5.4. Compositional classification of plagioclase

5.4.1. Compositional types

Classification of the studied plagioclase phenocryst compositions is based on the relation between anorthite content and the measured $(^{87}Sr/^{86}Sr)_i$ ratio of a single analysis spot. The aim was to recognize An - $^{87}Sr/^{86}Sr$ correlations and the intracrystal combinations (core and rim) of different compositional types (Fig. 15-A). However, defining the An content

for the corresponding laser ablation was problematic as EPMA spot size is notably smaller than LA-ICP-MS pits, making the correlation between $(^{87}Sr/^{86}Sr)_i$ ratios and An contents difficult. For example, LA-ICP-MS analysis spot can include part of zones with An_{66} and An_{82} (Fig. 16-A). Intracrystal changes within a type are faded under a vague type division, as seen from Table 7, where changes from core to rim are presented. Thus, more detailed intracrystal An- $(^{87}Sr/^{86}Sr)_i$ profiles are accomplished for more precise understanding of core to rim changes.

In situ measurements of plagioclase phenocrysts are divided into four compositional types (I-IV) (Fig. 15-A). An content of An_{75} divides the high and low An types, and the division between low and high radiogeneity is set at ~0.70606, where error bars are not overlain. Most of the measurements, which have type I and II compositions, show increasing $(^{87}Sr/^{86}Sr)_i$ with decreasing An content, although some scattering around a common trend line exists ($R^2 = 0.3745$, Fig. 15-A). The most common composition is type I, which is described with high An content and low $(^{87}Sr/^{86}Sr)_i$ ratio. The second abundant is type II compositions which are described with radiogenic $(^{87}Sr/^{86}Sr)_i$ ratio and high An. Type III and IV compositions have been determined by only one measurement in each. The distribution of plagioclase core compositions (types I, II and IV, Fig. 15-A), emphasize a fluctuation in initial crystallization conditions. The distribution of rim compositions (I, II and III, Fig. 15-A) is similar.

The variety of internal textures of crystals are not included to classification because, as Tepley et al. (1999) observed, texture-producing events can be only partially liable for the geochemical changes in plagioclase, thus the main focus is on geochemical data.

5.4.2. Crystallization paths

Examination of the chemical and isotopic data reveals complex intracrystal variations. These can be addressed using the four plagioclase types I-IV (Fig. 15-A), which help to identify four general crystallization paths (A-D) (Fig. 15-B).

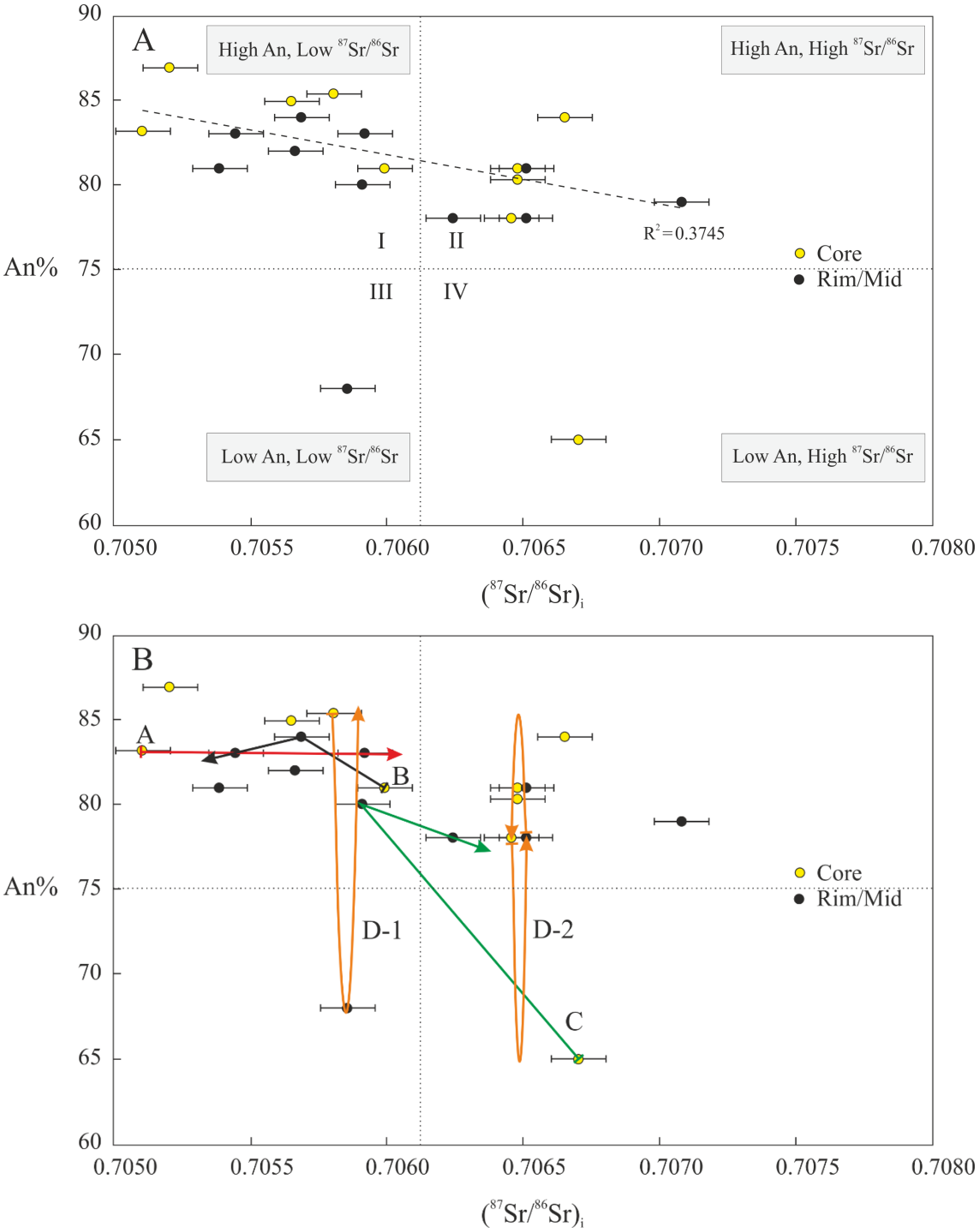

Figure 15. **A.** The An content versus in situ $(^{87}Sr/^{86}Sr)_i$ analyses (n = 21) in the studied plagioclase phenocrysts (n = 11) in the samples AL-T026B, AL-T026D, AL-T026E and AL-T026G. The 2σ error (analytical precision) of measured $(^{87}Sr/^{86}Sr)_i$ ablation is expressed with the width of the black line across the plot. The distribution of core (n = 10), mid (n = 3) and rim (n = 8) ablations are classified into four types (I-IV). Measurements follow a linear regression line (R^2= 0.3745). **B.** Representative plagioclase phenocryst compositional variations from core to rim (A-D) for types I–IV.

Intracrystal changes in $(^{87}Sr/^{86}Sr)_i$ from core to rim showed both isotopically zoned and unzoned plagioclase phenocrysts (Table 7). Zoned plagioclases can be further divided into increasingly, decreasingly and oscillatory phenocrysts. Phenocrysts E-PL-5a, D-PL-8, and B-PL-11 show uniform isotopic composition with variable An contents (Fig. 16). Phenocryst E-PL-5a has type I core and rim, whereas phenocrysts PL-8 and B-11 have type II core and rim. This evolution can be explained with crystallization path D-1 and D-2, respectively (Fig. 15-B). Phenocrysts E-PL-4 and E-PL-5b exhibit normal An zoning and increasing $(^{87}Sr/^{86}Sr)_i$ ratio from core to rim with the corresponding field of type I plagioclase (Fig. 17). This crystallization path is described as path A in Figure 15. Phenocrysts D-PL-1, and G-PL-1 have decreasing $(^{87}Sr/^{86}Sr)_i$ ratio with oscillating An content (Fig. 18). D-PL-1 has type II core and type III rims, whereas G-PL-1 has type I composition thoroughly. These compositional changes can be explained by crystallization path B (Fig. 15-B). E-PL-3 is the only crystal with oscillatory $(^{87}Sr/^{86}Sr)_i$ zoning and oscillatory An zoning (Fig. 19) with composition changing from IV to I to II from core to rim. Crystallization path C describes this complex evolution line (Fig. 15-B). Additionally, three phenocrysts contain only one ablation analysis and are unclassified (B-PL-3, B-PL-6 and D-PL-14, Fig. 20).

Table 7. The plagioclase phenocryst classification after the compositional types in Figure 15-A (I-IV) and the migration paths (A-D) in Figure 15-B. The intracrystal $(^{87}Sr/^{86}Sr)_i$ changes from core to rim are described as increasing, decreasing, oscillatory or are unclassified.

Phenocryst	Variation (core-rim)	Migration path	An zoning	$(^{87}Sr/^{86}Sr)_i$ zoning
E-PL-5a	I → I	D-1	Oscillatory	Unzoned
D-PL-8	II → II	D-2	Oscillatory	Unzoned
B-PL-11	I → II	D-2	Oscillatory	Unzoned
E-PL-4	I → I	A	Normal	Increasing
E-PL-5b	I → I	A	Normal	Increasing
D-PL-1	II → III	B	Oscillatory	Decreasing
G-PL-1	I → I → I	B	Normal	Decreasing
E-PL-3	IV → I → II	C	Oscillatory	Oscillatory
B-PL-6	II	×	Oscillatory	Unclassified
B-PL-3	II	×	Oscillatory	Unclassified
D-PL-14	I	×	Reverse	Unclassified

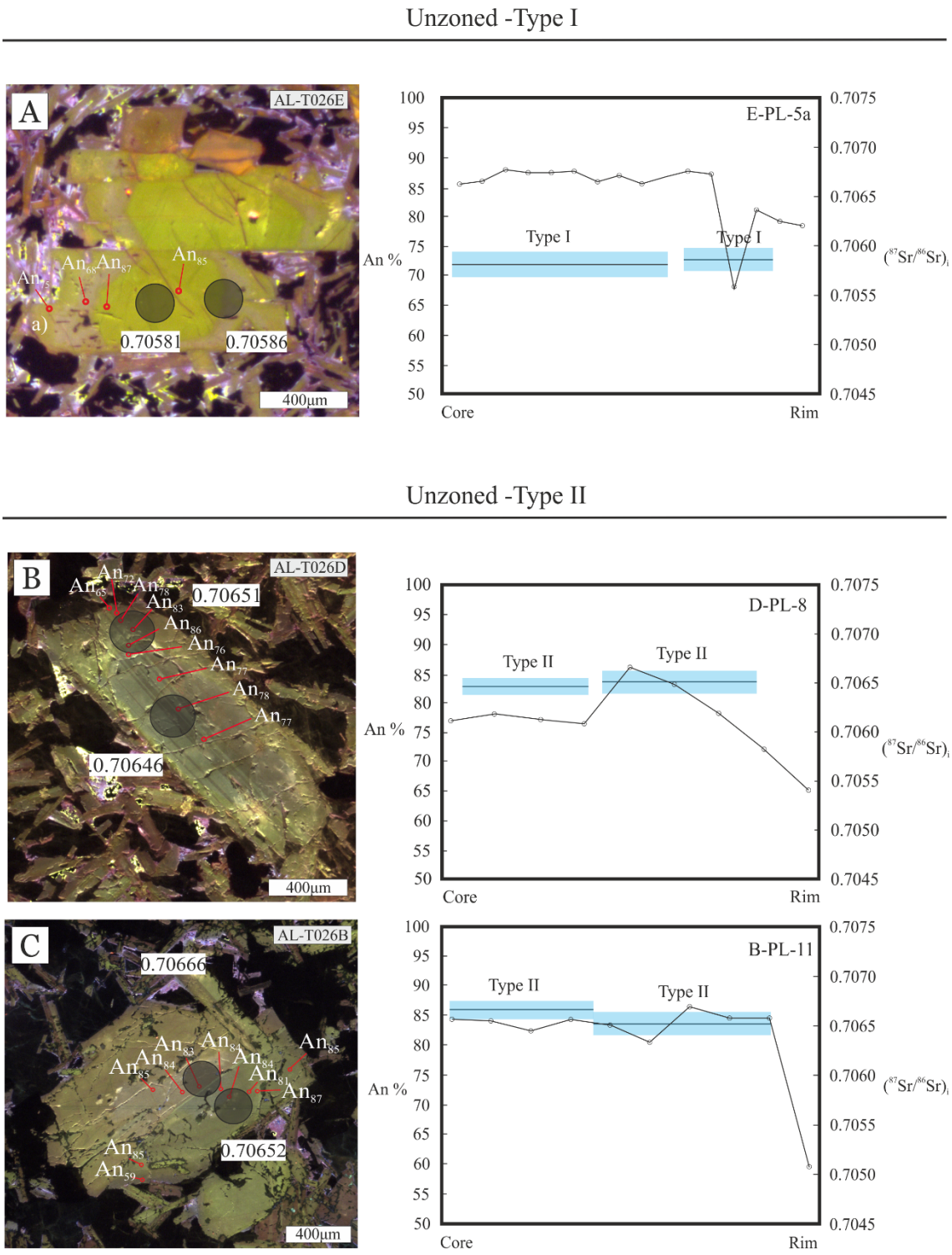

Figure 16. Core to rim An content and $(^{87}Sr/^{86}Sr)_i$ measurements of the isotopically uniform plagioclase phenocrysts. Classified as unzoned-type I and unzoned-type II after compositional variation. Horizontal solid black line is the An content measured from core to rim. The 2σ error (analytical precision) of $(^{87}Sr/^{86}Sr)_i$ ablation in phenocryst is expressed with the thickness of the blue bar, the black line across the bar being the measured initial ratio. **A.** Type I composition throughout the crystal in unzoned-type I crystal. **B.** Type II intracrystal composition with oscillating An content. **C**. Relatively consistent An content (type II).

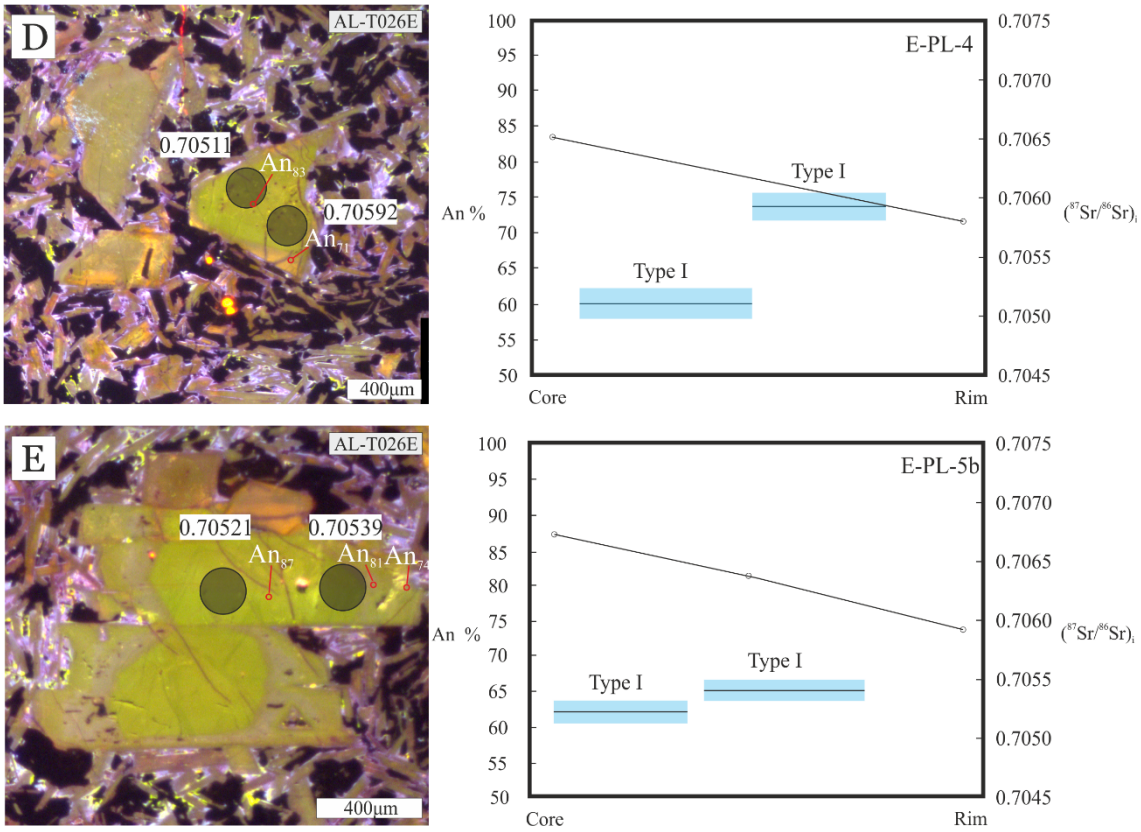

Figure 17. Core to rim An content and $(^{87}Sr/^{86}Sr)_i$ measurements of the isotopically zoned plagioclase phenocrysts with type I composition throughout the crystal. Horizontal solid black line is the An measured from core to rim. The 2σ error (analytical precision) of $(^{87}Sr/^{86}Sr)_i$ ablation in phenocryst is expressed with the thickness of the blue bar, the black line across the bar being the measured initial ratio. **D.** Clear increase in $(^{87}Sr/^{86}Sr)_i$ ratio with normal An zoning. **E.** More subtle change in $(^{87}Sr/^{86}Sr)_i$ ratio and normal An zoning.

Decreasing

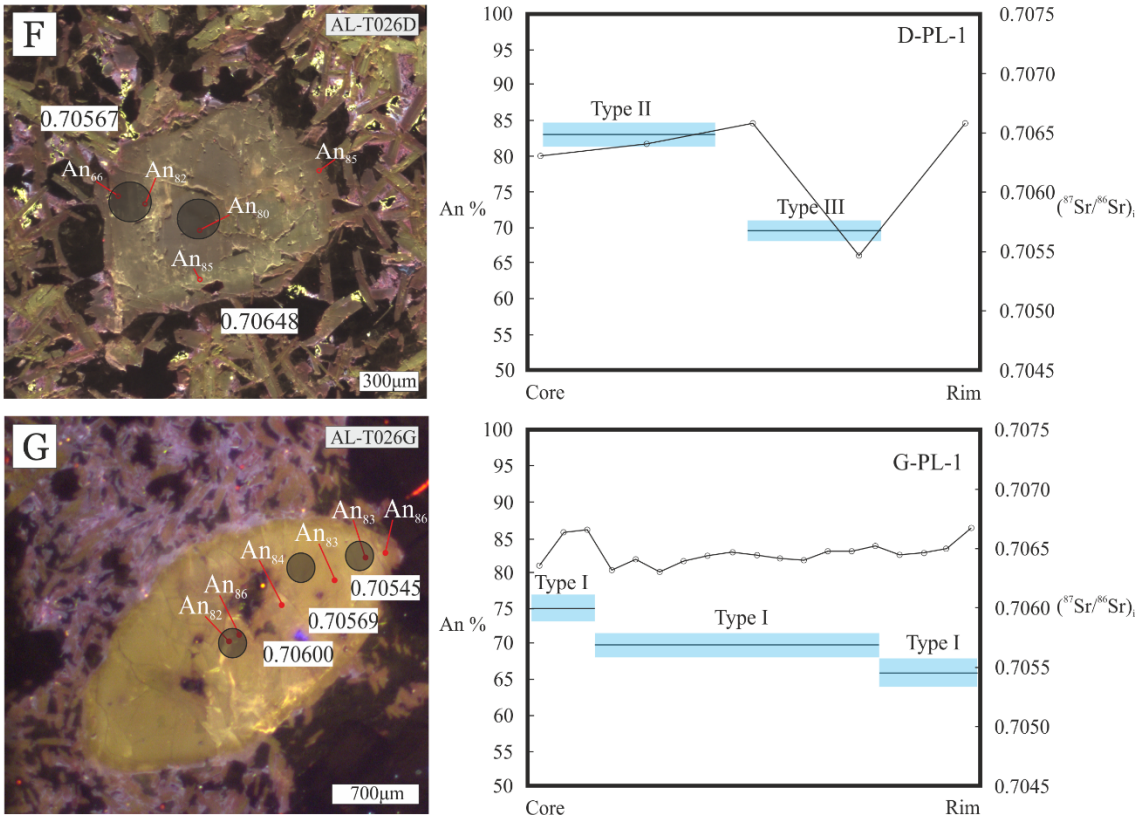

Figure 18. Core to rim An content and $(^{87}Sr/^{86}Sr)_i$ measurements of the plagioclase phenocrysts with decreasing $^{87}Sr/^{86}Sr$. Horizontal solid black line is the An content measured from core to rim. The 2σ error (analytical precision) of $(^{87}Sr/^{86}Sr)_I$ ablation in phenocryst is expressed with the thickness of the blue bar, the black line across the bar being the measured initial ratio. **F.** Strong compositional change from type II to type III with clear decrease in $(^{87}Sr/^{86}Sr)_i$. **G.** Systematically decreasing $(^{87}Sr/^{86}Sr)_i$ from core to rim with slightly oscillating An content (type I).

Oscillatory

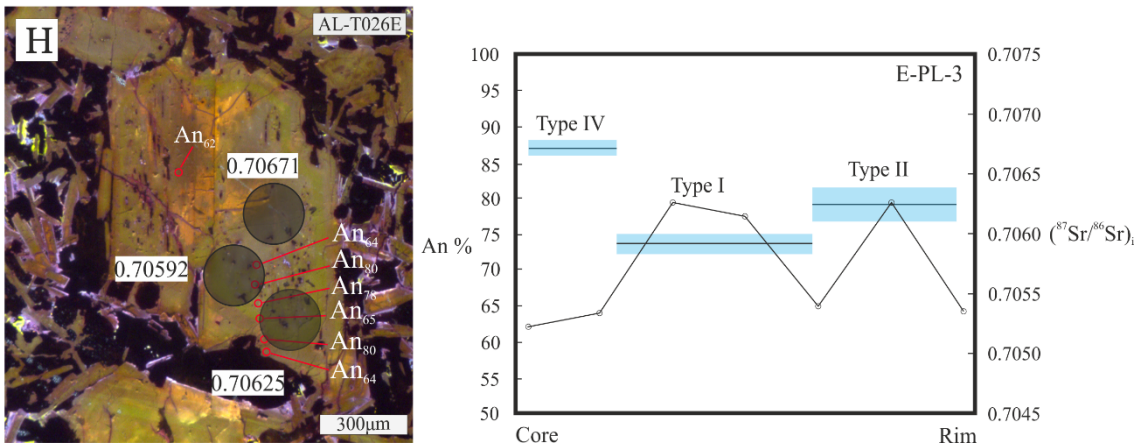

Figure 19. Core to rim An content and $(^{87}Sr/^{86}Sr)_i$ measurements of the plagioclase phenocryst classified as oscillatory. Horizontal solid black line is the An content measured from core to rim. The 2σ error (analytical precision) of $(^{87}Sr/^{86}Sr)_i$ ablation in phenocryst is expressed with the thickness of the blue bar, the black line across the bar being the measured initial ratio. **H.** Compositionally very heterogeneous crystal with oscillatory $(^{87}Sr/^{86}Sr)_i$ ratio from core to rim with oscillating An content.

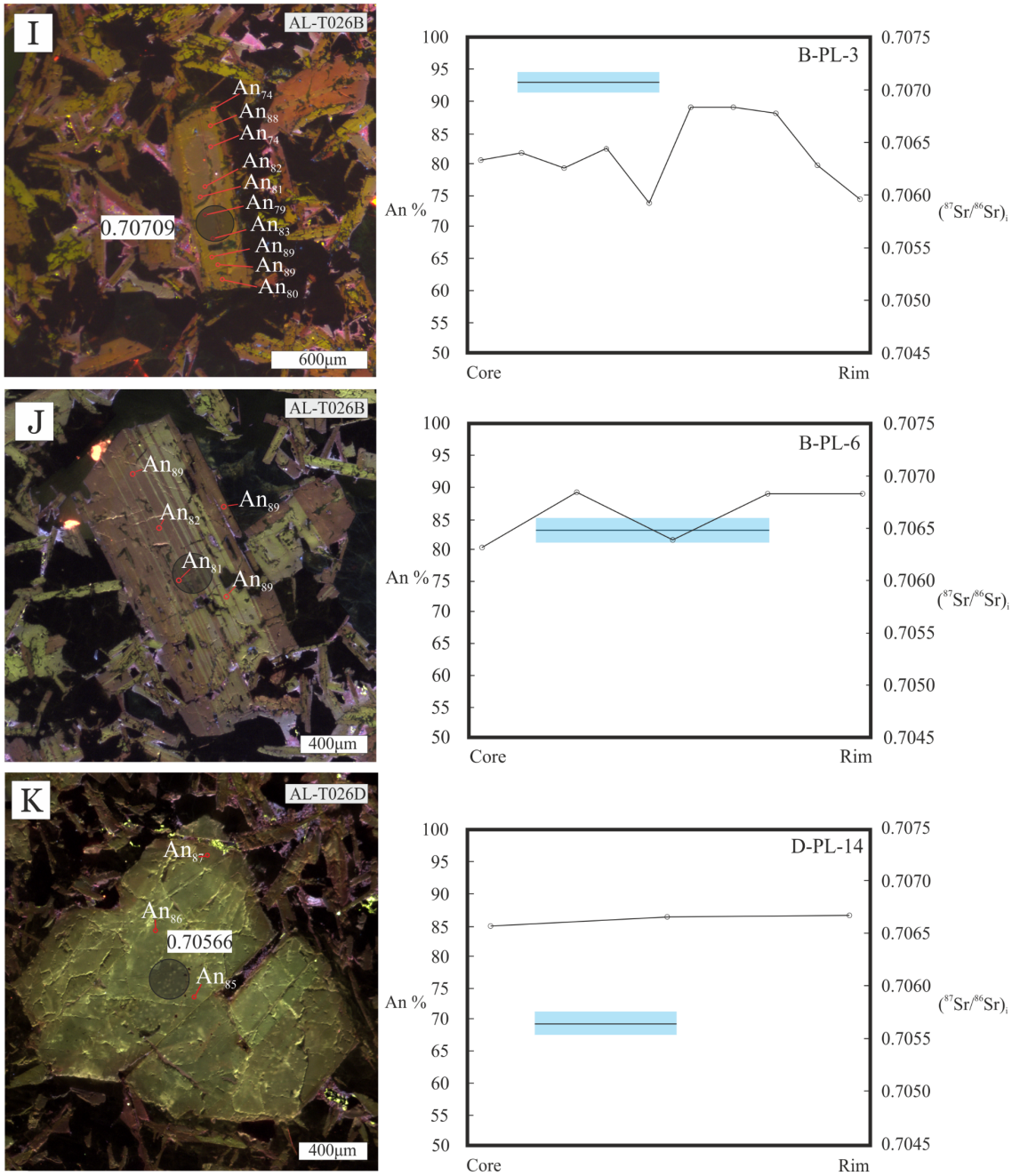

Figure 20. Core to rim An content and core $(^{87}Sr/^{86}Sr)_i$ measurements of the unclassified plagioclase phenocrysts. Horizontal solid black line is the An content measured from core to rim. The 2σ error (analytical precision) of $(^{87}Sr/^{86}Sr)_i$ ablation in phenocryst is expressed with the thickness of the blue bar, the black line across the bar being the measured initial ratio. **I.** The most radiogenic crystal with type II core and clearly oscillating An content. **J.** crystal with radiogenic type II core and oscillating An content. **K.** Moderately radiogenic type I core with stable An content from core to rim.

6. DISCUSSION

6.1. Comparison between in situ and whole-rock data

Compared to the previous whole-rock $(^{87}Sr/^{86}Sr)_i$ measurements (Turunen 2015), the plagioclase phenocrysts of the Luenha picrites are significantly less radiogenic (Table 6, Fig. 21). Generally, the bulk groundmass analyses are more radiogenic than the individual plagioclase phenocrysts and almost as radiogenic as the bulk rock (Turunen 2015) (Table 6). The in situ measurements of the plagioclase phenocrysts in the Luenha lavas are more comparable to the other Karoo lavas (Fig. 21). The plagioclase phenocryst $(^{87}Sr/^{86}Sr)_i$ ratios are more chondritic than the whole-rock measurements of the same samples, but not as chondritic as the least radiogenic Luenha sample T042 and the least radiogenic samples of the North and South Karoo (Fig. 21). Although $(^{87}Sr/^{86}Sr)_i$ variability among the plagioclase phenocrysts in the Luenha lavas still exists, this new in situ data is more coherent and shows that the parental magma of Luenha picrites has been less radiogenic than suggested by the previous whole-rock measurement of Turunen (2015).

Table 6. Summary of all the measured $(^{87}Sr/^{86}Sr)_i$ ratios of the Luenha samples used in this study including previously determined whole-rock data (Turunen 2015). Studied plagioclase phenocrysts are less radiogenic than the whole rock and the bulk groundmass.

Sample	Whole rock $(^{87}Sr/^{86}Sr)_i$	Plagioclase phenocrysts $(^{87}Sr/^{86}Sr)_i$	Bulk groundmass $(^{87}Sr/^{86}Sr)_i$
AL-T026B	0.71019	0.70649–0.70709	0.70874–0.71019
AL-T026D	0.70847	0.70566–0.70659	0.70707–0.70763
AL-T026E	0.70690	0.70511–0.70671	0.70660–0.70751
AL-T026G	0.70747	0.70545–0.70600	x
AL-T042	0.70410	x	x

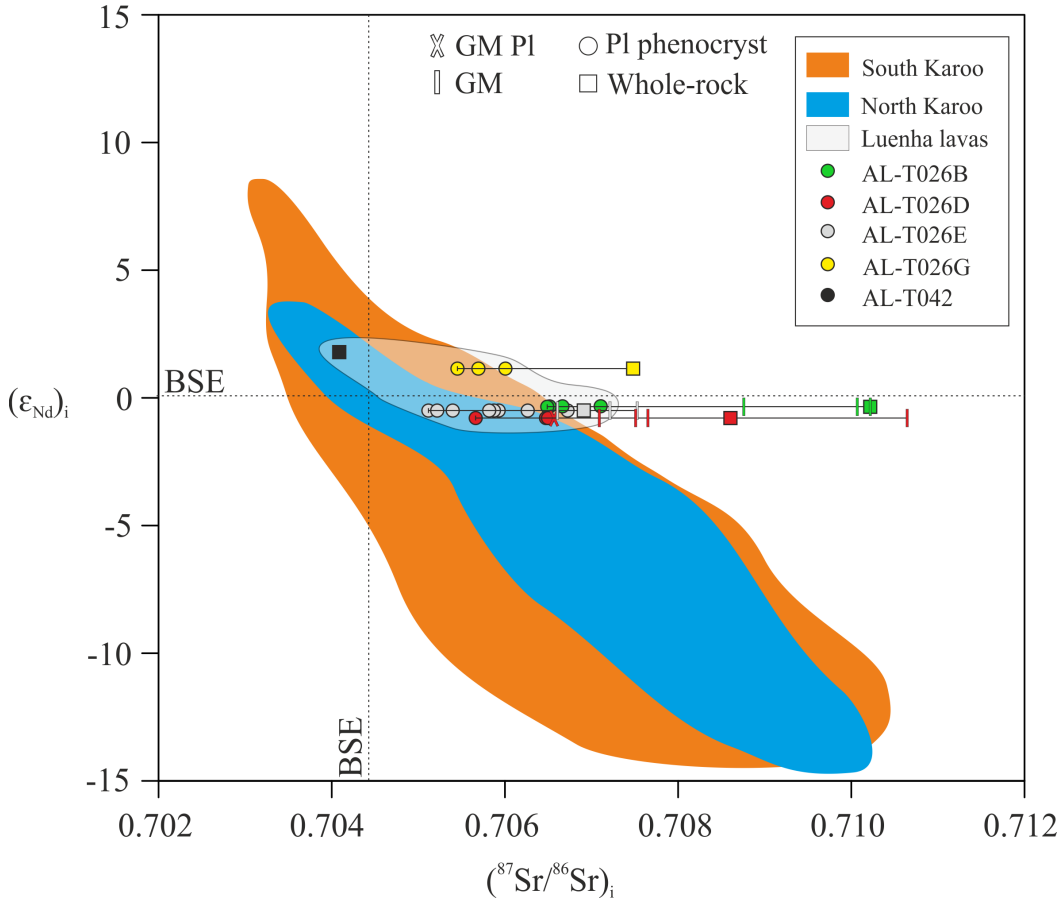

Figure 21. $(^{87}Sr/^{86}Sr)_i$ versus $(\varepsilon_{Nd})_i$ of the plagioclase phenocrysts (in situ, n = 21) and bulk groundmass (in situ, n = 10) compared to the whole-rock data (n = 5; Turunen 2015) in the Luenha picrites. The in situ $(^{87}Sr/^{86}Sr)_i$ measurements of the plagioclase phenocrysts are shifted to more chondritic ratios compared to whole rock ratios. All $(\varepsilon_{Nd})_i$ ratios of the Luenha samples are maintained from the whole-rock data of Turunen (2015). Sample labels in legend are in stratigraphic order. The North and South Karoo data from GEOROC (last visited 24.4.2018).

6.2. An content of plagioclase as tracer of magma chamber conditions

The phenocryst cores are expected to reflect the original anorthite content of the Luenha picrite parental magma at the time when plagioclase stability field was reached and nucleation started. The An content is defined by the temperature-pressure (T-P) conditions, water content (X_{H2O}), and the composition of the melt (X) (e.g. Ginibre et al. 2002, Ginibre and Wörner 2007, Churikova et al. 2013, Utsunisik et al. 2014). Thus, the wide range of the studied plagioclase cores An_{63-90} and diversity in An zoning imply a compositional change of host magma or change in the crystallization conditions. Luenha picrites seem to have been formed in a diverse magma chamber system.

6.2.1. Influence of temperature

As Or component in the measured plagioclase phenocrysts is low (< $Or_{0.99}$; Appendices A-F) the temperature effect on plagioclase composition can be demonstrated with the simplified binary Ab-An system of Bowen (1956). This phase diagram explains how cooling of magma (from 1553 to 1118 C°) leads to progressively more albitic plagioclase compositions by magma fractionation using simple, four-component synthetic material at 1 atm pressure. Normally zoned plagioclases with decreasing An content are formed if crystallization is fractional.

Utsunisik et al. (2014) tested basaltic compositions in MELTS (Ghiorso and Sack 1995) to thermodynamically model how different compositional zoning in plagioclase (with parameters P, T and $X_{H2O,}$ fO_2). The effect of temperature was tested with the magma recharge model, which caused plagioclase to crystallize compositions that are more anorthitic. This model requires that crystals do not dissolve entirely by heat increase.

6.2.2. Influence of pressure

In an anhydrous adiabatic (isothermal) system, pressure decrease shifts plagioclase stability to more anorthitic compositions (e.g. Montana and Nelson 1992, Ginibre and Wörner 2007, Borghini et al. 2010, Churikova et al. 2013, Utsunisik et al. 2014) (Fig. 22-A). Borghini et al. (2010) demonstrated that the An content of plagioclase decreases in with increasing pressure, whereas decreasing pressure of anhydrous magma is causing plagioclase to dissolve (Nelson and Montana 1992). Ginibre and Wörner (2007) propose this to result in more calcic composition. Plagioclase crystallization experiments of Bender et al. (1978) for natural MORB support the pressure dependence, even though the crystallization temperatures for natural samples are lower than those suggested by the synthetic models (e.g. Bowen 1956).

In a dynamic, open-system decompression MELTS-model of Utsunisik et al. (2014), the crystallizing plagioclase compositions are strongly controlled by pressure. Adiabatically rising magma batch resides at continuously shallower levels by steps, and decompression crystallization together with isobaric crystallization produces all normal, reverse, and oscillatory zonings (Fig. 23).

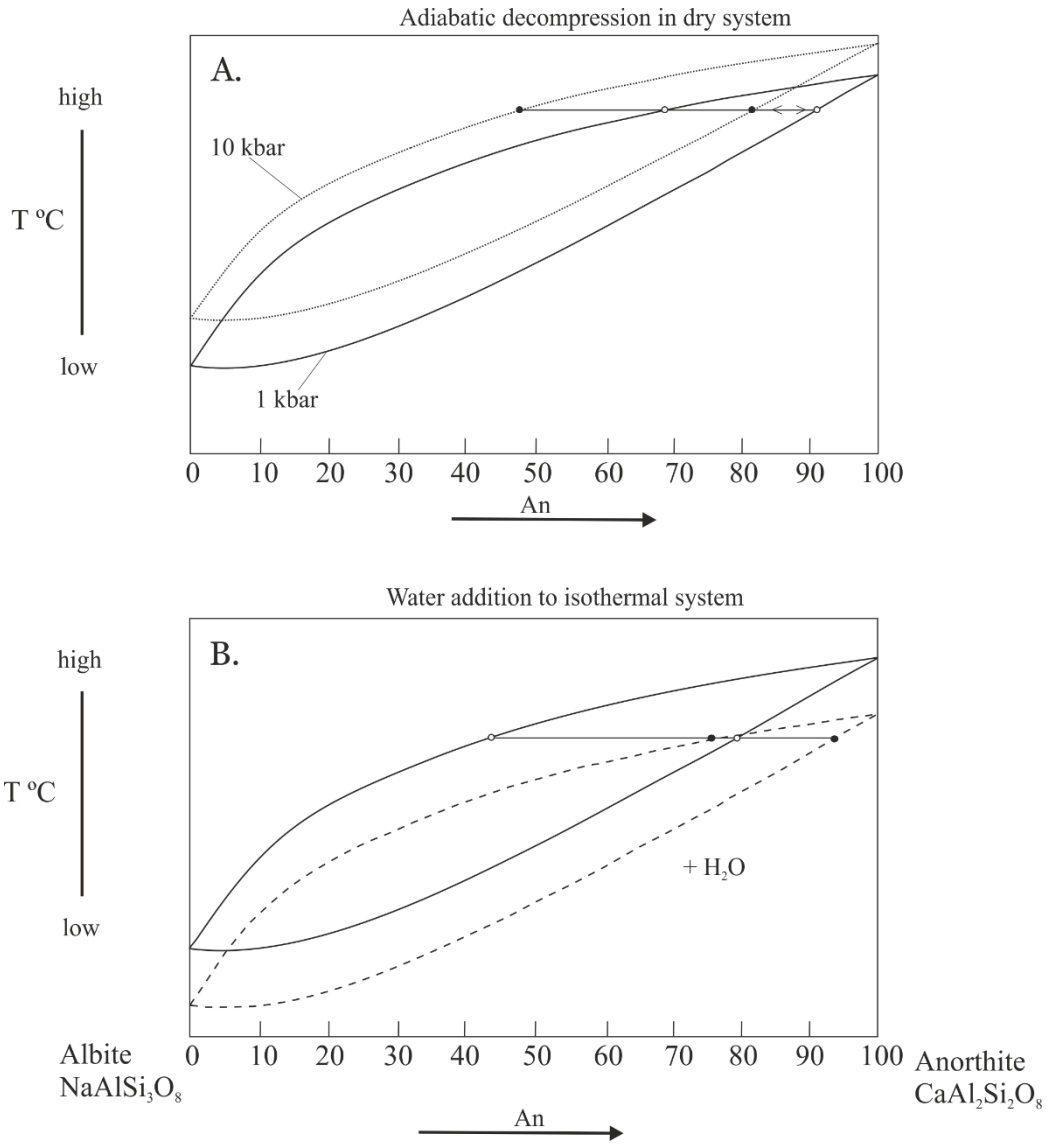

Figure 22. Schematic plagioclase feldspar binary phase diagram (Ab-An). **A.** The effect of decompression from 10 kbar to 1 kbar. Decreasing pressure in isothermal system, plagioclase composition changes to more anorthitic. In polythermal system, temperature decreases with decreasing pressure. **B.** Adding water to isobaric dry system. The more water is added the more albitic plagioclase crystallizes. Temperature decreases as water is added.

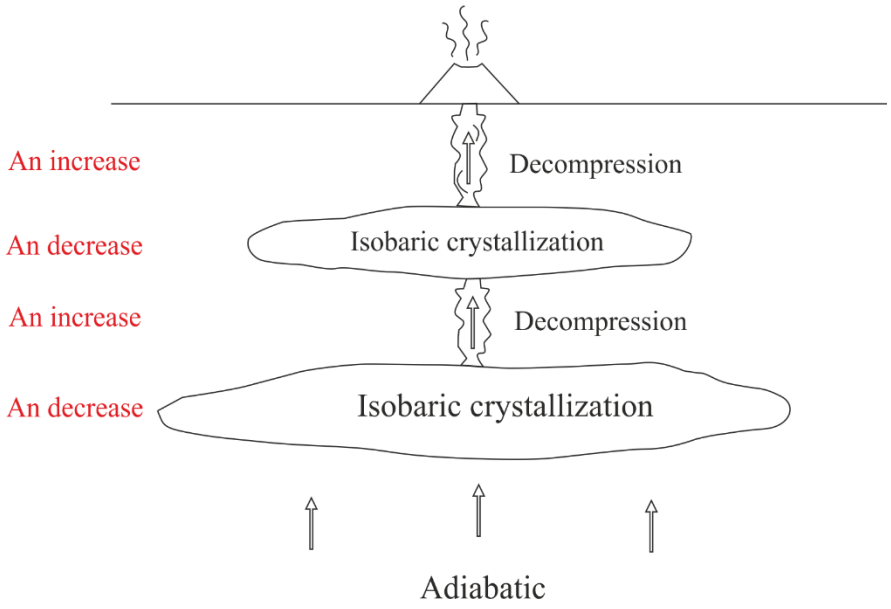

Figure 23. Multistage adiabatic decompression and isobaric repository crystallization model for plagioclase crystallization after Utsunisik et al. (2014). After each stage of decompression, plagioclase crystallizes in decompression and isobarically, eventually generating normal, oscillatory and reverse An zoning.

6.2.3. Influence of water

Increasing water content tends to stabilize more anorthitic plagioclase compared to dry system (Fig. 22-B). The water content of a magma significantly changes the crystallization conditions for plagioclase (Castro et al. 2001, Feig et al. 2006). Solidus temperature can be lowered by >250 ºC when water is added to dry system. In water-saturated synthetic system, pure anorthite crystallizes in lower temperatures than pure albite in the dry system (Yoder et al. 1956, Bowen 1956). The higher the water content and the lower the temperature, the higher An content (~$An_{80–90}$) can be crystallized (Feig et al. 2006). Ginibre and Wörner (2007) suggested that sodic zones in plagioclase may be crystallized in hydrous magma (water saturated) at shallower depth with higher water pressure by degassing and decompression (Blundy and Cashman 2005).

6.2.4. Insight to magma chamber conditions in Luenha

The fluctuating An content in the studied plagioclase phenocrysts in Luenha picrites indicates that the picrites derived from a thermally heterogeneous and possibly polybaric magma chamber system at less than 10 kbar pressure. The effect of water on the crystallization conditions is considered negligible as the initial melt composition for Luenha picrites is considered very low in water (Turunen 2015). The absence of primary

water bearing minerals further demonstrates water deficient crystallization conditions. The only effect of water is seen as completely serpentinized olivines in samples T026B, T026C and T026D, which are the topmost in stratigraphy possibly altered by meteoric water in subsolidus conditions.

To produce reverse and oscillatory zoning during solidification, consecutive cooling and heating events are required. Although the simple cooling system of Bowen (1956) could explain the An range in plagioclase cores, the recognized An zonings require more diverse P-T conditions during magma residence. Alternatively, repetitive magma recharge events or plagioclase migration between a hotter and a cooler magma chamber can temporally increase the temperature of the plagioclase host magma and produce the observed zoning.

Similar An zoning was also produced in the decompression model of Utsunisik et al. (2014). However, the effect of pressure to An content is relatively small compared to the effect of temperature. Generally, calcic plagioclase in basalts is stable around crustal pressures of ≤15 kbar (~60 km) (Ramos et al. 2005) and the Luenha picrites are thought to begun crystallizing at depth of < 55 km (~14 kbar) (Turunen 2015). Ramos et al. (2005) concluded that plagioclase phenocrysts from the Columbia River flood basalt with core compositions of $An_{65–73}$ crystallized at pressures no more than 10 kbar. As the An content increases with decreasing pressure and as the An core contents of Luenha plagioclase phenocrysts range between An_{62}–An_{88}, the crystallization pressures have probably been below 10 kbar, consistent with Turunen (2015).

Pressure decrease can lead to oscillatory and reversely zoned plagioclase (Ginibre and Wörner 2007). According to the phase diagram in Fig. 22-A, adiabatic decompression of 10 kbar (~ ascent of 32 km through continental crust) increases An content on the order of 10 mol% which is in line with Utsunisik et al.'s (2014) thermodynamic model. In theory, some of the small increases in An contents in Luenha phenocrysts could hence be explained by decompression. Thermal heterogeneity could also explain this difference in Luenha phenocrysts, thus decompressions are not necessary but cannot be excluded either.

The wide An range of crystal cores and An zoning in the Luenha plagioclase phenocrysts require a thermally diverse system with rapid heating and cooling of the host magma.

Hence, magma system going through simultaneous contamination and recharge, or plumbing system with isotopically and thermally distinct sections is required. Deep-seated high temperature magma chamber (higher P) connected to cooler chamber in shallower depth (lower P) could have produced the wide anorthite range of plagioclase phenocryst cores and An zoning (and dissolved/resorbed crystal boundaries) in samples from T026C–G. The proportion of the high An plagioclase cores increases up in the Luenha stratigraphy (Fig. 12). The great proportion of high An cores in the latest eruptions could, accordingly, be explained by crystallization in progressively lower pressures, i.e. in shallower crustal depths. The phenocrysts with the lowest An cores could have crystallized in a cooler magma chamber than the ones with the high An cores. If these chambers were connected to a one large magma reservoir prior to eruption, the plagioclases from different magma chambers would be mixed and this could explain the great variety of An core contents within single lava flow (e.g. T026E with core $An_{62–87}$, Fig. 12, Table 2). Many of the observed disequilibrium textures in plagioclase phenocrysts (Fig. 8) support the multiple magma chamber interpretation. The sieved and dissolved phenocryst cores imply physical and chemical instabilities caused by, for example, heat addition (Tsuhciyama 1985, Tepley et al. 1999, Andrews et al. 2008), decompression (Nelson and Montana 1992), rapid undercooling (Castro et al. 2001), or magma mixing (Tepley et al. 1999).

6.3. Isotopic evidence of processes from plagioclase nucleation to subsolidus alteration

The whole-rock ($^{87}Sr/^{86}Sr)_i$ data of Luenha picrites show a great variety from chondritic to radiogenic ratios (Turunen 2015, Fig. 6). The lavas were interpreted to have derived from a common source that was progressively contaminated by continental crust (Turunen 2015). Based on whole-rock data alone, the possible roles of hydrothermal alteration and magma mixing processes cannot be readily evaluated. The in situ data of this study provide more detailed insights into the causes of $^{87}Sr/^{86}Sr$ variation.

6.3.1. Alteration – the effect of hydrothermal fluids

Hydrothermal alteration can affect the $^{87}Sr/^{86}Sr$ composition of a rock by producing more radiogenic ratios by affecting the Rb/Sr values or by introducing isotopically different

fluids, or both. For that reason, subsolidus alteration was considered as a possible cause for the highly radiogenic whole rock $^{87}Sr/^{86}Sr$ ratios of Luenha picrites. Rb is highly mobile in hydrothermal fluids. A fluid with a high Rb/Sr ratio could increase the radiogenic daughter ^{87}Sr content over time, whereas the amount of stable ^{86}Sr remains constant. This increases the $^{87}Sr/^{86}Sr$ ratio, while the initial $^{87}Sr/^{86}Sr$ is not affected, as Sr can be mobile in hydrothermal fluids.

The secondary alteration products of plagioclase are sericite and saussurite (and other micas), the latter of which entrains Sr (Faure and Powell 1972). These alteration minerals are always absent in the analysed Luenha River plagioclase phenocrysts and neither sericite nor saussurite were observed in groundmass plagioclase grains. Overall, the isotopically different plagioclase phenocrysts do not show different styles or degrees at alteration.

Judging from thin-section observations, the isotopic heterogeneity in whole-rock determinations would rather reflect to a magmatic origin than hydrothermal alteration. Subsolidus alteration is not considered to interfere the in situ results of plagioclase phenocrysts and elevation in $^{87}Sr/^{86}Sr$ ratios and thus probably implies assimilation of crustal materials during plagioclase crystallization.

6.3.2. Evidence of crustal contamination in Luenha picrites

The radiogenic isotope compositions of plagioclase phenocrysts and the nonradiogenic composition of uncontaminated picrite T042 show that the Luenha lavas assimilated wall rocks as they erupted through thick continental crust. There is clear isotopic disequilibrium between most plagioclase phenocrysts and their host groundmass and whole rock (Fig. 21, Table 6), which will be discussed in chapter 6.4.1. All the studied plagioclase phenocrysts are less radiogenic than the whole-rock $(^{87}Sr/^{86}Sr)_i$ compositions (Turunen 2015), whereas the bulk groundmass is almost as radiogenic as the whole rock (Fig. 21), reflecting the dominance of groundmass in the whole-rock measurements.

The varying $(^{87}Sr/^{86}Sr)_i$ ratios in plagioclase phenocryst cores within individual lava flows indicate isotopically heterogeneous magmatic system for Luenha picrites. In addition, intracrystal plagioclase growth zones (core to rim) reflect temporally evolving isotope composition of the host magma. These identified isotopic features support the progressive

contamination model of Turunen (2015), but also require interaction with a less radiogenic magma. Magma chambers are typically open systems, where isotopic composition of magma can be changed by contamination, replenishment and eruption (Borges et al. 2014). The magma system must have had isotopically distinct reservoirs to explain all the observed plagioclase phenocryst ($^{87}Sr/^{86}Sr)_i$ ratios.

As crustal country rocks are commonly more silicic and older they have higher $^{87}Sr/^{86}Sr$ isotope compositions compared to basaltic magmas (e.g. Faure and Powell 1972, Andrews et al. 2008). Bulk assimilation of such wall rock or partial melting of Sr enriched minerals can lead to more radiogenic intracrystal core-to-rim $^{87}Sr/^{86}Sr$ ratios during crystal growth and cause isotopic disequilibrium between phenocrysts and groundmass. Continuously erupting picritic melt through a plumbing system could gradually heat the wall rocks, increasing the degree of assimilation in time. In greater depths (lower crust), the host rock would potentially be more mafic, making assimilation more modest in contrast to shallower depth (upper crust), where country rocks would be more felsic, more radiogenic and easier to melt.

The plagioclase phenocryst-free sample T042 has a low $(^{87}Sr/^{86}Sr)_i$ whole rock ratio of 0.7041 (Turunen 2015), giving a reference to a composition of a primitive Luenha picrite, not affected by contamination. Plagioclase phenocryst core $(^{87}Sr/^{86}Sr)_i$ ratios of all the studied lava flows range from mildly radiogenic 0.70511 up to 0.70671. This imply that even the least radiogenic plagioclase phenocrysts have grown from a slightly contaminated magma. The parental magma of Luenha picrites had low initial $^{87}Sr/^{86}Sr$ (like sample T042) being sensitive to contamination, so even a small degree of contamination would have caused the observed increase in $(^{87}Sr/^{86}Sr)_i$ ratios (Faure and Powell 1972).

Although the isotopic range between the flows overlap, there seems to be an increase in the $^{87}Sr/^{86}Sr$ up in stratigraphy, possibly reflecting heterogeneous crustal contamination. The constant heat addition to wall rock would enhance assimilation rate through time, which could explain progressive contamination. However, plagioclases phenocrysts in the basal units (E and G) show more variable $(^{87}Sr/^{86}Sr)_i$ (Table 6).

6.3.3. Evidence of interaction with less radiogenic magma

In addition to contamination, Luenha plagioclases have probably been in contact with less radiogenic magma than the one where they initially nucleated. The radiogenic initial core ratios (0.70648 and 0.70600) of the decreasingly zoned phenocrysts (D-PL-1 and G-PL-1, respectively) imply that interaction with less radiogenic magma (e.g. a recharge pulse, convection or crystal migration) occurred after the beginning of contamination (Tepley and Davidson 2003), and the significantly lower rim ratio of D-PL-1 (Fig. 18-E) indicates a great isotopic difference between the least and the most radiogenic magma system end members. A hotter and less radiogenic magma alters the isotope composition of the host magma towards more primitive ratios during crystal growth (Davidson et al. 1998, Andrews et al. 2008, Font et al. 2008) as observed in some phenocrysts in Luenha picrites (Fig. 18). Additionally, these phenocrysts have the dissolved crystal cores implying physical and chemical instabilities, which can be caused by heat addition (Andrews et al. 2008).

Heat conduction in a silicic melt occurs faster than chemical diffusion (Ginibre and Wörner 2007). Consequently, some phenocrysts might not show chemical changes but record thermal influence (Churikova et al. 2013), as can be seen in the texture of the Luenha plagioclases. Sieve and dissolution textures (Fig. 8) in plagioclase phenocrysts are common in all the Luenha samples. Ginibre and Wörner (2007) and Andrews et al. (2008) have interpreted that strongly sieved plagioclase with dissolution features reflects mixing of thermally distinct magmas. Some of the studied samples are more abundant in sieved phenocrysts (e.g. T026B, Fig. 7) implying crystallization closer to the heat source or stronger incoming heat to the system.

6.4. Complex magma chamber plumbing system of Luenha

Plagioclase phenocryst compositions can help to construct a qualitative model of magma plumbing system for the Luenha. In this schematic model, the plagioclase phenocrysts migrate between compositionally and thermally distinct reservoirs. The migration path depends on the four different evolutionary paths identified from the studied phenocrysts: A) increasing, B) decreasing, C) oscillatory, or D) isotopically homogeneous core-to-rim ($^{87}Sr/^{86}Sr)_i$ ratios (Fig. 15, Fig. 24).

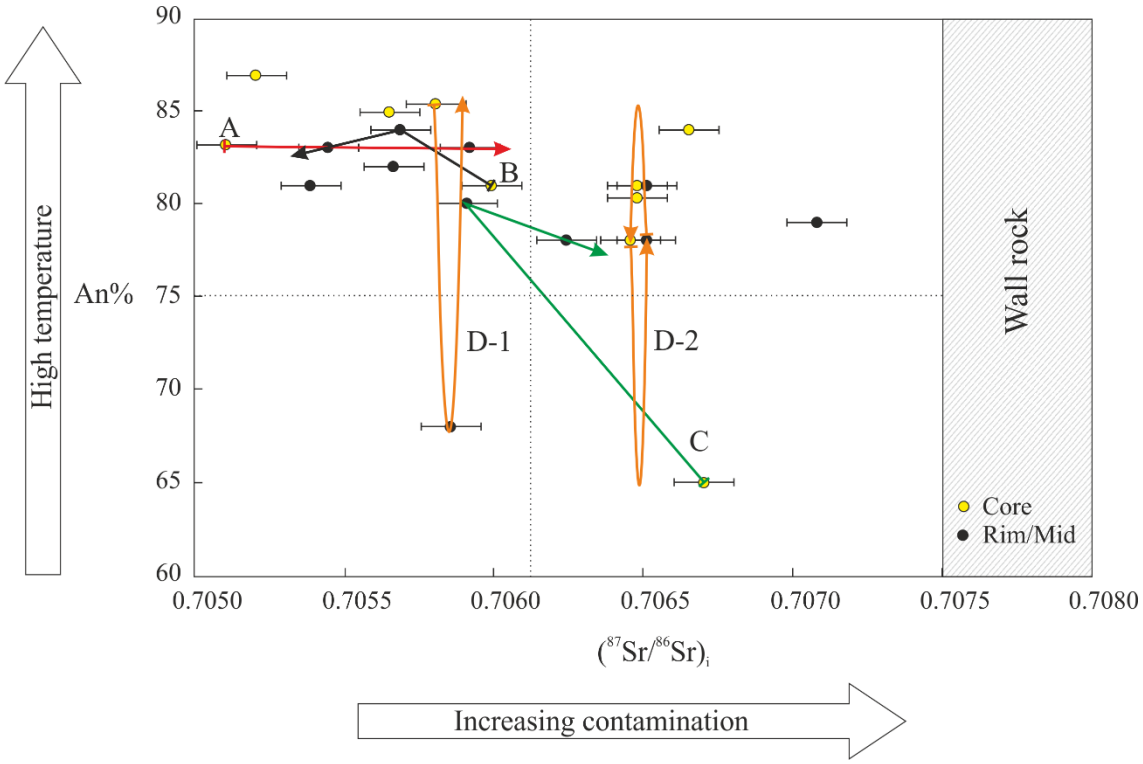

Figure 24. The plagioclase phenocryst migration paths of Luenha picrites after compositional changes from core-to-rim after Figure 15-B in respect to wall rock assimilation and temperature variation.

In the magma plumbing system, magma batches could be emplaced in different country rocks (e.g. mafic and felsic) at different depths, assimilating compositionally variable minerals to generate isotopically heterogeneous melts (Fig. 25). Yet the rock type of contaminant or assimilated mineral assemblages are unknown. The continuous magma ascends and increased heat addition would cause progressive contamination in the reservoirs emplaced in the felsic host rock. Moreover, magmas from separate reservoirs can be pooled and mixed in one large magma reservoir prior eruption to surface.

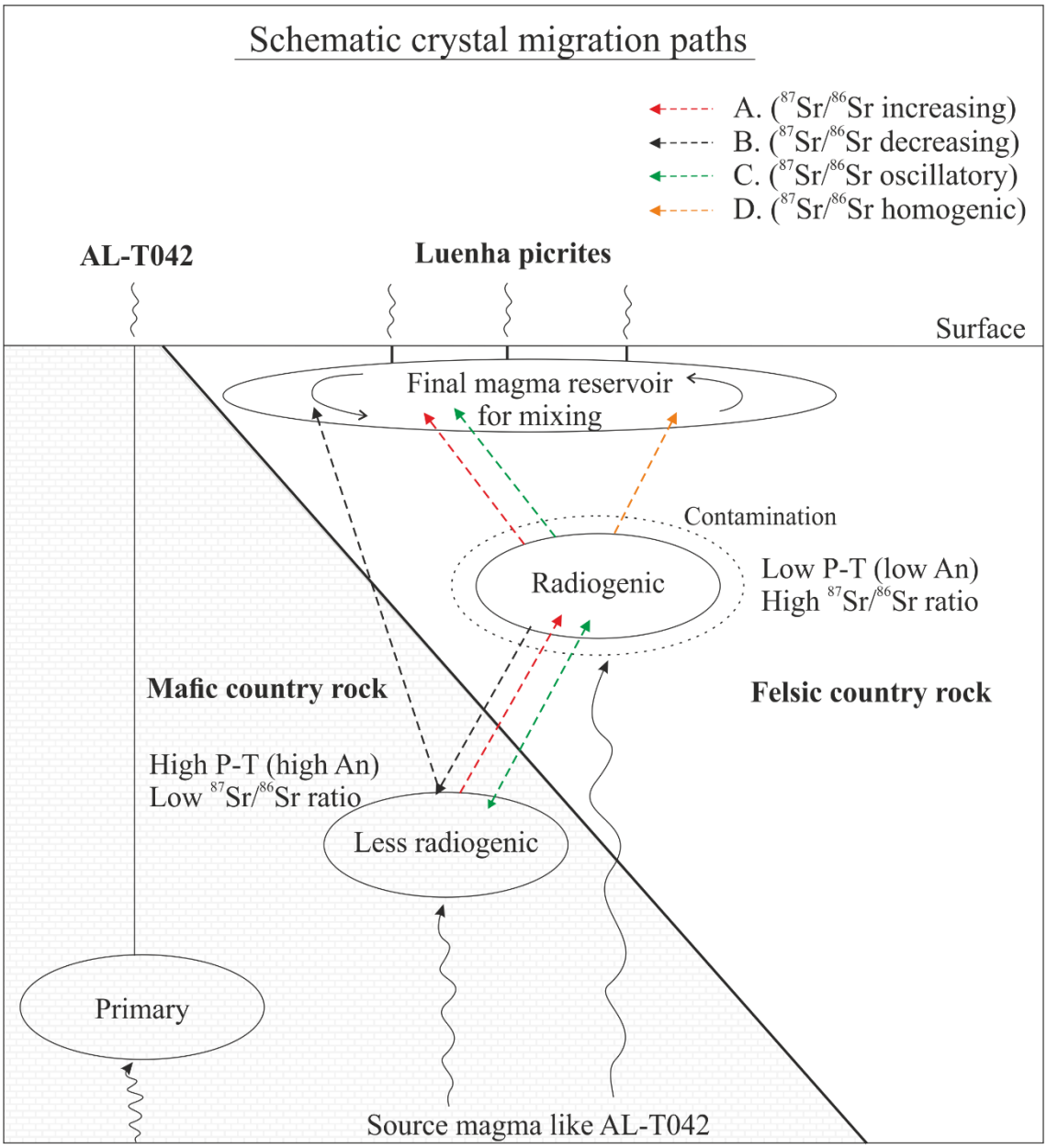

Figure 25. A schematic magma plumbing system of the Luenha picrites based on microsampling results of the studied plagioclase phenocrysts. Different migration paths (A-B) through two chemically different magma reservoirs and the final reservoir for mixing of the different plagioclase types prior eruption. The migration paths (A-D) are the same as discussed in Figure 24. The two distinct magma reservoirs of the plumbing system are emplaced in different host rocks. The less radiogenic reservoir surrounded by mafic country rock is the isotopically less contaminated in higher pressure and temperature conditions. The radiogenic reservoir in lower pressure and temperature conditions is strongly contaminated by the felsic country rock. The primary reservoir has the composition of the primitive plume-like sample AL-T042.

The plagioclases with intracrystal isotopic contamination signature are from the sample T026E, which also includes one isotopically homogeneous plagioclase (E-PL-5a) with oscillating An content (Fig. 17). The isotopically unzoned and zoned plagioclases present a selection of different crystal types scavenged from different parts of the magma system prior to the eruption. Isotopically zoned and nearly unzoned crystals can be crystallized

at the same time if magma system is isotopically layered or otherwise heterogeneous and crystals grew in different sections of the system. Hybridization, assimilation and cooling in magma chambers occur in length scales of 1 to 100's meters (Andrews et al. 2008), which enables plagioclase crystals to nucleate and grow in discrete parts of the system.

Although the selection of the studied plagioclase phenocrysts was intended to be as representative as possible, the most common normal zoned crystals from flow T026D are underrepresented, as are the minority of reversely zoned from flow T026B. The examination of crystals with low An cores from flow T026E are left isotopically unexamined. Two of the studied plagioclase phenocrysts (E-PL-3 and G-PL-1) are not representative of the plagioclase population, and are discussed separately.

The exceptional phenocryst from migration path B, is G-PL-1 (Fig. 18-G, Fig. 25) with distinguishable oval shaped (dissolved) rims has weak compositional An zoning but clear systematic decrease in $(^{87}Sr/^{86}Sr)_i$ from core to rim. The consistent intracrystal $^{87}Sr/^{86}Sr$ decrease imply crystallization in more radiogenic magma prior to emplacing into less radiogenic enclosing melt and later resorption. Decrease in $(^{87}Sr/^{86}Sr)_i$ with relatively constant An content through a large grain suggest that the crystal might have migrated to isotopically different but otherwise compositionally similar and stable environment compared to initiation conditions. Alternatively, a new pulse of compositionally similar but isotopically less radiogenic magma intruded to a chamber. Strongly dissolved phenocryst rims indicate heat addition. The degree of crystallinity of the magma can be partly responsible for maintaining the relatively consistent An content. In the case of a new magma pulse, melt mixing would have been very rapid to produce the relatively homogeneous An composition indicating a melt-dominant magma (crystallinity < 25 %) (Marsh 1996).

The most differentiated phenocryst E-PL-3 (from flow T026E) records more complex evolution events, where both $(^{87}Sr/^{86}Sr)_i$ and An are oscillatory (migration path C) (Fig. 19, Fig. 25). A compilation of events discussed earlier could be adapted here, emphasizing the compositionally distinct parts in a chamber or distinct but connected chambers. This type of crystal might be supplied from more evolved and radiogenic chamber (core An_{62}) into more primitive magma, consequently re-equilibrating with the host magma (decrease in $^{87}Sr/^{86}Sr$ ratio, sieve texture and Ca-rich zone) and then migrated again near the

contamination (increase in $(^{87}Sr/^{86}Sr)_i$). A wide range between zones (from An_{62} to An_{80}) requires high and sudden changes in temperature back and forth, most likely reflecting a heating event of a new hot magma pulse and eruption.

6.4.1. Eruption timescales

Timescales of differentiation events taking place during Luenha magma migration can be qualitatively evaluated from the strontium diffusion rates. In order to retain the observed isotopic disequilibrium in the Luenha picrites, crustal residence times for magma must have been short, on the order of <500 years (Andrews et al. 2008). Sr diffusion is fast in high temperature magmatic environment and Sr isotope ratio would re-equilibrate through isotopic exchange between plagioclase phenocrysts and surrounding melt eventually neutralizing the disequilibrium (Ramos et al. 2005, Allègre 2008).

The disequilibria between the plagioclase phenocrysts and groundmass was found to be magmatic suggesting that the phenocrysts did not crystallize from the same liquid with the groundmass (Munoz et al. 2016). The groundmass has likely recorded the contamination that occurred in the final magma reservoir. Ramos et al. (2005) estimated crustal residence times for Columbia River Basalts with the Sr diffusion model. They concluded that the isotopic re-equilibration between plagioclase and melt occurs within years to few decades' time, homogenizing the magma. In addition, plagioclase growth and strontium diffusivity ends after eruption when magma cools disabling further Sr diffusion (Allègre 2008).

For the Luenha picrites this means that, if phenocrysts migrate between isotopically distinct sections of the magma system or within isotopically layered chamber, it would happen within the same timescales. The Luenha magmas resided in the different isotopic reservoirs only for short periods and the final eruptions took place closely after, avoiding isotope re-equilibration between phenocrysts and more radiogenic groundmass. The uncontaminated and plagioclase free sample T042 has probably erupted rapidly through more cold or mafic crust avoiding *en route* contamination.

6.5. Implications for the North Karoo lavas

6.5.1. The North Karoo source

This study does not have the means to constrain the primary magma composition nor the origin of the Luenha-type North Karoo source, but provide a platform to discuss the diversity of sources from the plagioclase point of view. The data generated in this study supports the previous theory that Luenha picrites originated from a fairly uniform source affected by heterogeneous contamination. The detailed in situ isotopic measurements suggest that contamination occurred both during magma residence in complex plumbing system and *en route* to eruption.

The core ($^{87}Sr/^{86}Sr)_i$ ratios of the studied plagioclase phenocrysts (0.70511–0.70671) are notably higher than MORB ratios ($^{87}Sr/^{86}Sr$ for 0.7022−0.7034; Allègre 2008) and slightly higher than OIB ratios ($^{87}Sr/^{86}Sr$ for 0.7030−0.7050; Allègre 2008). The most primitive sample from Luenha, olivine cumulate T042 has OIB-like isotope ratio (0.7041; Turunen 2015), and the most primitive plagioclase phenocryst from the sample T026E (PL-4) has core ($^{87}Sr/^{86}Sr)_i$ ratio of 0.7051 falling very close to OIB. Thus, the low but slightly more radiogenic ratio of E-PL-4 could be inherited from slightly contaminated mantle plume or contaminated upper mantle (MORB) source. The positive ΔNb of the Luenha lavas favors the mantle plume source (Luttinen 2018).

The radiogenic $^{87}Sr/^{86}Sr$ of CFBs is commonly thought to be inherited from old SCLM (Greenough et al. 1989, Peate and Hawkesworth 1996) or from the isolated non-convecting part of the mantle (lHawkesworth et al. 1988). The heterogeneous SCLM is not likely source for the North Karoo lavas because of their relatively homogeneous geochemical composition (Luttinen 2018). NMORB-like source contaminated with SCLM cannot produce the geochemical features of the Luenha-type North Karoo lavas either (Turunen 2015). The SCLM below southern Zimbabwe Craton has been proved old (meso-Archean), and anomalously depleted (Smith et al. 2009). The least radiogenic isotopic data of the plagioclase cores from the Luenha does not favour SCLM, unless the SCLM under Zimbabwe craton is so depleted in Rb that $^{87}Sr/^{86}Sr$ ratios were low. The low TiO_2 content of Luenha picrites neither favors SCLM source (Turunen 2015) and it is unlikely to that the depleted old SCLM could melt in high enough degree to produce the voluminous North Karoo lavas (Arndt and Christensen 1992).

Following the above reasoning, a mantle plume source from convective mantle is more prominent for the Luenha-type North Karoo lavas, as it can explain the low core ($^{87}Sr/^{86}Sr)_i$ ratios found from some of the studied plagioclase phenocrysts. This correlates with the results that imply a plume source for the North Karoo lavas (Luttinen 2018), although in the case of Luenha picrites the plume fingerprints seem to be strongly overprinted by progressive contamination. The most primitive picrite T042 potentially represents the parental magma type of North Karoo, and preliminary results of an ongoing $^{187}Os/^{188}Os$ isotopic study supports a convective mantle source (personal communication Sanni Turunen 2018).

6.5.2. Adjustment on the contamination process

This study provides crucial details to petrogenesis of the Luenha picrites. The in situ microsampling results of plagioclase phenocrysts corroborate the conclusions of Turunen (2015) and shows more explicitly how the contamination proceeded. The interpretation of this study is that contamination started before the onset of plagioclase crystallization and the isotopically diverse phenocryst cores showed a temporally increasing contamination up in stratigraphy. A feasible explanation could be that wall-rock assimilation was very modest at the beginning, causing only minor addition of ^{87}Sr to the melt. While magma adiabatically raised to shallower depths, assimilation favored more radiogenic phases such as micas to melt.

The most radiogenic phenocryst cores record the late stages of magma evolution, characterized by prominent contamination, whereas the least radiogenic phenocryst cores could record much earlier stages. T026E could be the only flow recording the early stages of the system evolution, at the initiation of the progressive contamination. The most radiogenic phenocryst (B-PL-3) with $(^{87}Sr/^{86}Sr)_i$ ratio of 0.70709 (Fig. 20-I) is from flow T026B. The An content and zoning of this plagioclase are similar with other oscillating less radiogenic plagioclases making no exception. These observations suggest that B-PL-3 crystal has grown from magma with same chemical composition but nearby the contamination source e.g. chamber wall or roof (Meade et al. 2014).

The contaminant had either chondritic $^{143}Nd/^{144}Nd$ ratio with high $^{87}Sr/^{86}Sr$ ratio, low Nd concentration and high Sr concentration, or a composition such where Nd is compatible and Sr is incompatible during partial melting in order to produce similar ratios that are

observed in Luenha bulk analyses. To answer how much contamination is required to change the $^{87}Sr/^{86}Sr$ ratios from 0.704 to 0.707 would require energy constrained modelling (e.g. EC-AFC modelling). Models need rigorous evaluation of the prominent contaminants and their mineralogy to understand isotopic evolution and the composition of parent magma.

7. CONCLUSIONS

1. The previously observed heterogeneity in whole-rock strontium $(^{87}Sr/^{86}Sr)_i$ in Luenha picrites is not caused by subsolidus alteration of hydrothermal fluids. The range in $(^{87}Sr/^{86}Sr)_i$ is inherited from magmatic events during evolution of Luenha lavas.

2. The crystallization conditions (T-P-X_{H2O}) of Luenha picrites were dynamic, changing throughout the crystallization history. The compositional variation in plagioclase crystals imply strong temperature controlled crystallization conditions with possible minor effect of decompression.

3. In addition to unveiling temporally progressing contamination of more radiogenic country rocks, interaction with less radiogenic magma during plagioclase growth was also revealed with microsampling plagioclase growth zones. Relatively radiogenic plagioclase cores compared to the uncontaminated, plagioclase-free sample AL-T042 imply that the contamination had already begun prior the initiation of plagioclase crystallization. This emphasizes that crustal contamination is an important process in generating isotopic heterogeneity in Luenha picrites.

4. The diverse compositional evidence of plagioclase phenocrysts within and between lava flows suggests complex and isotopically heterogeneous magma plumbing system, where magma migrates between connected but compositionally diverse magma reservoirs. Assimilating different mineral assemblages with different isotope compositions from different country rocks introduces complexity to magma compositon.

5. This study of the plagioclase phenocrysts shows that the magma source of Luenha picrites has been less radiogenic than interpreted from the whole-rock data. The most primitive plagioclase core in Luenha picrites has a $^{87}Sr/^{86}Sr$ close to OIB and MORB,

suggesting a genetic link to a plume source. However, in most of the examined samples the plume signature is overprinted by contamination.

6. The whole Karoo CFB province lacks detailed in situ studies, and the methodology introduced in this work could be adapted for North Karoo examination.

8. ACKNOWLEDGEMENTS

I would like to address my gratitude to the VALVE team for the opportunity to study these very interesting picrites samples, and my supervisors Arto Luttinen and Tapani Rämö and Sanni Turunen for constructive comments and feedback. To Yann Lahaye I thank for helping and allowing me to practice MC-LA-ICP-MS at GTK, and Radoslaw Michallic for sample preparation and EPMA instructions at University of Helsinki. Ville Virtanen is thanked for “Piano lessons”, mental stabilization and brainstorming.

REFERENCES

Allègre, C.J. 2008. Isotope geology. Cambridge university press, The Edinburgh building, United Kindom. p. 507.

Anderson, D.L. 1994. Superplumes or supercontinents? Geology 22, 39–42.

Andrews, B.J., Gardner, J.E. and Housh, T.B. 2008. Repeated recharge, assimilation, and hybridization in magmas erupted from El Chichón as recorded by plagioclase and amphibole phenocrysts. Journal of Volcanology and Geothermal Research 175, 415–426.

Arndt, N.T., Czamanske, G.K., Wooden, J.L. and Fedorenko, V.A. 1993. Mantle and crustal contributions to continental flood volcanism. Tectonophysics 223, 39–52.

Arndt, N.T. and Christensen, U. 1992. The role of lithospheric mantle in continental flood volcanism: Thermal and geochemical constraints. Journal of Geophysical Research 97, 10967–10981.

Beccaluva, L., Bianchini, G., Natali, C. and Siena, F. 2009. Continental flood basalts and mantle plumes: a case study of the northern Ethiopian Plateau. Journal of Petrology 50, 1377–1403.

Bender, F.F., Hodges, F.N. and Bence, A.E. 1978. Petrogenesis of basalts from the project FAMOUS area: experimental study from 0 to 15 kbars. Earth and Planetary Science Letters 41, 277–302.

Blundy, J. and Cashman, K. 2005. Rapid decompression-driven crystallization recorded by melt inclusions from Mount St. Helens volcano. Geological Society of America 33, 739–796.

Borges, M.R., Sen, G., Hart, G.L., Wolff, J.A. and Chandrasekharam, D. 2014. Plagioclase as recorder of magma chamber processes in the Deccan Traps: Sr-isotope zoning and implications for Deccan eruptive event. Journal of Asian Earth Sciences 84, 95–101.

Borghini, G., Fumagalli, P. and Rampone, E. 2010. The stability of plagioclase in the upper mantle: subsolidus experiments on fertile and depleted lherzolite. Journal of Petrology 51, 229–254.

Bowen, N.L. 1956. The evolution of the ingenous rocks. Dover Publications, inc. p. 332.
Browne, B.L., Eichelberger, J.C., Patino, L.C., Vogel, T.A., Uto, K. and Hoshizumi, H. 2006. Magma mingling as indicated by textures and Sr/Br ratios of plagioclase phenocrysts from Unzen volcano, SW Japan. Journal of Volcanology and Geothermal Research 154, 103–116.
Bryan, S.E. and Ernst, R.E. 2008. Revised definition of large igneous provinces (LIPs). Earth-Science Reviews 86, 175–202.
Campbell, I.H. and Griffiths, R.W. 1990. Implication of mantle plume structure for the evolution of flood basalts. Earth and Planetary Science Letters 99, 79–93.
Carlson, R.W., Lugmair, G.W. and Macdougall, J.D. 1981. Columbia River volcanism: the question of mantle heterogeneity or crustal contamination. Geochimica and Cosmochimica Acta 42, 2483–2499.
Carlson, R.W. 1991. Physical and chemical evidence on the cause and source characteristics of flood basalt volcanism. Australian Journal of Earth Sciences 38, 525–544.
Castro, A. 2001. Plagioclase morphologies in assimilation experiments. Implication for disequilibrium melting in the generation of granodiorite rocks. Mineralogy and Petrology 71, 31–49.
Coffin, M.F. and Eldholm, O. 1994. Large igneous provinces: crustal structure, dimensions, and external consequences. Reviews of Geophysics 32, 1–36.
Courtillot, V.E. and Renne, P.R. 2003. On the ages of flood basalt events. Comptes Rendus Geosciences 335, 113–140.
Cox, K.G., MacDonald, R. and Hornung, G. 1967. Geochemical and petrographic provinces in the Karoo basalts of southern Africa. The American Mineralogist 52, 1451–1474.
Cox, K.G. 1988. The Karoo province. In: J.D. Macdougall (Editor), Continental Flood Basalts. Kluwer, Dordrecht, 239–272.
Churikova, T.G., Ivanov, B.V., Eichelberger, J., Wörner, G., Browne, B. and Izbekov, P. 2013. Major and trace element zoning in plagiolcase from Kizimen volcano (Kamchatka): insights into magma-chamber processes. Journal of Volcnaology and Seismology 7, 112–130.
Davidson, J.P. and Tepley, F.J. III. 1997. Recharge in volcanic systems: evidence from isotope profiles of phenocrysts. Science 275, 826–829.
Davidson, J.P., Tepley, F.J., III and Knesel, K.M. 1998. Isotopic fingerprinting may provide insights into evolution of magmatic systems. EOS Transactions, American Geophysical Union 79, 185–196.
Deer, W.A., Howie R.A. and Zussmann J. 1963. Rock-forming minerals, Vol.4 Framework Silicates. Logmans, Great Britain p. 435.
DePaolo, D.J. 1981. Trace element and isotopic effects of combined wallrock assimilation and fractional crystallization. Earth and Planetary Science Letters 53, 189–202.
Duncan, R.A., Hooper, P.R., Rechacek, J., Marsh, J.S. and Duncan, A.R. 1997. The timing and duration of the Karoo igneous event, southern Gondwana. Journal of Geophysical Research 102, 127–138.
Ellam, R.M., Carlson, R.W. and Shirey, S.B. 1992. Evidence from Re-Os isotopes for plume-lithophere mixing in Karoo flood basalt genesis. Letters to Nature 359, 718–721.
Faure, G. and Powell, J.L. 1972. Strontium isotope geology. Minerals Rocks and inorganic material, monograph series of theoretical and experimental studies 5 (Edit) Von Engelhardt W., and Hahn T. Pub. Springer-Verlag Belrin, Heidelberg New York. p. 188.
Feig, S.T., Koepke, J. and Snow, J. 2006. Effect of water on tholeiitic basalt phase equilibria: an experimental study under oxidizing conditions. Contributions to Mineralogy and Petrology 152, 611–638.
Fitton, J.G., Saunders, A.D., Norry, M.J., Harsarson, B.S. and Taylor, R.N. 1997. Thermal and chemical structure of the Iceland plume. Earth and Planetary Scinece Letters 153, 197–208.
Foland, K.A., Gibb, F.G.F. and Henderson, C.M.B. 2000. Patterns of Nd and Sr isotopic ratios produced by magmatic and post-magmatic processes in the Shiant Isles Main Sill, Scotland. Contribution to Mineralogy and Petrology 139, 655–671.
Font, L., Davidson, J.P., Pearson, D.G., Nowell, G.M., Jerram, D.A. and Ottley, C.J. 2008. Sr and Pb Isotope micro-analysis of plagioclase crystals from Skye lavas: an insight into open-system processes in a flood basalt province. Journal of Petrology 49, 1449–1471.

Ghiorso, M.S. and Sack, R.O. 1994. Chemical mass transfer in magmatic processes IV. A revised and internally consistent thermodynamic model for the interpolation and extrapolation of liquid-solid equilibria in magmatic systems at elevated temperatures and pressures. Contribution to Mineralogy and Petrology 119, 197–212.

Ginibre, C., Wörner, G. and Kronz, A. 2002. Minor- and trace-element zoning in plagioclase: implications for magma chamber processes at Parinacota volcano, northern Chile. Contribution to Mineralogy and Petrology 143, 300–315.

Ginibre, C. and Wörner, G. 2007. Variable parent magmas and recharge regimes of the Parinacota magma system (N. Chile) revealed by Fe, Mg and Sr zoning in plagioclase. Lithos 98, 118–140.

Ginibre, C. and Davidson, J. 2014. Sr isotope zoning in plagioclase from Parinacote volcano (northern Chile): quantifying magma mixing and crustal contamination. Journal of Petrology 55, 1203–1238.

Greenough, J.D., Jones, L.M. and Mossman, D.J. 1989. The Sr isotopic composition of Early Jurassic mafic rocks of Atlantic Canada: Implication for assimilation and injection mechanisms affecting mafic dykes. Chemical Geology (Isotope Geoscience Section) 80, 17–26.

Grove, T.L., Baker, M.B. and Kinzler, R.J. 1984. Coupled CaAl-NaSi diffusion in plagioclase feldspar: Experiments and applications to cooling rate speedometry. Geochimica et Cosmochimica Acta 48, 2113–2121.

Hawkesworth, C.J., Mantovani, M.S.M., Taylor, P.N. and Palacz, Z. 1986. Evidence from the Parana of south Brazil for a continental contribution to Dupal basalts. Nature 322, 356–359.

Hawkesworth, C.J. Mantovani, M. and Peate, D. 1988. Lithosphere Remobilization during Paraná CFB Magmatism. Journal in Petrology, Special Lithospehre Issue, 205–223.

Heinonen, J.S., Carlson, R.W., Riley, T.R., Luttinen, A.V. and Horan, M.F. 2014. Subduction-modified oceanic crust mixed with a depleted mantle reservoir in the sources of the Karoo continental flood basalt province. Earth and Planetary Science Letters 394, 229–241.

Housh, T.B. and Luhr, J.F. 1991. Plagioclase-melt equilibria in hydrous systems. American Mineralogist 76, 477–492.

Jackson, M.G. and Carlson, R.W. 2011. An ancient recipe for flood-basalt genesis. Nature 476, 316–319.

Jochum, K.P., Stoll, B., Weis, U., Kuzmin, D.V. and Sobolev, A.V. 2009. In situ Sr isotopic analysis of low Sr silicates using LA-ICP-MS. Journal of Analytical Atomic Spectrometry 24, 1237–1243.

Jourdan, F., Féraud, G., Bertrand, H., Kampunzu, A.B., Tshoso, G., Watkeys, M.K. and Le Gall, B. 2005. Karoo large igneous province: brevity, origin, and relation to mass extinction questioned by new $^{40}Ar/^{39}Ar$ age data. Geological Society of America 33, no 9, 745–748.

Jourdan, F., Bertrand, H., Schaerer, U., Blichert-Toft, J., Féraud, G. and Kampunzu, A. B. 2007a. Major and trace element and Sr, Nd, Hf, and Pb isotope compositions of the Karoo large igneous province, Botswana–Zimbabwe: lithosphere vs mantle plume contribution. Journal of Petrology 48, 1043–1077.

Jourdan, F., Féraud, G., Bertrand, H., Watkeys, M.K. and Renne, P.R. 2007b. Distinct brief major events in the Karoo large igneous province clarified by new $^{40}Ar/^{39}Ar$ ages on the Lesotho basalts. Lithos 98, 195–209.

Jourdan, F., Féraud, G., Bertrand, H., Watkeys, M.K. and Renne, P.R. 2007c. From flood basalts to the inception of oceanization: example from the $^{40}Ar/^{39}Ar$ high-resolution picture of the Karoo large igneous province. Geochemistry, Geophysics. Geosystems 8.

Kamenetsky, V.S., Maas, R., Kamenetsky, M.B., Yaxley, G.M., Ehrig, K., Zellmer, G.F., Bindeman, I.N., Sobolev, A.V., Kuzmin, D.V., Ivanov, A.V., Woodhead, J. and Schilling, J.G. 2017. Multiple mantle sources of continental magmatism: Insights from “high-Ti” picrites of Karoo and other large igneous provinces. Chemical Geology 455, 22–31.

Kent, R.W., Storey, M. and Saunders, A.D. 1992. Large igneous provinces: sites of plume impact or plume incubation? Geology 20, 891–894.

King, S.D. and Anderson, D.L. 1995. An alternative mechanism of flood basalt formation. Earth and Planetary Science Letters 139, 269–279.

Korenaga, J. 2004. Mantle mixing and continental breakup magmatism. Earth and Planetary Science Letters 218, 463–473.

Le Bas, M.J. 2000. IUGS Reclassification of the high-Mg and picritic volcanic rocks. Journal of Petrology 41, 1467–1470.

Lenardic, A., Moresi, L., Jellinek, A.M., O'Neill, C.J., Cooper, C.M. and Lee, C.T. 2011. Continents, supercontinents, mantle thermal mixing, and mantle thermal isolation: Theory, numerical simulation, and laboratory experiments. Geochemistry, Geophysics, Geosystems 12, 1–23.

Lightfoot, P.C., Hawkesworth, C.J., Hergt, J., Naldrett, A.J., Gorbachev, N.S., Federenko, V.A. and Doherty, W. 1993. Remobilisation of the continental lithosphere by a mantle plume: major-, trace-element, and Sr-, Nd-, and Pb-isotope evidence from picritic and tholeiitic lavas of the Noril'sk District, Siberian Trap, Russia. Contribution to Mineraloly and Petrology 114, 171–188.

Luttinen, A.V., Heinonen, J., Kurhila, M., Jourdan, F., Mänttäri, I., Vuori, S. and Huhma, H. 2015. Depleted mantle-sourced CFB magmatism in the Jurassic Africa-Antarctica rift: Petrology and $^{40}Ar/^{39}Ar$ and U/Pb chronology of the Vestfjella dyke swarm, Dronning Maudland, Antarctica. Journal of Petrology. Electronical publishment doi:10.1093/petrology/egv022.

Luttinen, A.V. 2018. Bilateral geochemical asymmetry in the Karoo large igneous province. Nature, Scientific reports 8, 1–11.

Manninen, T., Eerola, T., Mäkitie, H., Vuori, S., Luttinen, A., Sénvano, A. and Manhica, V. 2008. The Katoo volcanic rocks and related intrusions in southern and central Mozambique. Geological Survey of Finland, Special paper 48, 211–250.

Marsh, B.D. 1996. Solidification fronts and magmatic evolution. Mineralogical Magazine 60, 5–40.

Meyer, R., van Wijk, J. and Gernigon, L. 2007. The North Atlantic Igenous Province: a review of models for its formation. The Geological Society of America 430, 525–552.

Meade, F.C., Troll, V.R., Ellam, R.M., Freda, C., Font, L., Donaldson, C.H. and Klonowska, I. 2014. Bimodal magmatism produced by progressively inhibited crustal assimilation. Nature Communications 5, 1–11.

Morgan, W.J. 1971. Convection plumes in the lower mantle. Nature 230, 42–43.

Munoz, P.M., Alves, A., Azzone, R.G., Cordenons, P., Morano, S., Sproesser, W. and de Souza, S. 2016. In situ Sr isotope analyses by LA-MC-ICP-MS of igneous apatite and plagioclase from magmatic rocks at the CPGeo-USP. Brazilian Journal of Geology 46, 227–243.

Müller, W., M. Shelley, Miller, P. and Broude, S. 2009. Initial performance metrics of a new custom-designed ArF excimer LA-ICPMS system coupled to a two-volume laser-ablation cell. Journal of Analytical Atomic Spectrometry 24, 209–214.

Nelson, S.T. and Montana, A. 1992. Sieve-textured plagioclase in volcanic rocks produced by rapid decompression. American Mineralogist 77, 1242–1249.

Peate, D.W. and Hawkesworth, C.J. 1996. Lithospheric to asthenospheric transition in Low-Ti flood basalts from southern Paraná, Brazil. Chemical Geology 127, 1–24.

Pearce, T.H. and Kolisnik, A.M. 1990. Observations of plagioclase zoning using interference imaging. Earth-Science Reviws 29, 9–26.

Pekkala, Y., Lehto, T. and Lehtonen, M.I. 2008. Intorduction to GTK projects in Mozambique 2002−2007. Geologian survey of Finland, Special Paper 48, 7–22.

Peyve, A.A. 2015. The role of mantle plumes in the evolution of the African segment of Pangea and the formation of the Atlantic Ocean. Geotectonics 49, 379–394.

Pik, R., Deniel, C., Coulon, C., Yirgu, G. and Marty, B. 1999. Isotopic and trace element signatures of Ethiopian flood basalts: Evidence for plume-lithosphere interactions. Geochimica et Cosmochimica Acta 63, 2263–2279.

Pouchou, J.L. and Pichoir, F. 1984. A new model for quantitative X-ray microanalysis. La Recherce Aerospatiale 3, 167–192.

Ramos, F.C, Wolff, J.A. and Tollstrup, D.L. 2004. Measuring $^{87}Sr/^{86}Sr$ variations in minerals and groundmass from basalts using LA-MC-ICPMS. Chemical Geology 211, 135–158.

Ramos, F.C, Wolff, J.A. and Tollstrup, D.L. 2005. Sr isotope disequilibrium in Columbia River flood basalts: Evidence for rapid shallow-level open-system processes. Geological Society of America 33, 457–460.

Rankenburg, K., Lassiter, J.C. and Brey, G. 2004. Origin of megacrysts in volcanic rocks of the Cameroon volcanic chain - constraints on magma genesis and crustal contamination, Contribution to Mineralogy and Petrology 147, 129–144.

Renne, P.R., Zichao, Z., Richards, M.A., Black, M.T. and Basu, A.R. 1995. Synchrony and causal relations between Permia-Triassic boundary crises and Siberian flood volcanism. Science 269, 1413–1417.

Richards, M.A., Duncan, R.A. and Courtillot, V.E. 1989. Flood basalts and hot-spot tracks: plume heads and tails. Science 246, 103–107.

Rogers, G.C. 1982. Ocenanic plateaus as meteorite impact signatures. Nature 299, 341–342.

Rollinson, H.R. 1993. Using Geochemical Data: Evaluation, Presentation, Interpretation. Longman, London, 352 p.

Silver, P.G., Behn, M.D., Kelley, K., Schmitz, M. and Savage, B. 2006. Understanding cratonic flood basalts. Earth and Planetary Science Letters 245, 190–201.

Smith, C.B., Pearson, G.D., Bulanova, G.P., Beard, A.D., Carlson, R.W., Wittig, N., Sims K., Chimuka, L. and Muchemwa, E. 2009. Extremely depleted lithospheric mantle and diamonds beneath the southern Zimbabwe Craton. Lithos 112S, 1120–1132.

Sweeney, R.J., Falloon, T.J., Green, D.H. and Tatsumi, Y. 1991. The mantle origins of Karoo picrites. Earth and Planetary Science Letters 107, 256–271.

Taylor, H.P., Jr. 1980. The effects of assimilation of country rocks by magmas on $^{18}O/^{16}O$ and $^{87}Sr/^{86}Sr$ systematics in igneous rocks. Earth and Planetary Science Letters 47, 243–254.

Tepley, III F.J., Davidson, J.P. and Clynne, M.A. 1999. Magmatic interactions as recorded in plagioclase phenocrysts of Cahos Crags, Lassen Volcanic Center, California. Journal of Petrology 40, 787–806.

Tepley, III F.J. and Davidson, J.P. 2003. Mineral-scale Sr-isotope constraints on magma evolution and chamber dynamics in the Rum layered intrusion, Scotland. Contribution to Mineralogy and Petrology 145, 628–641.

Thirlwall, M.F. 1991. Long-term reproducibility of multicollector Sr and Nd isotope ratio analysis. Chemical Geology 94, 85–104.

Tsuchiyama, A. 1985. Dissolution kinetics of plagioclase in the melt of the system diopside-albite-anorthite, and origin of dusty plagioclase in andeseites. Contribution to Mineralogy and Petrology 89, 1–16.

Turunen, S. 2015. Mosambikin Luenha-joen pikriittilaavojen petrologinen, mineraloginen ja geokemiallinen tutkimus: uusia johtolankoja Karoon magmaprovinssin laakiobasalttien vaippalähteestä. Master's Thesis, University of Helsinki, Department of Geosciences and Geography. 85 (96) p.

Ustunisik, G., Kilinc, A. and Nielsen, R.L. 2014. New insights into the processes controlling compositional zoning in plagioclase. Lithos 200–201, 80–93.

White, R.S. and McKenzie, D. 1989. Magmatism at rift zones: the generation of volcanic continental margins and flood basalts. Journal of Geophysical Research 94, 7685–7729.

Yoder, H.S., Stewart, D.B. and Smith, J.R. Feldspars. 1956. Carnegie Institution of Washington, Yearbook 56, 206–214.

APPENDIX A: PLAGIOCLASE EPMA DATA, AL-T026B

APPENDIX B: PLAGIOCLASE EPMA DATA, AL-T026C

APPENDIX C: PLAGIOCLASE EPMA DATA, AL-T026D

APPENDIX D: PLAGIOCLASE EPMA DATA, AL-T026E

APPENDIX E: PLAGIOCLASE EPMA DATA, AL-T026G

APPENDIX F: PLAGIOCLASE EPMA DATA, AL-T042

APPENDIX A. Microprobe analyses of plagioclase phenocrysts and groundmass plagioclase grains of sample AL-T026B.

Grain	PL-5-1				PL-3-1				PL-4-1		PL-11-1			PL-12-1		PL-9a-1	
Spot	plg59	plg60	plg61	plg62	plg63	plg64	plg65	plg66	plg67	plg68	plg70	plg71	plg72	plg74	plg75	plg76	plg77
Location	Core*	Mid	Rim*	Mid	Core*	Core	Mid	Rim*	Mid	Mid	Core*	Mid	Rim*	Core*	Mid	Core*	Rim*
SiO_2	50.22	48.70	45.93	46.06	47.84	47.48	46.09	45.89	46.94	46.12	48.17	45.89	45.61	47.72	46.84	46.34	47.14
TiO_2	0.06	0.00	0.00	0.00	0.03	0.04	0.00	0.00	0.14	0.00	0.16	0.01	0.04	0.00	0.00	0.17	0.00
Al_2O_3	30.31	31.24	33.44	33.69	32.20	32.38	33.39	33.48	32.79	33.00	31.38	33.31	33.31	32.48	32.39	32.17	32.57
Fe_2O_3	0.51	0.49	0.53	0.46	0.45	0.49	0.44	0.37	0.49	0.43	0.47	0.43	0.45	0.46	0.43	0.56	0.47
MgO	0.27	0.28	0.19	0.14	0.22	0.18	0.19	0.17	0.23	0.23	0.22	0.18	0.22	0.25	0.26	0.20	0.21
CaO	14.66	15.96	17.34	17.35	17.51	17.82	17.18	17.20	17.13	17.20	15.67	18.24	17.88	16.98	16.85	17.39	17.57
SrO	0.00	0.00	0.03	0.01	0.00	0.00	0.00	0.10	0.00	0.00	0.00	0.00	0.00	0.00	0.02	0.00	0.00
BaO	0.14	0.01	0.00	0.00	0.18	0.03	0.00	0.07	0.15	0.00	0.00	0.10	0.00	0.03	0.12	0.02	0.00
Na_2O	3.52	2.71	1.48	1.52	2.37	2.10	1.65	1.44	1.89	1.45	2.61	1.40	1.29	2.16	1.91	1.89	2.01
K_2O	0.06	0.02	0.04	0.00	0.03	0.03	0.02	0.00	0.02	0.04	0.00	0.01	0.01	0.02	0.06	0.07	0.00
Total	99.74	99.42	98.99	99.24	100.82	100.54	98.96	98.72	99.78	98.48	98.69	99.55	98.79	100.09	98.88	98.81	99.97
Si	2.31	2.25	2.14	2.14	2.19	2.18	2.14	2.14	2.17	2.15	2.24	2.13	2.13	2.19	2.18	2.17	2.17
Ti	0.00	0.00	0.00	0.00	0.00	0.00	0.00	0.00	0.01	0.00	0.01	0.00	0.00	0.00	0.00	0.01	0.00
Fe3+	0.02	0.02	0.02	0.02	0.02	0.02	0.02	0.01	0.02	0.02	0.02	0.02	0.02	0.02	0.02	0.02	0.02
Mg	0.02	0.02	0.01	0.01	0.02	0.01	0.01	0.01	0.02	0.02	0.02	0.01	0.02	0.02	0.02	0.01	0.01
Ca	0.72	0.79	0.87	0.86	0.86	0.88	0.86	0.86	0.85	0.86	0.78	0.91	0.89	0.84	0.84	0.87	0.87
Sr	0.00	0.00	0.00	0.00	0.00	0.00	0.00	0.00	0.00	0.00	0.00	0.00	0.00	0.00	0.00	0.00	0.00
Ba	0.00	0.00	0.00	0.00	0.00	0.00	0.00	0.00	0.00	0.00	0.00	0.00	0.00	0.00	0.00	0.00	0.00
Na	0.31	0.24	0.13	0.14	0.21	0.19	0.15	0.13	0.17	0.13	0.24	0.13	0.12	0.19	0.17	0.17	0.18
K	0.00	0.00	0.00	0.00	0.00	0.00	0.00	0.00	0.00	0.00	0.00	0.00	0.00	0.00	0.00	0.00	0.00
Sum (cat)	5.02	5.02	5.00	5.00	5.04	5.03	5.01	5.00	5.01	5.00	5.01	5.02	5.00	5.02	5.01	5.02	5.02
Ab	30.09	23.49	13.30	13.69	19.57	17.57	14.80	13.14	16.59	13.24	23.19	12.17	11.52	18.68	16.89	16.34	17.13
An	69.32	76.39	86.36	86.28	80.00	82.23	85.10	86.47	83.02	86.54	76.81	87.62	88.44	81.18	82.47	83.23	82.87
Or	0.34	0.11	0.26	0.00	0.14	0.15	0.10	0.00	0.11	0.23	0.00	0.04	0.05	0.09	0.37	0.40	0.00

* Measurement used in core to rim comparisons

APPENDIX A. Continues…

Grain	PL-1						PL-3										PL-17			
Spot	plg332	plg333	plg336	plg337	plg334	plg338	plg342	plg341	plg343	plg344	plg349	plg345	plg346	plg351	plg347	plg353	plg424	plg425	plg426	plg427
Location	Core	Mid	Mid		Rim	Rim*	Core*							Rim	Rim	Rim*	Core*		Mid	Rim*
SiO_2	46.22	45.96	44.93	48.52	48.52	48.54	46.61	46.29	48.11	46.03	49.20	45.39	44.67	45.06	46.96	47.41	46.41	47.61	45.58	49.38
TiO_2	0.00	0.11	0.05	0.00	0.08	0.05	0.03	0.11	0.06	0.00	0.18	0.03	0.00	0.00	0.05	0.02	0.00	0.08	0.00	0.00
Al_2O_3	33.09	33.05	33.10	31.96	30.72	30.51	31.36	31.72	32.51	31.83	30.45	33.38	32.99	33.18	31.46	29.99	32.75	31.41	33.39	30.67
Fe_2O_3	0.50	0.36	0.45	0.69	0.75	0.75	0.54	0.58	0.47	0.45	0.39	0.41	0.40	0.39	0.59	0.67	0.43	0.55	0.37	0.66
MgO	0.47	0.20	0.23	0.40	0.19	0.22	0.30	0.23	0.28	0.29	0.33	0.15	0.21	0.23	0.23	0.21	0.23	0.29	0.22	0.26
CaO	16.09	17.83	18.49	16.68	15.51	15.65	16.35	16.35	16.09	16.81	15.58	19.31	18.15	18.37	16.30	14.99	18.48	17.12	19.91	14.64
SrO	0.00	0.00	0.00	0.00	0.01	0.00	0.00	0.00	0.01	0.00	0.00	0.00	0.04	0.00	0.01	0.00	0.00	0.00	0.00	0.00
BaO	0.10	0.07	0.00	0.09	0.05	0.00	0.02	0.00	0.27	0.09	0.03	0.03	0.00	0.24	0.00	0.01	0.00	0.00	0.00	0.00
Na_2O	1.24	1.40	1.21	2.24	2.72	2.78	2.16	1.98	2.23	1.93	2.96	1.27	1.22	1.30	2.28	2.82	1.68	2.47	1.37	2.91
K_2O	0.43	0.01	0.04	0.03	0.08	0.07	0.03	0.05	0.03	0.03	0.09	0.05	0.01	0.02	0.02	0.03	0.01	0.01	0.00	0.04
Total	98.13	98.98	98.49	100.61	98.63	98.56	97.40	97.32	100.07	97.46	99.21	100.02	97.69	98.79	97.90	96.15	100.00	99.54	100.84	98.56
Si	2.16	2.14	2.11	2.22	2.26	2.26	2.20	2.19	2.21	2.18	2.27	2.11	2.11	2.11	2.21	2.26	2.15	2.21	2.10	2.29
Ti	0.00	0.00	0.00	0.00	0.00	0.00	0.00	0.00	0.00	0.00	0.01	0.00	0.00	0.00	0.00	0.00	0.00	0.00	0.00	0.00
Fe3+	0.02	0.01	0.02	0.02	0.03	0.03	0.02	0.02	0.02	0.02	0.01	0.01	0.01	0.01	0.02	0.02	0.02	0.02	0.01	0.02
Mg	0.03	0.01	0.02	0.03	0.01	0.02	0.02	0.02	0.02	0.02	0.02	0.01	0.02	0.02	0.02	0.02	0.02	0.02	0.02	0.02
Ca	0.81	0.89	0.93	0.82	0.77	0.78	0.83	0.83	0.79	0.85	0.77	0.96	0.92	0.92	0.82	0.77	0.92	0.85	0.98	0.73
Sr	0.00	0.00	0.00	0.00	0.00	0.00	0.00	0.00	0.00	0.00	0.00	0.00	0.00	0.00	0.00	0.00	0.00	0.00	0.00	0.00
Ba	0.00	0.00	0.00	0.00	0.00	0.00	0.00	0.00	0.01	0.00	0.00	0.00	0.00	0.00	0.00	0.00	0.00	0.00	0.00	0.00
Na	0.11	0.13	0.11	0.20	0.25	0.25	0.20	0.18	0.20	0.18	0.27	0.11	0.11	0.12	0.21	0.26	0.15	0.22	0.12	0.26
K	0.03	0.00	0.00	0.00	0.01	0.00	0.00	0.00	0.00	0.00	0.01	0.00	0.00	0.00	0.00	0.00	0.00	0.00	0.00	0.00
Sum (cat)	4.99	5.00	5.02	5.01	5.01	5.02	5.02	5.01	5.00	5.02	5.02	5.03	5.02	5.02	5.02	5.02	5.03	5.04	5.05	5.00
Ab	11.86	12.39	10.61	19.46	23.98	24.22	19.24	17.91	19.95	17.11	25.47	10.60	10.80	11.25	20.18	25.38	14.13	20.67	11.08	26.38
An	85.27	87.42	89.18	80.20	75.45	75.40	80.55	81.77	79.39	82.56	73.96	89.09	89.00	88.21	79.68	74.43	85.84	79.26	88.92	73.35
Or	2.68	0.07	0.21	0.18	0.46	0.37	0.18	0.33	0.16	0.18	0.51	0.26	0.09	0.11	0.13	0.16	0.03	0.07	0.00	0.27

* Measurement used in core to rim comparisons

APPENDIX A. Continues…

Grain	PL-6						PL-10					PL-11									
Spot	plg372	plg374	plg375	plg376	plg377	plg379	plg382	plg383	plg384	plg385	plg386	plg388	plg389	plg390	plg391	plg392	plg393	plg394	plg395	plg397	plg398
Location	Inc.	Core	Mid	Core	Mid	Rim*	Core*	Mid		Rim	Rim*	Core*	Core	Core	Mid	Mid	Mid		Rim	Rim	Rim*
SiO_2	49.11	45.16	45.15	46.75	45.02	45.16	44.58	45.17	45.40	45.18	44.05	46.01	46.22	48.28	46.22	46.75	47.15	45.86	45.97	45.74	51.93
TiO_2	0.05	0.14	0.00	0.00	0.11	0.06	0.00	0.05	0.00	0.03	0.00	0.08	0.00	0.02	0.16	0.00	0.08	0.02	0.00	0.00	0.00
Al_2O_3	30.51	30.54	33.31	31.75	33.27	33.05	33.00	32.65	32.75	33.15	32.98	32.04	32.51	32.65	32.60	32.35	31.74	33.11	32.32	32.54	28.18
Fe_2O_3	1.00	0.55	0.44	0.49	0.49	0.63	0.41	0.53	0.48	0.45	0.47	0.38	0.49	0.51	0.45	0.53	0.48	0.37	0.44	0.40	0.91
MgO	0.15	0.34	0.19	0.27	0.18	0.10	0.17	0.20	0.19	0.22	0.19	0.21	0.20	0.30	0.25	0.20	0.26	0.18	0.29	0.21	0.07
CaO	15.57	16.65	19.04	17.01	18.27	18.98	18.19	17.99	18.38	18.51	18.56	18.01	17.90	17.42	17.37	17.78	16.63	18.32	17.48	17.66	12.51
SrO	0.00	0.02	0.04	0.11	0.00	0.00	0.00	0.00	0.00	0.00	0.00	0.00	0.00	0.00	0.00	0.00	0.00	0.00	0.00	0.00	0.00
BaO	0.00	0.15	0.16	0.14	0.00	0.06	0.00	0.00	0.00	0.22	0.28	0.19	0.00	0.00	0.00	0.08	0.08	0.01	0.23	0.00	0.13
Na_2O	3.20	2.18	1.19	1.97	1.25	1.26	1.15	1.52	1.64	1.41	1.26	1.77	1.80	2.00	1.76	1.91	2.18	1.54	1.67	1.73	4.59
K_2O	0.10	0.00	0.04	0.09	0.00	0.04	0.05	0.04	0.04	0.01	0.00	0.02	0.06	0.06	0.03	0.01	0.04	0.00	0.06	0.04	0.17
Total	99.70	95.73	99.56	98.58	98.59	99.34	97.55	98.15	98.88	99.18	97.79	98.71	99.18	101.25	98.85	99.60	98.63	99.41	98.47	98.31	98.49
Si	2.27	2.18	2.10	2.19	2.11	2.11	2.11	2.13	2.13	2.11	2.09	2.16	2.15	2.20	2.16	2.17	2.20	2.13	2.16	2.15	2.40
Ti	0.00	0.01	0.00	0.00	0.00	0.00	0.00	0.00	0.00	0.00	0.00	0.00	0.00	0.00	0.01	0.00	0.00	0.00	0.00	0.00	0.00
Fe3+	0.04	0.02	0.02	0.02	0.02	0.02	0.02	0.02	0.02	0.02	0.02	0.01	0.02	0.02	0.02	0.02	0.02	0.01	0.02	0.01	0.03
Mg	0.01	0.02	0.01	0.02	0.01	0.01	0.01	0.01	0.01	0.02	0.01	0.02	0.01	0.02	0.02	0.01	0.02	0.01	0.02	0.01	0.01
Ca	0.77	0.86	0.95	0.85	0.92	0.95	0.92	0.91	0.92	0.93	0.95	0.91	0.89	0.85	0.87	0.88	0.83	0.91	0.88	0.89	0.62
Sr	0.00	0.00	0.00	0.00	0.00	0.00	0.00	0.00	0.00	0.00	0.00	0.00	0.00	0.00	0.00	0.00	0.00	0.00	0.00	0.00	0.00
Ba	0.00	0.00	0.00	0.00	0.00	0.00	0.00	0.00	0.00	0.00	0.01	0.00	0.00	0.00	0.00	0.00	0.00	0.00	0.00	0.00	0.00
Na	0.29	0.21	0.11	0.18	0.11	0.11	0.11	0.14	0.15	0.13	0.12	0.16	0.16	0.18	0.16	0.17	0.20	0.14	0.15	0.16	0.41
K	0.01	0.00	0.00	0.01	0.00	0.00	0.00	0.00	0.00	0.00	0.00	0.00	0.00	0.00	0.00	0.00	0.00	0.00	0.00	0.00	0.01
Sum (cat)	5.03	5.04	5.03	5.02	5.01	5.03	5.01	5.03	5.04	5.03	5.04	5.03	5.03	5.01	5.02	5.03	5.02	5.02	5.02	5.03	5.02
Ab	26.97	19.13	10.08	17.18	11.00	10.71	10.23	13.27	13.86	12.08	10.89	15.04	15.34	17.15	15.45	16.24	19.08	13.22	14.63	15.06	39.43
An	72.47	80.55	89.33	81.79	89.00	88.98	89.50	86.52	85.93	87.50	88.61	84.51	84.30	82.50	84.37	83.54	80.58	86.76	84.60	84.73	59.36
Or	0.57	0.00	0.23	0.51	0.00	0.20	0.27	0.22	0.21	0.04	0.02	0.13	0.36	0.36	0.18	0.08	0.21	0.00	0.37	0.21	0.99

* Measurement used in core to rim comparisons

APPENDIX A. Continues…

Grain	PL-13					PL-14					PL-15					PL-16		PL-22	
Spot	plg403	plg404	plg405	plg406	plg407	plg408	plg409	plg410	plg413	plg412	plg414	plg415	plg416	plg417	plg418	plg419	plg420	plg429	plg430
Location	Core*	Mid	Mid	Rim	Rim*	Core*	Core	Mid	Mid	Rim*	Core*	Mid	Mid	Rim	Rim*	Core*	Mid	Core*	Mid
SiO_2	45.75	45.66	44.57	46.91	50.81	46.98	44.69	46.76	44.57	50.13	44.89	46.55	45.65	46.68	51.02	46.52	45.12	46.13	44.49
TiO_2	0.10	0.00	0.14	0.05	0.06	0.00	0.06	0.00	0.00	0.00	0.00	0.00	0.00	0.10	0.14	0.00	0.14	0.00	0.03
Al_2O_3	33.04	32.35	33.43	31.37	29.40	31.76	33.05	31.88	32.78	29.00	33.29	33.89	33.17	31.39	28.44	30.96	33.37	32.66	32.98
Fe_2O_3	0.39	0.37	0.41	0.56	0.67	0.43	0.33	0.44	0.37	0.83	0.34	0.38	0.37	0.39	0.71	1.00	0.48	0.46	0.43
MgO	0.18	0.24	0.18	0.23	0.18	0.25	0.21	0.31	0.18	0.18	0.15	0.20	0.19	0.31	0.19	0.77	0.21	0.17	0.19
CaO	18.48	18.38	18.80	16.80	14.26	17.07	18.55	17.41	18.42	14.02	18.49	19.40	19.40	17.10	13.72	17.51	19.41	17.66	18.24
SrO	0.00	0.00	0.00	0.00	0.00	0.00	0.00	0.00	0.00	0.00	0.00	0.00	0.10	0.00	0.00	0.00	0.00	0.00	0.00
BaO	0.03	0.16	0.00	0.12	0.00	0.00	0.00	0.00	0.25	0.00	0.20	0.09	0.00	0.00	0.02	0.02	0.11	0.07	0.15
Na_2O	1.35	1.49	1.19	2.11	3.84	2.03	1.30	2.01	1.31	3.77	1.28	1.20	1.29	2.17	4.45	2.00	1.17	1.56	1.17
K_2O	0.01	0.02	0.03	0.09	0.07	0.05	0.02	0.02	0.01	0.10	0.03	0.05	0.04	0.07	0.08	0.06	0.00	0.01	0.02
Total	99.34	98.68	98.75	98.24	99.29	98.56	98.22	98.83	97.90	98.03	98.67	101.76	100.21	98.20	98.77	98.84	100.02	98.72	97.70
Si	2.13	2.14	2.09	2.20	2.34	2.20	2.11	2.18	2.11	2.34	2.11	2.12	2.11	2.19	2.36	2.18	2.10	2.16	2.11
Ti	0.00	0.00	0.01	0.00	0.00	0.00	0.00	0.00	0.00	0.00	0.00	0.00	0.00	0.00	0.01	0.00	0.01	0.00	0.00
Fe3+	0.01	0.01	0.01	0.02	0.02	0.02	0.01	0.02	0.01	0.03	0.01	0.01	0.01	0.01	0.03	0.04	0.02	0.02	0.02
Mg	0.01	0.02	0.01	0.02	0.01	0.02	0.01	0.02	0.01	0.01	0.01	0.01	0.01	0.02	0.01	0.05	0.02	0.01	0.01
Ca	0.92	0.92	0.95	0.85	0.70	0.85	0.94	0.87	0.94	0.70	0.93	0.95	0.96	0.86	0.68	0.88	0.97	0.88	0.93
Sr	0.00	0.00	0.00	0.00	0.00	0.00	0.00	0.00	0.00	0.00	0.00	0.00	0.00	0.00	0.00	0.00	0.00	0.00	0.00
Ba	0.00	0.00	0.00	0.00	0.00	0.00	0.00	0.00	0.01	0.00	0.00	0.00	0.00	0.00	0.00	0.00	0.00	0.00	0.00
Na	0.12	0.14	0.11	0.19	0.34	0.18	0.12	0.18	0.12	0.34	0.12	0.11	0.12	0.20	0.40	0.18	0.11	0.14	0.11
K	0.00	0.00	0.00	0.01	0.00	0.00	0.00	0.00	0.00	0.01	0.00	0.00	0.00	0.00	0.01	0.00	0.00	0.00	0.00
Sum (cat)	5.02	5.03	5.03	5.02	5.02	5.02	5.03	5.03	5.03	5.02	5.02	5.02	5.03	5.03	5.05	5.04	5.03	5.01	5.02
Ab	11.70	12.77	10.23	18.39	32.65	17.64	11.25	17.28	11.37	32.55	11.05	10.00	10.66	18.59	36.81	17.10	9.82	13.77	10.38
An	88.17	86.86	89.62	80.90	66.95	82.09	88.61	82.62	88.13	66.86	88.45	89.60	88.88	81.02	62.71	82.52	89.99	86.05	89.23
Or	0.08	0.11	0.16	0.50	0.39	0.27	0.14	0.09	0.06	0.59	0.15	0.25	0.20	0.40	0.45	0.34	0.00	0.06	0.12

* Measurement used in core to rim comparisons

APPENDIX A. Continues…

Grain	PL-23										GM2	GM4	GM5	GM7	GM8	Inc.	GM2		GM1
Spot	plg358	plg359	plg366	plg360	plg367	plg361	plg368	plg369	plg362	plg370	plg340	plg355	plg356	plg381	plg401	plg371	plg78	plg79	plg73
Location	Core*			Mid	Mid	Rim	Rim	Rim	Rim	Rim*									
SiO_2	44.75	44.59	44.88	45.20	45.81	45.06	48.02	49.94	48.60	50.66	49.57	46.82	48.77	47.90	46.20	48.75	49.14	51.76	49.39
TiO_2	0.06	0.00	0.00	0.05	0.03	0.00	0.00	0.00	0.16	0.00	0.06	0.02	0.18	0.13	0.00	0.29	0.04	0.00	0.04
Al_2O_3	32.27	33.20	32.92	32.88	31.92	32.31	30.56	29.10	30.01	28.81	30.11	31.10	28.72	31.16	32.23	29.71	31.01	29.71	30.57
Fe_2O_3	0.93	0.35	0.41	0.37	0.39	0.39	0.85	0.90	0.75	0.83	0.93	0.83	0.80	0.63	0.42	0.68	0.64	0.90	0.66
MgO	0.55	0.18	0.18	0.17	0.20	0.23	0.52	0.10	0.25	0.13	0.12	0.29	0.20	0.47	0.22	0.18	0.21	0.16	0.19
CaO	17.55	18.82	17.73	17.91	17.00	17.82	15.20	13.90	15.09	13.65	14.30	16.33	14.10	16.76	17.26	15.13	15.51	14.20	15.35
SrO	0.00	0.00	0.00	0.00	0.00	0.00	0.00	0.00	0.00	0.07	0.00	0.00	0.00	0.00	0.00	0.00	0.02	0.00	0.00
BaO	0.15	0.00	0.00	0.00	0.00	0.01	0.00	0.00	0.00	0.03	0.00	0.00	0.00	0.00	0.05	0.00	0.00	0.00	0.10
Na_2O	1.32	1.14	1.34	1.45	1.78	1.58	2.65	3.79	2.75	3.96	3.20	2.16	3.28	2.39	1.72	3.21	3.21	4.34	3.13
K_2O	0.05	0.01	0.00	0.02	0.00	0.02	0.10	0.08	0.03	0.12	0.06	0.05	0.05	0.04	0.04	0.08	0.03	0.16	0.05
Total	97.64	98.29	97.46	98.04	97.13	97.42	97.89	97.80	97.65	98.26	98.35	97.60	96.10	99.48	98.14	98.03	99.80	101.24	99.46
Si	2.12	2.10	2.12	2.13	2.17	2.14	2.25	2.34	2.28	2.36	2.30	2.21	2.32	2.22	2.17	2.28	2.26	2.34	2.28
Ti	0.00	0.00	0.00	0.00	0.00	0.00	0.00	0.00	0.01	0.00	0.00	0.00	0.01	0.00	0.00	0.01	0.00	0.00	0.00
Fe3+	0.03	0.01	0.02	0.01	0.01	0.01	0.03	0.03	0.03	0.03	0.03	0.03	0.03	0.02	0.02	0.02	0.02	0.03	0.02
Mg	0.04	0.01	0.01	0.01	0.01	0.02	0.04	0.01	0.02	0.01	0.01	0.02	0.01	0.03	0.02	0.01	0.02	0.01	0.01
Ca	0.89	0.95	0.90	0.90	0.86	0.91	0.76	0.70	0.76	0.68	0.71	0.83	0.72	0.83	0.87	0.76	0.76	0.69	0.76
Sr	0.00	0.00	0.00	0.00	0.00	0.00	0.00	0.00	0.00	0.00	0.00	0.00	0.00	0.00	0.00	0.00	0.00	0.00	0.00
Ba	0.00	0.00	0.00	0.00	0.00	0.00	0.00	0.00	0.00	0.00	0.00	0.00	0.00	0.00	0.00	0.00	0.00	0.00	0.00
Na	0.12	0.10	0.12	0.13	0.16	0.15	0.24	0.34	0.25	0.36	0.29	0.20	0.30	0.21	0.16	0.29	0.29	0.38	0.28
K	0.00	0.00	0.00	0.00	0.00	0.00	0.01	0.01	0.00	0.01	0.00	0.00	0.00	0.00	0.00	0.01	0.00	0.01	0.00
Sum (cat)	5.02	5.02	5.01	5.02	5.01	5.03	5.01	5.02	5.00	5.02	5.00	5.01	5.01	5.03	5.01	5.02	5.03	5.05	5.02
Ab	11.94	9.90	12.01	12.74	15.90	13.81	23.83	32.87	24.76	34.10	28.70	19.28	29.56	20.45	15.25	27.63	27.20	35.32	26.81
An	87.50	90.07	87.99	87.14	84.10	86.05	75.60	66.66	75.06	64.97	70.94	80.44	70.17	79.33	84.44	71.92	72.58	63.80	72.75
Or	0.29	0.03	0.00	0.12	0.00	0.12	0.57	0.47	0.18	0.70	0.36	0.27	0.27	0.23	0.22	0.45	0.16	0.88	0.27

* Measurement used in core to rim comparisons

APPENDIX B. Microprobe analyses of plagioclase phenocrysts and groundmass plagioclase grains of sample AL-T026C.

Grain	PL-5																			
Spot	plg127	plg126	plg125	plg124	plg123	plg122	plg121	plg88	plg89	plg90	plg91	plg92	plg93	plg94	plg95	plg96	plg97	plg98	plg99	plg100
Location	Core*																			
SiO_2	45.75	46.79	46.86	46.47	46.30	46.36	45.85	45.62	45.36	45.78	46.03	45.38	45.37	46.03	46.39	45.23	47.02	45.95	45.89	46.35
TiO_2	0.00	0.00	0.00	0.00	0.00	0.10	0.00	0.00	0.00	0.00	0.00	0.11	0.00	0.12	0.05	0.09	0.00	0.00	0.01	0.00
Al_2O_3	31.53	32.72	32.81	32.98	33.15	33.17	33.27	33.23	33.10	33.27	33.30	32.65	32.65	32.73	33.25	33.07	33.84	33.07	33.15	33.53
Fe_2O_3	0.35	0.37	0.39	0.39	0.32	0.33	0.34	0.29	0.31	0.28	0.22	0.39	0.33	0.37	0.24	0.38	0.31	0.40	0.39	0.39
MgO	0.15	0.16	0.16	0.16	0.16	0.17	0.17	0.15	0.18	0.15	0.13	0.22	0.16	0.14	0.14	0.14	0.20	0.18	0.16	0.16
CaO	18.86	17.47	17.18	17.36	17.63	17.69	18.20	17.83	17.66	17.84	17.54	17.39	16.78	16.96	16.90	16.51	16.48	16.43	17.09	17.54
SrO	0.00	0.00	0.00	0.00	0.00	0.00	0.00	0.09	0.00	0.00	0.00	0.00	0.01	0.00	0.00	0.06	0.00	0.00	0.00	0.00
BaO	0.00	0.00	0.09	0.15	0.02	0.00	0.00	0.00	0.00	0.01	0.00	0.00	0.04	0.01	0.03	0.08	0.00	0.00	0.08	0.00
Na_2O	2.07	2.11	2.16	1.95	1.87	1.87	1.74	1.74	1.59	1.80	1.65	1.80	1.83	1.79	1.72	1.69	1.86	1.82	1.66	1.73
K_2O	0.06	0.00	0.04	0.03	0.03	0.03	0.02	0.04	0.07	0.05	0.01	0.02	0.07	0.06	0.08	0.01	0.00	0.03	0.04	0.01
Total	98.76	99.61	99.68	99.47	99.48	99.71	99.59	98.99	98.27	99.17	98.88	97.98	97.22	98.20	98.78	97.25	99.70	97.89	98.46	99.71
Si	2.15	2.17	2.17	2.16	2.15	2.15	2.13	2.13	2.13	2.13	2.14	2.14	2.15	2.16	2.16	2.14	2.16	2.16	2.15	2.14
Ti	0.00	0.00	0.00	0.00	0.00	0.00	0.00	0.00	0.00	0.00	0.00	0.00	0.00	0.00	0.00	0.00	0.00	0.00	0.00	0.00
Fe3+	0.01	0.01	0.01	0.01	0.01	0.01	0.01	0.01	0.01	0.01	0.01	0.01	0.01	0.01	0.01	0.01	0.01	0.01	0.01	0.01
Mg	0.01	0.01	0.01	0.01	0.01	0.01	0.01	0.01	0.01	0.01	0.01	0.02	0.01	0.01	0.01	0.01	0.01	0.01	0.01	0.01
Ca	0.95	0.87	0.85	0.86	0.88	0.88	0.91	0.89	0.89	0.89	0.88	0.88	0.85	0.85	0.84	0.84	0.81	0.83	0.86	0.87
Sr	0.00	0.00	0.00	0.00	0.00	0.00	0.00	0.00	0.00	0.00	0.00	0.00	0.00	0.00	0.00	0.00	0.00	0.00	0.00	0.00
Ba	0.00	0.00	0.00	0.00	0.00	0.00	0.00	0.00	0.00	0.00	0.00	0.00	0.00	0.00	0.00	0.00	0.00	0.00	0.00	0.00
Na	0.19	0.19	0.19	0.18	0.17	0.17	0.16	0.16	0.15	0.16	0.15	0.16	0.17	0.16	0.16	0.16	0.17	0.17	0.15	0.16
K	0.00	0.00	0.00	0.00	0.00	0.00	0.00	0.00	0.00	0.00	0.00	0.00	0.00	0.00	0.01	0.00	0.00	0.00	0.00	0.00
Sum (cat)	5.07	5.03	5.03	5.03	5.03	5.03	5.04	5.03	5.02	5.03	5.01	5.03	5.02	5.01	5.00	5.01	5.00	5.01	5.01	5.02
Ab	16.50	17.94	18.49	16.80	16.05	16.01	14.71	14.93	13.99	15.38	14.55	15.74	16.37	15.96	15.44	15.55	16.95	16.65	14.87	15.13
An	83.18	82.06	81.16	82.77	83.75	83.84	85.17	84.63	85.62	84.35	85.38	84.13	83.15	83.67	84.06	84.09	83.06	83.15	84.76	84.82
Or	0.32	0.00	0.20	0.18	0.16	0.15	0.12	0.21	0.39	0.26	0.06	0.14	0.39	0.36	0.45	0.04	0.00	0.20	0.23	0.05

* Measurement used in core to rim comparisons

APPENDIX B. Continues…

Grain	PL-5																		
Spot	plg101	plg102	plg103	plg104	plg105	plg106	plg107	plg108	plg109	plg110	plg111	plg112	plg113	plg114	plg115	plg116	plg117	plg118	plg119
Location		Mid															Rim		Rim*
SiO_2	46.21	46.23	45.70	45.17	46.02	46.51	46.71	45.88	46.30	45.78	45.28	45.28	45.19	46.07	47.21	47.37	46.97	46.47	44.58
TiO_2	0.00	0.00	0.00	0.00	0.04	0.01	0.00	0.03	0.00	0.02	0.04	0.00	0.00	0.09	0.00	0.00	0.00	0.00	0.02
Al_2O_3	33.31	33.32	33.21	32.65	33.11	33.38	33.27	32.79	32.85	31.27	33.39	33.84	33.67	33.72	31.76	32.27	32.23	32.57	33.39
Fe_2O_3	0.36	0.28	0.34	0.32	0.26	0.35	0.37	0.39	0.39	0.45	0.45	0.35	0.44	0.45	0.45	0.46	0.33	0.47	0.48
MgO	0.15	0.14	0.12	0.21	0.15	0.14	0.16	0.17	0.17	0.44	0.17	0.20	0.20	0.16	0.29	0.38	0.28	0.25	0.27
CaO	17.26	17.30	16.68	17.03	16.91	17.20	17.63	16.88	17.23	17.58	18.27	18.33	20.12	18.61	16.07	16.89	17.76	18.06	19.64
SrO	0.00	0.00	0.00	0.00	0.02	0.00	0.00	0.00	0.02	0.02	0.00	0.00	0.00	0.00	0.00	0.00	0.01	0.00	0.00
BaO	0.00	0.00	0.04	0.04	0.03	0.00	0.05	0.09	0.00	0.02	0.00	0.14	0.03	0.07	0.09	0.00	0.03	0.20	0.00
Na_2O	1.84	1.77	1.74	1.87	1.72	1.78	1.78	1.96	2.01	2.14	1.32	1.39	1.41	1.45	2.47	2.30	2.43	2.16	1.38
K_2O	0.00	0.04	0.04	0.05	0.01	0.02	0.00	0.05	0.05	0.02	0.01	0.02	0.01	0.03	0.02	0.04	0.04	0.03	0.00
Total	99.13	99.08	97.87	97.33	98.27	99.40	99.96	98.23	99.03	97.75	98.93	99.55	101.08	100.64	98.37	99.70	100.08	100.21	99.76
Si	2.15	2.15	2.15	2.14	2.15	2.15	2.15	2.15	2.16	2.17	2.12	2.10	2.08	2.12	2.21	2.19	2.17	2.15	2.08
Ti	0.00	0.00	0.00	0.00	0.00	0.00	0.00	0.00	0.00	0.00	0.00	0.00	0.00	0.00	0.00	0.00	0.00	0.00	0.00
Fe3+	0.01	0.01	0.01	0.01	0.01	0.01	0.01	0.01	0.01	0.02	0.02	0.01	0.02	0.02	0.02	0.02	0.01	0.02	0.02
Mg	0.01	0.01	0.01	0.02	0.01	0.01	0.01	0.01	0.01	0.03	0.01	0.01	0.01	0.01	0.02	0.03	0.02	0.02	0.02
Ca	0.86	0.86	0.84	0.87	0.85	0.85	0.87	0.85	0.86	0.89	0.91	0.91	0.99	0.92	0.80	0.84	0.88	0.90	0.98
Sr	0.00	0.00	0.00	0.00	0.00	0.00	0.00	0.00	0.00	0.00	0.00	0.00	0.00	0.00	0.00	0.00	0.00	0.00	0.00
Ba	0.00	0.00	0.00	0.00	0.00	0.00	0.00	0.00	0.00	0.00	0.00	0.00	0.00	0.00	0.00	0.00	0.00	0.00	0.00
Na	0.17	0.16	0.16	0.17	0.16	0.16	0.16	0.18	0.18	0.20	0.12	0.13	0.13	0.13	0.22	0.21	0.22	0.19	0.13
K	0.00	0.00	0.00	0.00	0.00	0.00	0.00	0.00	0.00	0.00	0.00	0.00	0.00	0.00	0.00	0.00	0.00	0.00	0.00
Sum (cat)	5.02	5.02	5.01	5.03	5.01	5.01	5.02	5.02	5.03	5.05	5.02	5.03	5.06	5.02	5.02	5.03	5.06	5.05	5.06
Ab	16.17	15.56	15.81	16.49	15.53	15.73	15.44	17.26	17.37	18.03	11.52	12.04	11.21	12.35	21.69	19.73	19.78	17.72	11.30
An	83.83	84.21	83.88	83.14	84.32	84.15	84.48	82.29	82.30	81.77	88.41	87.59	88.69	87.37	78.03	80.06	79.93	81.80	88.69
Or	0.00	0.23	0.24	0.31	0.05	0.12	0.00	0.28	0.30	0.11	0.07	0.13	0.05	0.16	0.12	0.22	0.22	0.15	0.01

* Measurement used in core to rim comparisons

APPENDIX B. Continues…

Grain	PL-1			PL-2			PL-6			PL-8					PL-9		
Spot	plg80	plg81	plg82	plg84	plg85	plg86	plg128	plg129	plg130	plg132	plg133	plg134	plg136	plg137	plg138	plg139	plg140
Location	Core*	Mid	Mid	Core*	Core	Mid	Core*	Rim	Rim*	Core*	Mid	Mid		Rim*	Core*	Mid	Rim*
SiO_2	44.97	44.99	45.73	45.64	46.34	47.59	45.37	45.76	47.79	45.88	46.11	45.80	51.72	48.01	46.10	45.21	45.22
TiO_2	0.00	0.00	0.06	0.00	0.00	0.00	0.02	0.06	0.00	0.00	0.00	0.00	0.00	0.08	0.14	0.10	0.00
Al_2O_3	33.07	33.44	32.45	32.77	32.82	31.96	33.18	33.22	31.95	33.22	32.79	33.21	29.37	31.62	32.58	33.14	33.26
Fe_2O_3	0.40	0.39	0.49	0.48	0.43	0.50	0.47	0.52	0.69	0.43	0.46	0.51	1.01	1.02	0.44	0.56	0.48
MgO	0.21	0.18	0.25	0.19	0.22	0.29	0.10	0.16	0.14	0.20	0.21	0.20	0.13	0.17	0.25	0.20	0.25
CaO	18.19	18.31	17.07	17.43	17.25	16.34	17.60	17.52	16.10	18.02	17.77	17.82	13.58	15.97	17.84	17.97	17.88
SrO	0.00	0.02	0.00	0.00	0.00	0.00	0.00	0.00	0.01	0.00	0.00	0.00	0.00	0.00	0.00	0.00	0.00
BaO	0.00	0.11	0.02	0.02	0.10	0.00	0.00	0.02	0.05	0.04	0.00	0.01	0.00	0.00	0.00	0.00	0.00
Na_2O	1.46	1.37	1.84	1.89	1.93	2.52	1.63	1.58	2.44	1.62	1.70	1.54	4.35	2.75	1.80	1.41	1.45
K_2O	0.05	0.05	0.05	0.03	0.00	0.04	0.01	0.03	0.04	0.03	0.04	0.02	0.11	0.08	0.02	0.02	0.03
Total	98.36	98.85	97.94	98.45	99.10	99.25	98.37	98.87	99.23	99.42	99.07	99.11	100.26	99.69	99.18	98.62	98.56
Si	2.12	2.11	2.15	2.14	2.16	2.21	2.13	2.14	2.21	2.13	2.15	2.13	2.36	2.22	2.15	2.12	2.12
Ti	0.00	0.00	0.00	0.00	0.00	0.00	0.00	0.00	0.00	0.00	0.00	0.00	0.00	0.00	0.01	0.00	0.00
Fe3+	0.01	0.01	0.02	0.02	0.02	0.02	0.02	0.02	0.02	0.02	0.02	0.02	0.04	0.04	0.02	0.02	0.02
Mg	0.01	0.01	0.02	0.01	0.02	0.02	0.01	0.01	0.01	0.01	0.02	0.01	0.01	0.01	0.02	0.01	0.02
Ca	0.92	0.92	0.86	0.88	0.86	0.81	0.89	0.88	0.80	0.90	0.89	0.89	0.66	0.79	0.89	0.90	0.90
Sr	0.00	0.00	0.00	0.00	0.00	0.00	0.00	0.00	0.00	0.00	0.00	0.00	0.00	0.00	0.00	0.00	0.00
Ba	0.00	0.00	0.00	0.00	0.00	0.00	0.00	0.00	0.00	0.00	0.00	0.00	0.00	0.00	0.00	0.00	0.00
Na	0.13	0.12	0.17	0.17	0.17	0.23	0.15	0.14	0.22	0.15	0.15	0.14	0.38	0.25	0.16	0.13	0.13
K	0.00	0.00	0.00	0.00	0.00	0.00	0.00	0.00	0.00	0.00	0.00	0.00	0.01	0.01	0.00	0.00	0.00
Sum (cat)	5.03	5.03	5.02	5.03	5.02	5.03	5.02	5.01	5.01	5.03	5.02	5.02	5.03	5.03	5.03	5.02	5.02
Ab	12.66	11.85	16.28	16.36	16.83	21.76	14.36	14.03	21.47	13.94	14.70	13.50	36.47	23.62	15.45	12.44	12.75
An	87.03	87.65	83.39	83.45	83.00	77.99	85.59	85.74	78.17	85.81	85.05	86.36	62.95	75.91	84.42	87.43	87.09
Or	0.31	0.27	0.30	0.16	0.00	0.25	0.05	0.20	0.23	0.19	0.25	0.13	0.58	0.48	0.13	0.13	0.16

* Measurement used in core to rim comparisons

APPENDIX B. Continues…

Grain		PL-10		PL-23a	PL-23b		PL-23c		PL-24		GM1
Spot	plg155	plg156	plg157	plg146	plg147	plg148	plg149	plg150	plg143	plg144	plg141
Location	Mid	Mid	Rim*	Core*	Core*	Core*	Mid/Rim	Rim*	Core*	Mid	
SiO_2	46.69	46.51	48.22	45.40	45.55	46.45	46.72	46.20	46.18	46.25	47.05
TiO_2	0.00	0.00	0.05	0.10	0.00	0.00	0.00	0.00	0.00	0.00	0.00
Al_2O_3	32.71	32.76	31.56	33.52	33.58	32.77	32.53	32.85	33.02	33.23	31.22
Fe_2O_3	0.53	0.49	0.80	0.50	0.46	0.41	0.51	0.51	0.56	0.48	1.17
MgO	0.27	0.21	0.56	0.19	0.21	0.21	0.24	0.18	0.16	0.22	0.39
CaO	17.00	17.49	16.22	17.77	18.85	17.43	17.58	17.11	17.89	17.72	16.03
SrO	0.00	0.00	0.00	0.00	0.00	0.00	0.00	0.03	0.01	0.07	0.03
BaO	0.06	0.00	0.00	0.00	0.00	0.01	0.03	0.00	0.00	0.04	0.06
Na2O	1.85	1.81	2.46	1.46	1.41	1.78	2.08	1.94	1.79	1.70	2.46
K_2O	0.02	0.00	0.02	0.02	0.00	0.00	0.03	0.00	0.04	0.03	0.05
Total	99.11	99.26	99.89	98.95	100.06	99.06	99.71	98.83	99.66	99.74	98.46
Si	2.17	2.16	2.22	2.12	2.11	2.16	2.16	2.15	2.14	2.14	2.20
Ti	0.00	0.00	0.00	0.00	0.00	0.00	0.00	0.00	0.00	0.00	0.00
Fe3+	0.02	0.02	0.03	0.02	0.02	0.01	0.02	0.02	0.02	0.02	0.04
Mg	0.02	0.02	0.04	0.01	0.01	0.01	0.02	0.01	0.01	0.02	0.03
Ca	0.85	0.87	0.80	0.89	0.94	0.87	0.87	0.86	0.89	0.88	0.80
Sr	0.00	0.00	0.00	0.00	0.00	0.00	0.00	0.00	0.00	0.00	0.00
Ba	0.00	0.00	0.00	0.00	0.00	0.00	0.00	0.00	0.00	0.00	0.00
Na	0.17	0.16	0.22	0.13	0.13	0.16	0.19	0.18	0.16	0.15	0.22
K	0.00	0.00	0.00	0.00	0.00	0.00	0.00	0.00	0.00	0.00	0.00
Sum (cat)	5.01	5.02	5.02	5.02	5.03	5.02	5.03	5.02	5.03	5.02	5.03
Ab	16.40	15.74	21.48	12.90	11.92	15.62	17.56	17.00	15.32	14.75	21.65
An	83.38	84.24	78.39	86.97	88.08	84.36	82.20	82.88	84.42	84.84	77.87
Or	0.13	0.02	0.13	0.14	0.00	0.00	0.19	0.03	0.24	0.15	0.32

* Measurement used in core to rim comparisons

APPENDIX C. Microprobe analyses of plagioclase phenocrysts and groundmass plagioclase grains of sample AL-T026D.

Grain	PL-3	PL-4a-1			PL-4b-1		PL-5-1			PL-1-1		PL-2-1		PL-12-1		PL-11-1
Spot	plg34	plg35	plg36	plg37	plg38	plg39	plg41	plg42	plg43	plg44	plg45	plg47	plg48	plg49	plg50	plg52
Location	Core*	Mid	Mid	Rim*	Core*	Rim*	Core*	Rim*	Core*	Rim	Rim*	Core*	Core*	Mid	Rim*	Mid
SiO_2	45.79	45.01	45.99	47.79	45.96	47.77	45.96	48.24	46.00	45.91	53.31	45.89	45.43	47.77	48.36	46.48
TiO_2	0.00	0.00	0.06	0.00	0.00	0.18	0.08	0.00	0.00	0.00	0.04	0.01	0.04	0.17	0.03	0.00
Al_2O_3	33.45	32.74	33.31	31.89	32.92	31.44	32.91	31.29	32.34	32.88	28.21	32.97	32.68	31.43	30.95	32.85
Fe_2O_3	0.46	0.43	0.37	0.52	0.38	0.64	0.49	0.47	0.45	0.42	0.97	0.46	0.53	0.60	0.60	0.52
MgO	0.22	0.18	0.19	0.28	0.17	0.31	0.21	0.31	0.21	0.21	0.18	0.19	0.10	0.17	0.26	0.24
CaO	18.90	17.74	17.31	16.42	18.11	16.70	18.50	16.70	17.50	18.56	12.76	17.40	17.62	16.19	15.59	17.54
SrO	0.00	0.01	0.00	0.00	0.00	0.00	0.00	0.00	0.00	0.00	0.00	0.00	0.00	0.00	0.00	0.00
BaO	0.00	0.16	0.10	0.00	0.02	0.09	0.06	0.11	0.00	0.06	0.12	0.00	0.00	0.00	0.00	0.00
Na_2O	1.44	1.43	1.49	2.27	1.52	2.58	1.50	2.71	1.73	1.57	4.83	1.51	1.48	2.47	2.57	1.58
K_2O	0.05	0.04	0.01	0.02	0.05	0.04	0.03	0.01	0.02	0.04	0.15	0.03	0.02	0.04	0.03	0.05
Total	100.31	97.74	98.84	99.18	99.12	99.75	99.73	99.83	98.25	99.66	100.58	98.46	97.89	98.84	98.38	99.26
Si	2.12	2.13	2.14	2.21	2.14	2.21	2.13	2.23	2.16	2.13	2.42	2.15	2.14	2.22	2.25	2.16
Ti	0.00	0.00	0.00	0.00	0.00	0.01	0.00	0.00	0.00	0.00	0.00	0.00	0.00	0.01	0.00	0.00
Fe3+	0.02	0.02	0.01	0.02	0.01	0.02	0.02	0.02	0.02	0.02	0.03	0.02	0.02	0.02	0.02	0.02
Mg	0.02	0.01	0.01	0.02	0.01	0.02	0.01	0.02	0.02	0.02	0.01	0.01	0.01	0.01	0.02	0.02
Ca	0.94	0.90	0.86	0.82	0.90	0.83	0.92	0.83	0.88	0.92	0.62	0.87	0.89	0.81	0.78	0.87
Sr	0.00	0.00	0.00	0.00	0.00	0.00	0.00	0.00	0.00	0.00	0.00	0.00	0.00	0.00	0.00	0.00
Ba	0.00	0.00	0.00	0.00	0.00	0.00	0.00	0.00	0.00	0.00	0.00	0.00	0.00	0.00	0.00	0.00
Na	0.13	0.13	0.14	0.20	0.14	0.23	0.14	0.24	0.16	0.14	0.43	0.14	0.14	0.22	0.23	0.14
K	0.00	0.00	0.00	0.00	0.00	0.00	0.00	0.00	0.00	0.00	0.01	0.00	0.00	0.00	0.00	0.00
Sum (cat)	5.03	5.02	5.00	5.01	5.02	5.03	5.02	5.04	5.02	5.03	5.03	5.01	5.01	5.01	5.00	5.01
Ab	12.05	12.69	13.44	19.97	13.12	21.73	12.80	22.63	15.18	13.26	40.27	13.53	13.22	21.57	22.96	13.98
An	87.69	86.77	86.31	79.92	86.56	77.89	86.96	77.15	84.68	86.40	58.73	86.27	86.69	78.20	76.89	85.74
Or	0.26	0.24	0.05	0.11	0.29	0.22	0.15	0.04	0.14	0.24	0.81	0.20	0.09	0.23	0.16	0.28

* Measurement used in core to rim comparisons

APPENDIX C. Continues…

Grain	PL-10-1			PL-9-1		PL-1				PL-3a				PL-3b		PL-5	
Spot	plg53	plg54	plg55	plg57	plg58	plg266	plg269	plg267	plg271	plg272	plg273	plg279	plg280	plg278	plg281	plg282	plg283
Location	Core*	Mid	Rim*	Core*	Rim*	Mid	Mid	Rim	Rim*	Core*	Mid	Core*	Mid	Rim	Rim*	Core*	Mid
SiO_2	46.81	45.91	51.09	46.51	51.11	47.51	46.98	51.50	47.79	47.99	46.45	46.34	46.24	45.19	49.29	45.70	44.87
TiO_2	0.00	0.00	0.15	0.08	0.00	0.11	0.02	0.10	0.00	0.03	0.00	0.00	0.11	0.03	0.00	0.00	0.00
Al_2O_3	32.62	33.08	29.40	33.24	29.90	32.10	32.69	29.46	32.89	33.29	32.47	32.51	32.51	32.51	31.05	32.60	32.78
Fe_2O_3	0.45	0.46	0.73	0.45	0.75	0.45	0.35	0.74	0.45	0.35	0.29	0.40	0.49	0.48	0.95	0.46	0.37
MgO	0.22	0.24	0.21	0.23	0.22	0.25	0.22	0.20	0.55	0.18	0.21	0.23	0.21	0.20	0.27	0.19	0.21
CaO	17.85	18.07	13.66	17.13	14.29	16.32	17.50	13.63	17.86	17.69	17.47	18.60	18.40	18.53	15.21	18.01	18.32
SrO	0.00	0.00	0.00	0.00	0.00	0.00	0.04	0.00	0.00	0.00	0.06	0.00	0.00	0.02	0.00	0.01	0.00
BaO	0.09	0.06	0.02	0.02	0.00	0.00	0.09	0.01	0.08	0.00	0.13	0.13	0.04	0.05	0.00	0.20	0.00
Na_2O	1.99	1.45	3.99	1.54	3.89	2.01	1.73	3.82	1.74	1.97	1.82	1.77	1.66	1.39	2.86	1.64	1.34
K_2O	0.05	0.02	0.08	0.05	0.11	0.00	0.02	0.08	0.05	0.01	0.00	0.03	0.04	0.02	0.03	0.02	0.03
Total	100.08	99.30	99.33	99.24	100.27	98.76	99.63	99.56	101.42	101.51	98.89	100.02	99.70	98.42	99.67	98.84	97.91
Si	2.16	2.14	2.35	2.16	2.33	2.21	2.17	2.36	2.17	2.18	2.17	2.15	2.15	2.13	2.27	2.14	2.12
Ti	0.00	0.00	0.01	0.00	0.00	0.00	0.00	0.00	0.00	0.00	0.00	0.00	0.00	0.00	0.00	0.00	0.00
Fe3+	0.02	0.02	0.03	0.02	0.03	0.02	0.01	0.03	0.02	0.01	0.01	0.01	0.02	0.02	0.03	0.02	0.01
Mg	0.02	0.02	0.01	0.02	0.02	0.02	0.02	0.01	0.04	0.01	0.02	0.02	0.02	0.01	0.02	0.01	0.02
Ca	0.88	0.90	0.67	0.85	0.70	0.81	0.87	0.67	0.87	0.86	0.87	0.92	0.92	0.94	0.75	0.90	0.93
Sr	0.00	0.00	0.00	0.00	0.00	0.00	0.00	0.00	0.00	0.00	0.00	0.00	0.00	0.00	0.00	0.00	0.00
Ba	0.00	0.00	0.00	0.00	0.00	0.00	0.00	0.00	0.00	0.00	0.00	0.00	0.00	0.00	0.00	0.00	0.00
Na	0.18	0.13	0.36	0.14	0.34	0.18	0.16	0.34	0.15	0.17	0.16	0.16	0.15	0.13	0.26	0.15	0.12
K	0.00	0.00	0.01	0.00	0.01	0.00	0.00	0.01	0.00	0.00	0.00	0.00	0.00	0.00	0.00	0.00	0.00
Sum (cat)	5.03	5.02	5.02	5.00	5.03	4.99	5.01	5.00	5.02	5.01	5.02	5.04	5.03	5.03	5.01	5.03	5.02
Ab	16.68	12.63	34.43	13.96	32.81	18.24	15.11	33.49	14.94	16.74	15.78	14.62	14.01	11.93	25.35	14.11	11.68
An	82.89	87.12	65.10	85.71	66.59	81.76	84.54	66.02	84.62	83.23	83.84	84.99	85.71	87.82	74.46	85.42	88.16
Or	0.28	0.14	0.44	0.29	0.59	0.00	0.11	0.47	0.30	0.03	0.00	0.18	0.21	0.12	0.19	0.09	0.17

* Measurement used in core to rim comparisons

APPENDIX C. Continues…

Grain	PL-7					PL-14			PL-8							
Spot	plg286	plg291	plg292	plg287	plg290	plg314	plg315	plg317	plg295	plg296	plg297	plg298	plg299	plg301	plg302	plg303
Location	Core*	Core	Mid	Mid	Rim*	Core*	Mid	Rim*	Core*	Mid	Mid				Rim	Rim*
SiO_2	47.51	46.97	47.91	46.11	44.86	46.97	46.64	47.01	47.82	48.57	48.68	49.09	45.88	47.91	48.49	49.15
TiO_2	0.05	0.00	0.21	0.00	0.02	0.11	0.00	0.00	0.00	0.00	0.00	0.10	0.00	0.00	0.10	0.05
Al_2O_3	31.73	31.72	31.60	31.18	33.12	32.83	32.80	33.11	30.73	31.24	31.19	31.36	32.80	33.27	30.91	29.89
Fe_2O_3	0.46	0.45	0.46	0.52	0.39	0.33	0.43	0.44	0.65	0.70	0.65	0.57	0.42	0.47	0.54	0.77
MgO	0.26	0.25	0.23	0.36	0.19	0.20	0.22	0.20	0.13	0.18	0.15	0.18	0.23	0.28	0.29	0.35
CaO	16.62	16.42	16.36	16.38	17.96	17.99	17.99	19.32	15.43	16.14	16.62	15.21	17.32	17.41	15.91	14.62
SrO	0.00	0.05	0.00	0.00	0.00	0.00	0.00	0.04	0.00	0.00	0.00	0.00	0.00	0.00	0.00	0.04
BaO	0.01	0.08	0.01	0.00	0.00	0.00	0.09	0.11	0.00	0.00	0.00	0.10	0.03	0.07	0.04	0.00
Na_2O	2.17	1.98	2.21	2.05	1.16	1.73	1.52	1.58	2.53	2.44	2.69	2.55	1.54	1.91	2.46	3.09
K_2O	0.07	0.06	0.01	0.00	0.02	0.05	0.03	0.01	0.06	0.09	0.05	0.05	0.02	0.03	0.01	0.04
Total	98.88	97.98	99.00	96.60	97.72	100.22	99.73	101.82	97.36	99.36	100.03	99.19	98.25	101.35	98.75	98.01
Si	2.21	2.20	2.22	2.20	2.12	2.16	2.16	2.14	2.25	2.24	2.24	2.26	2.15	2.18	2.25	2.30
Ti	0.00	0.00	0.01	0.00	0.00	0.00	0.00	0.00	0.00	0.00	0.00	0.00	0.00	0.00	0.00	0.00
Fe3+	0.02	0.02	0.02	0.02	0.01	0.01	0.02	0.02	0.02	0.02	0.02	0.02	0.02	0.02	0.02	0.03
Mg	0.02	0.02	0.02	0.03	0.01	0.01	0.02	0.01	0.01	0.01	0.01	0.01	0.02	0.02	0.02	0.02
Ca	0.83	0.83	0.81	0.84	0.91	0.89	0.89	0.94	0.78	0.80	0.82	0.75	0.87	0.85	0.79	0.73
Sr	0.00	0.00	0.00	0.00	0.00	0.00	0.00	0.00	0.00	0.00	0.00	0.00	0.00	0.00	0.00	0.00
Ba	0.00	0.00	0.00	0.00	0.00	0.00	0.00	0.00	0.00	0.00	0.00	0.00	0.00	0.00	0.00	0.00
Na	0.20	0.18	0.20	0.19	0.11	0.15	0.14	0.14	0.23	0.22	0.24	0.23	0.14	0.17	0.22	0.28
K	0.00	0.00	0.00	0.00	0.00	0.00	0.00	0.00	0.00	0.01	0.00	0.00	0.00	0.00	0.00	0.00
Sum (cat)	5.01	5.00	5.00	5.02	5.01	5.02	5.01	5.03	5.00	5.01	5.03	4.99	5.01	5.01	5.00	5.01
Ab	19.00	17.83	19.65	18.49	10.41	14.75	13.21	12.83	22.83	21.37	22.56	23.14	13.87	16.51	21.80	27.58
An	80.60	81.57	80.26	81.51	89.47	84.95	86.43	86.82	76.81	78.10	77.14	76.37	85.95	83.19	78.04	72.06
Or	0.38	0.33	0.07	0.00	0.12	0.30	0.19	0.06	0.37	0.53	0.30	0.32	0.13	0.19	0.08	0.26

* Measurement used in core to rim comparisons

APPENDIX C. Continues…

Grain	PL-12						PL-16							GM1	GM2	GM3
Spot	plg307	plg310	plg311	plg308	plg312	plg313	plg322	plg323	plg335	plg334	plg326	plg327	plg328	plg40	plg51	plg56
Location	Core*		Mid	Rim	Rim	Rim*	Core*	Mid		Mid		Rim	Rim*			
SiO_2	45.43	45.20	45.33	45.29	45.43	46.32	46.99	45.96	46.05	45.91	46.32	48.57	49.15	46.99	48.30	48.33
TiO_2	0.10	0.00	0.06	0.03	0.00	0.14	0.08	0.06	0.00	0.00	0.06	0.00	0.11	0.00	0.00	0.01
Al_2O_3	33.33	32.91	32.73	32.91	33.30	32.65	34.04	33.64	33.78	34.03	33.77	31.69	31.31	32.24	31.52	31.09
Fe_2O_3	0.46	0.41	0.39	0.32	0.44	0.44	0.58	0.48	0.44	0.44	0.46	0.53	0.58	0.41	0.76	0.63
MgO	0.18	0.18	0.18	0.22	0.23	0.23	0.21	0.15	0.16	0.13	0.18	0.25	0.28	0.24	0.23	0.57
CaO	18.00	17.61	17.90	17.72	17.87	17.44	18.46	18.65	18.61	18.48	18.79	16.29	16.38	17.06	15.30	15.61
SrO	0.00	0.00	0.00	0.00	0.00	0.00	0.00	0.00	0.00	0.00	0.00	0.00	0.00	0.00	0.00	0.00
BaO	0.00	0.00	0.00	0.20	0.05	0.19	0.16	0.00	0.15	0.17	0.00	0.00	0.00	0.04	0.00	0.09
Na_2O	1.25	1.29	1.40	1.24	1.33	1.63	1.44	1.20	1.18	1.12	1.24	1.97	2.72	1.99	2.55	2.51
K_2O	0.04	0.05	0.00	0.03	0.02	0.00	0.00	0.00	0.03	0.05	0.00	0.02	0.05	0.05	0.05	0.04
Total	98.79	97.65	98.00	97.97	98.66	99.04	101.96	100.15	100.41	100.34	100.83	99.32	100.59	99.02	98.71	98.88
Si	2.12	2.13	2.14	2.13	2.13	2.16	2.13	2.12	2.12	2.12	2.12	2.24	2.25	2.19	2.24	2.24
Ti	0.00	0.00	0.00	0.00	0.00	0.01	0.00	0.00	0.00	0.00	0.00	0.00	0.00	0.00	0.00	0.00
Fe3+	0.02	0.01	0.01	0.01	0.02	0.02	0.02	0.02	0.02	0.02	0.02	0.02	0.02	0.01	0.03	0.02
Mg	0.01	0.01	0.01	0.02	0.02	0.02	0.01	0.01	0.01	0.01	0.01	0.02	0.02	0.02	0.02	0.04
Ca	0.90	0.89	0.90	0.90	0.90	0.87	0.90	0.92	0.92	0.91	0.92	0.81	0.80	0.85	0.76	0.78
Sr	0.00	0.00	0.00	0.00	0.00	0.00	0.00	0.00	0.00	0.00	0.00	0.00	0.00	0.00	0.00	0.00
Ba	0.00	0.00	0.00	0.00	0.00	0.00	0.00	0.00	0.00	0.00	0.00	0.00	0.00	0.00	0.00	0.00
Na	0.11	0.12	0.13	0.11	0.12	0.15	0.13	0.11	0.11	0.10	0.11	0.18	0.24	0.18	0.23	0.23
K	0.00	0.00	0.00	0.00	0.00	0.00	0.00	0.00	0.00	0.00	0.00	0.00	0.00	0.00	0.00	0.00
Sum (cat)	5.01	5.00	5.01	5.00	5.01	5.01	5.01	5.01	5.01	5.01	5.01	4.98	5.02	5.02	5.00	5.01
Ab	11.14	11.69	12.42	11.19	11.88	14.41	12.36	10.44	10.25	9.85	10.70	17.95	23.08	17.35	23.11	22.48
An	88.64	88.01	87.58	88.26	87.94	85.24	87.37	89.56	89.31	89.55	89.29	81.96	76.65	82.31	76.59	77.15
Or	0.22	0.31	0.00	0.19	0.10	0.00	0.00	0.00	0.17	0.29	0.01	0.09	0.26	0.27	0.31	0.21

* Measurement used in core to rim comparisons

APPENDIX D. Microprobe analyses of plagioclase phenocrysts and groundmass plagioclase grains of sample AL-T026E.

Grain	PL-3-1		PL-4-1	PL-9-1		PL-8-1		PL-7-1				PL-5-1				PL-1-1	
Spot	plg1	plg2	plg31	plg4	plg26	plg5	plg27	plg6	plg7	plg8	plg9	plg10	plg11	plg12	plg13	plg14	plg15
Location	Core*	Rim*	Core*	Core*	Rim*	Core*	Core	Core*		Rim	Rim*	Core*	Core	Rim*	Rim*	Core*	
SiO_2	46.00	45.41	46.35	49.54	49.18	46.46	47.28	46.88	45.82	49.96	48.48	45.97	45.24	48.25	46.55	47.04	48.20
TiO_2	0.05	0.00	0.00	0.02	0.04	0.06	0.00	0.00	0.13	0.00	0.00	0.00	0.08	0.00	0.01	0.03	0.00
Al_2O_3	32.92	32.84	32.58	30.32	30.81	32.08	32.39	31.33	31.83	29.75	29.76	32.64	32.97	30.52	32.39	32.20	30.45
Fe_2O_3	0.57	0.38	0.77	0.72	0.77	0.46	0.48	0.56	0.48	0.62	0.84	0.45	0.33	0.77	0.55	0.49	0.65
MgO	0.10	0.12	0.16	0.18	0.19	0.18	0.18	0.23	0.15	0.20	0.24	0.18	0.16	0.21	0.12	0.17	0.21
CaO	17.38	16.79	16.89	14.13	14.83	16.84	17.10	15.64	16.17	14.20	14.53	16.72	17.26	14.98	17.04	16.72	15.23
SrO	0.00	0.00	0.05	0.00	0.06	0.00	0.00	0.14	0.00	0.00	0.00	0.00	0.00	0.03	0.00	0.00	0.00
BaO	0.00	0.00	0.00	0.00	0.05	0.00	0.00	0.13	0.01	0.07	0.11	0.28	0.00	0.06	0.03	0.06	0.03
Na_2O	1.60	1.43	1.77	3.47	3.13	2.04	2.12	2.39	1.88	3.76	3.28	1.61	1.40	3.05	1.92	2.10	3.01
K_2O	0.06	0.03	0.03	0.15	0.10	0.04	0.04	0.00	0.08	0.11	0.09	0.02	0.06	0.07	0.04	0.02	0.05
Total	98.67	97.01	98.59	98.52	99.15	98.16	99.59	97.32	96.55	98.68	97.33	97.87	97.50	97.94	98.66	98.84	97.82
Si	2.15	2.15	2.17	2.30	2.27	2.18	2.19	2.22	2.18	2.32	2.29	2.16	2.14	2.26	2.17	2.19	2.26
Ti	0.00	0.00	0.00	0.00	0.00	0.00	0.00	0.00	0.01	0.00	0.00	0.00	0.00	0.00	0.00	0.00	0.00
Fe3+	0.02	0.01	0.03	0.03	0.03	0.02	0.02	0.02	0.02	0.02	0.03	0.02	0.01	0.03	0.02	0.02	0.02
Mg	0.01	0.01	0.01	0.01	0.01	0.01	0.01	0.02	0.01	0.01	0.02	0.01	0.01	0.02	0.01	0.01	0.02
Ca	0.87	0.85	0.85	0.70	0.73	0.85	0.85	0.79	0.83	0.71	0.73	0.84	0.87	0.75	0.85	0.83	0.77
Sr	0.00	0.00	0.00	0.00	0.00	0.00	0.00	0.00	0.00	0.00	0.00	0.00	0.00	0.00	0.00	0.00	0.00
Ba	0.00	0.00	0.00	0.00	0.00	0.00	0.00	0.00	0.00	0.00	0.00	0.01	0.00	0.00	0.00	0.00	0.00
Na	0.15	0.13	0.16	0.31	0.28	0.19	0.19	0.22	0.17	0.34	0.30	0.15	0.13	0.28	0.17	0.19	0.27
K	0.00	0.00	0.00	0.01	0.01	0.00	0.00	0.00	0.01	0.01	0.01	0.00	0.00	0.00	0.00	0.00	0.00
Sum (cat)	5.01	4.99	5.01	5.02	5.02	5.02	5.02	5.01	5.00	5.03	5.03	5.00	5.00	5.02	5.01	5.01	5.02
Ab	14.20	13.35	15.87	30.48	27.41	17.97	18.25	21.54	17.27	32.19	28.78	14.75	12.75	26.80	16.88	18.48	26.27
An	85.47	86.48	83.85	68.63	71.79	81.82	81.49	77.84	82.25	67.09	70.50	84.61	86.88	72.61	82.81	81.31	73.42
Or	0.33	0.17	0.15	0.88	0.55	0.21	0.25	0.00	0.47	0.60	0.52	0.12	0.37	0.41	0.26	0.11	0.26

* Measurement used in core to rim comparisons

APPENDIX D. Continues…

Grain	PL-11-1		PL-13-1		PL-1		PL-2				PL-2b	PL-3a						PL-3b
Spot	plg16	plg17	plg18	plg19	plg258	plg259	plg20	plg21	plg22	plg23	plg255	plg241	plg242	plg243	plg244	plg245	plg246	plg247
Location	Core*	Rim*	Mid	Core*	Core*	Mid	Core*		Rim	Rim*	Core	Core	Mid				Rim*	Core*
SiO_2	45.80	45.65	50.50	51.10	45.80	50.57	47.56	47.45	49.55	49.09	48.92	51.51	46.99	47.73	50.46	47.43	51.20	52.15
TiO_2	0.00	0.00	0.12	0.00	0.00	0.00	0.09	0.02	0.00	0.00	0.00	0.10	0.04	0.00	0.00	0.00	0.10	0.03
Al_2O_3	33.01	33.15	30.15	29.46	33.05	29.97	31.75	32.27	30.95	31.24	31.26	29.38	32.42	32.00	30.10	32.56	29.47	29.37
Fe_2O_3	0.59	0.62	0.82	0.79	0.50	0.85	0.72	0.63	0.76	0.88	0.88	0.62	0.77	0.81	0.72	0.61	0.96	0.73
MgO	0.15	0.16	0.19	0.25	0.21	0.22	0.14	0.19	0.26	0.22	0.25	0.22	0.06	0.10	0.23	0.15	0.26	0.21
CaO	17.91	18.23	14.40	13.67	17.23	14.55	16.75	16.85	15.28	16.09	15.77	14.09	16.16	16.39	13.58	16.27	13.37	13.13
SrO	0.00	0.00	0.00	0.00	0.00	0.00	0.00	0.00	0.00	0.00	0.00	0.00	0.00	0.00	0.00	0.08	0.00	0.00
BaO	0.00	0.08	0.00	0.02	0.07	0.00	0.00	0.01	0.00	0.04	0.08	0.00	0.18	0.10	0.00	0.00	0.00	0.05
Na_2O	1.44	1.47	3.72	3.86	1.68	3.89	2.40	2.20	3.14	2.97	3.03	4.26	2.23	2.52	3.95	2.21	4.01	4.32
K_2O	0.03	0.03	0.05	0.08	0.02	0.11	0.05	0.02	0.07	0.10	0.07	0.14	0.05	0.09	0.11	0.09	0.12	0.11
Total	98.93	99.39	99.95	99.23	98.56	100.16	99.47	99.64	100.01	100.63	100.26	100.30	98.91	99.74	99.16	99.40	99.50	100.12
Si	2.14	2.13	2.31	2.35	2.14	2.31	2.20	2.19	2.27	2.25	2.24	2.35	2.19	2.21	2.32	2.19	2.35	2.37
Ti	0.00	0.00	0.00	0.00	0.00	0.00	0.00	0.00	0.00	0.00	0.00	0.00	0.00	0.00	0.00	0.00	0.00	0.00
Fe3+	0.02	0.02	0.03	0.03	0.02	0.03	0.03	0.02	0.03	0.03	0.03	0.02	0.03	0.03	0.03	0.02	0.03	0.03
Mg	0.01	0.01	0.01	0.02	0.02	0.02	0.01	0.01	0.02	0.02	0.02	0.02	0.00	0.01	0.02	0.01	0.02	0.01
Ca	0.90	0.91	0.71	0.67	0.86	0.71	0.83	0.83	0.75	0.79	0.78	0.69	0.81	0.81	0.67	0.81	0.66	0.64
Sr	0.00	0.00	0.00	0.00	0.00	0.00	0.00	0.00	0.00	0.00	0.00	0.00	0.00	0.00	0.00	0.00	0.00	0.00
Ba	0.00	0.00	0.00	0.00	0.00	0.00	0.00	0.00	0.00	0.00	0.00	0.00	0.00	0.00	0.00	0.00	0.00	0.00
Na	0.13	0.13	0.33	0.34	0.15	0.35	0.22	0.20	0.28	0.26	0.27	0.38	0.20	0.23	0.35	0.20	0.36	0.38
K	0.00	0.00	0.00	0.01	0.00	0.01	0.00	0.00	0.00	0.01	0.00	0.01	0.00	0.01	0.01	0.01	0.01	0.01
Sum (cat)	5.01	5.02	5.02	5.01	5.02	5.04	5.02	5.02	5.02	5.03	5.03	5.04	5.01	5.03	5.03	5.01	5.02	5.02
Ab	12.65	12.66	31.73	33.65	14.99	32.38	20.56	19.12	26.98	24.87	25.64	35.07	19.86	21.63	34.24	19.60	34.95	37.06
An	87.16	87.02	67.96	65.85	84.77	67.00	79.16	80.76	72.62	74.50	73.85	64.16	79.50	77.67	65.11	79.65	64.38	62.21
Or	0.19	0.17	0.30	0.48	0.11	0.63	0.28	0.11	0.41	0.56	0.38	0.77	0.32	0.52	0.65	0.54	0.66	0.65

* Measurement used in core to rim comparisons

APPENDIX D. Continues…

Grain	PL-5a															
Spot	plg201	plg202	plg203	plg204	plg205	plg206	plg207	plg208	plg209	plg210	plg211	plg212	plg214	plg215	plg216	plg217
Location	Core*											Mid				Rim
SiO_2	46.38	45.86	45.60	45.82	45.83	45.85	46.07	46.10	46.18	46.21	45.67	45.69	51.10	47.38	47.79	47.85
TiO_2	0.00	0.07	0.00	0.02	0.05	0.16	0.00	0.02	0.05	0.03	0.00	0.00	0.00	0.00	0.00	0.00
Al_2O_3	33.17	33.80	33.41	33.67	33.52	33.55	33.60	33.47	33.53	33.65	33.63	33.85	30.31	32.56	32.17	32.32
Fe_2O_3	0.57	0.53	0.52	0.51	0.57	0.54	0.54	0.52	0.55	0.55	0.56	0.45	0.54	0.51	0.56	0.93
MgO	0.19	0.14	0.14	0.15	0.14	0.18	0.17	0.14	0.12	0.11	0.16	0.13	0.25	0.19	0.21	0.14
CaO	17.94	17.95	18.56	18.86	18.33	18.35	18.10	18.55	18.34	18.15	18.53	17.80	14.86	17.55	17.13	17.02
SrO	0.00	0.00	0.00	0.00	0.00	0.00	0.00	0.00	0.00	0.04	0.00	0.00	0.00	0.05	0.00	0.00
BaO	0.08	0.04	0.09	0.18	0.05	0.00	0.20	0.00	0.19	0.06	0.04	0.13	0.04	0.02	0.00	0.05
Na_2O	1.67	1.57	1.38	1.44	1.43	1.43	1.57	1.54	1.65	1.52	1.42	1.43	3.85	2.22	2.42	2.53
K_2O	0.02	0.03	0.00	0.04	0.02	0.00	0.02	0.00	0.03	0.00	0.03	0.00	0.10	0.04	0.07	0.06
Total	100.01	99.99	99.71	100.69	99.93	100.07	100.27	100.34	100.64	100.32	100.04	99.47	101.04	100.53	100.35	100.90
Si	2.14	2.12	2.12	2.11	2.12	2.12	2.13	2.13	2.13	2.13	2.11	2.12	2.32	2.18	2.20	2.19
Ti	0.00	0.00	0.00	0.00	0.00	0.01	0.00	0.00	0.00	0.00	0.00	0.00	0.00	0.00	0.00	0.00
Fe3+	0.02	0.02	0.02	0.02	0.02	0.02	0.02	0.02	0.02	0.02	0.02	0.02	0.02	0.02	0.02	0.03
Mg	0.01	0.01	0.01	0.01	0.01	0.01	0.01	0.01	0.01	0.01	0.01	0.01	0.02	0.01	0.02	0.01
Ca	0.89	0.89	0.92	0.93	0.91	0.91	0.90	0.92	0.90	0.90	0.92	0.89	0.72	0.86	0.84	0.83
Sr	0.00	0.00	0.00	0.00	0.00	0.00	0.00	0.00	0.00	0.00	0.00	0.00	0.00	0.00	0.00	0.00
Ba	0.00	0.00	0.00	0.00	0.00	0.00	0.00	0.00	0.00	0.00	0.00	0.00	0.00	0.00	0.00	0.00
Na	0.15	0.14	0.12	0.13	0.13	0.13	0.14	0.14	0.15	0.14	0.13	0.13	0.34	0.20	0.22	0.22
K	0.00	0.00	0.00	0.00	0.00	0.00	0.00	0.00	0.00	0.00	0.00	0.00	0.01	0.00	0.00	0.00
Sum (cat)	5.02	5.02	5.02	5.03	5.02	5.02	5.02	5.03	5.03	5.02	5.03	5.01	5.04	5.03	5.03	5.04
Ab	14.37	13.65	11.83	12.08	12.34	12.37	13.50	13.04	13.95	13.16	12.17	12.65	31.71	18.57	20.25	21.11
An	85.40	86.09	88.01	87.37	87.48	87.64	86.06	86.95	85.59	86.65	87.60	87.12	67.68	81.05	79.36	78.49
Or	0.09	0.18	0.00	0.25	0.09	0.00	0.10	0.01	0.14	0.00	0.17	0.00	0.54	0.20	0.40	0.32

* Measurement used in core to rim comparisons

APPENDIX D. Continues…

Grain	PL-4c			PL-5b			PL-6			PL-7	PL-11	PL-14		PL-15	GM1	GM2	GM3	Ol1
Spot	plg228	plg229	plg225	plg226	plg227	plg248	plg249	plg250	plg251	plg262	plg24	plg25	plg29	plg30	plg252	plg257	plg3	
Location	Core*	Rim*	Core*	Mid	Rim*	Core*	Mid	Rim*	Core*		Mid	Rim*	Rim*				inclusion	
SiO_2	46.61	49.10	45.58	47.55	49.26	46.83	46.38	49.21	48.55	47.49	46.03	49.05	50.35	49.44	49.95	45.67	49.37	
TiO_2	0.06	0.00	0.01	0.00	0.10	0.03	0.00	0.07	0.12	0.04	0.02	0.00	0.08	0.10	0.00	0.00	0.01	
Al_2O_3	32.70	31.08	33.36	32.42	30.34	32.33	33.18	31.11	31.51	31.78	33.07	31.15	29.70	30.05	30.27	33.38	29.66	
Fe_2O_3	0.54	0.68	0.50	0.54	0.95	1.01	0.50	0.77	0.70	0.78	0.59	0.73	0.82	0.96	1.13	0.60	0.95	
MgO	0.15	0.16	0.23	0.20	0.55	0.50	0.14	0.17	0.17	0.24	0.17	0.17	0.25	0.04	0.16	0.16	0.32	
CaO	17.29	15.13	17.77	17.27	15.41	16.58	16.68	14.47	15.60	16.04	17.83	15.68	14.46	14.15	14.39	17.23	13.80	
SrO	0.00	0.00	0.00	0.00	0.00	0.00	0.00	0.00	0.00	0.00	0.00	0.00	0.00	0.00	0.00	0.00	0.00	
BaO	0.00	0.00	0.17	0.00	0.02	0.04	0.01	0.00	0.00	0.24	0.00	0.00	0.01	0.00	0.04	0.03	0.00	
Na_2O	1.91	3.29	1.43	2.24	3.03	2.06	1.74	3.29	2.82	2.47	1.57	2.96	3.56	3.61	3.78	1.63	3.50	
K_2O	0.03	0.09	0.02	0.05	0.05	0.08	0.05	0.02	0.11	0.05	0.03	0.07	0.08	0.15	0.12	0.05	0.08	
Total	99.29	99.52	99.07	100.26	99.72	99.45	98.68	99.10	99.57	99.12	99.30	99.81	99.32	98.51	99.85	98.75	97.69	
Si	2.16	2.26	2.13	2.19	2.27	2.17	2.16	2.27	2.24	2.21	2.14	2.26	2.32	2.30	2.30	2.13	2.31	
Ti	0.00	0.00	0.00	0.00	0.00	0.00	0.00	0.00	0.00	0.00	0.00	0.00	0.00	0.00	0.00	0.00	0.00	
Fe3+	0.02	0.02	0.02	0.02	0.03	0.04	0.02	0.03	0.02	0.03	0.02	0.03	0.03	0.03	0.04	0.02	0.03	
Mg	0.01	0.01	0.02	0.01	0.04	0.03	0.01	0.01	0.01	0.02	0.01	0.01	0.02	0.00	0.01	0.01	0.02	
Ca	0.86	0.75	0.89	0.85	0.76	0.82	0.83	0.72	0.77	0.80	0.89	0.77	0.71	0.71	0.71	0.86	0.69	
Sr	0.00	0.00	0.00	0.00	0.00	0.00	0.00	0.00	0.00	0.00	0.00	0.00	0.00	0.00	0.00	0.00	0.00	
Ba	0.00	0.00	0.00	0.00	0.00	0.00	0.00	0.00	0.00	0.00	0.00	0.00	0.00	0.00	0.00	0.00	0.00	
Na	0.17	0.29	0.13	0.20	0.27	0.19	0.16	0.30	0.25	0.22	0.14	0.26	0.32	0.33	0.34	0.15	0.32	
K	0.00	0.01	0.00	0.00	0.00	0.00	0.00	0.00	0.01	0.00	0.00	0.00	0.01	0.01	0.01	0.00	0.01	
Sum (cat)	5.02	5.03	5.01	5.03	5.03	5.02	5.00	5.02	5.02	5.02	5.02	5.02	5.02	5.03	5.04	5.01	5.02	
Ab	16.65	28.08	12.66	18.98	26.17	18.24	15.85	29.13	24.49	21.62	13.73	25.39	30.70	31.35	31.97	14.56	31.30	
An	83.19	71.43	86.92	80.73	73.53	81.24	83.81	70.73	74.90	77.70	86.11	74.20	68.84	67.83	67.27	85.08	68.22	
Or	0.16	0.49	0.12	0.30	0.27	0.44	0.32	0.14	0.61	0.26	0.16	0.41	0.44	0.83	0.69	0.30	0.48	

* Measurement used in core to rim comparisons

APPENDIX E. Microprobe analyses of plagioclase phenocrysts and groundmass plagioclase grains of sample AL-T026G.

Grain	PL-1																	
Spot	plg161	plg162	plg163	plg166	plg167	plg168	plg169	plg170	plg171	plg172	plg173	plg174	plg175	plg176	plg177	plg178	plg179	plg180
Location	Core*																	Rim*
SiO_2	47.15	46.38	45.86	47.56	46.92	47.70	46.80	46.83	47.01	46.04	46.75	46.98	46.90	46.31	46.29	47.13	47.00	46.44
TiO_2	0.03	0.00	0.00	0.00	0.00	0.16	0.00	0.00	0.17	0.00	0.00	0.19	0.00	0.00	0.00	0.00	0.00	0.12
Al_2O_3	32.56	32.99	32.54	31.98	32.31	32.12	32.27	32.70	32.59	32.44	32.59	32.79	32.97	32.62	32.88	32.80	32.68	32.93
Fe_2O_3	0.66	0.92	0.63	0.59	0.52	0.54	0.45	0.52	0.52	0.63	0.48	0.66	0.46	0.49	0.44	0.51	0.57	0.75
MgO	0.18	0.06	0.58	0.25	0.25	0.24	0.24	0.20	0.16	0.14	0.21	0.19	0.16	0.19	0.14	0.19	0.20	0.12
CaO	17.51	18.28	17.90	17.27	17.71	16.91	16.81	17.28	17.75	17.25	16.96	17.10	17.02	17.35	17.56	17.45	17.43	17.47
SrO	0.00	0.00	0.00	0.00	0.00	0.00	0.00	0.00	0.00	0.00	0.00	0.00	0.04	0.03	0.00	0.00	0.00	0.00
BaO	0.00	0.04	0.00	0.03	0.00	0.00	0.00	0.16	0.00	0.00	0.00	0.01	0.00	0.00	0.00	0.00	0.03	0.00
Na_2O	2.24	1.67	1.58	2.31	2.18	2.29	2.09	1.99	2.00	2.01	2.04	2.07	1.91	1.93	1.89	2.03	1.98	1.89
K_2O	0.04	0.04	0.04	0.03	0.00	0.04	0.04	0.03	0.03	0.03	0.01	0.04	0.00	0.03	0.02	0.01	0.01	0.05
Total	100.37	100.37	99.13	100.01	99.88	100.02	98.70	99.72	100.22	98.54	99.06	100.04	99.46	98.96	99.23	100.13	99.90	99.77
Si	2.17	2.14	2.14	2.19	2.17	2.20	2.18	2.17	2.17	2.16	2.17	2.17	2.17	2.16	2.15	2.17	2.17	2.15
Ti	0.00	0.00	0.00	0.00	0.00	0.01	0.00	0.00	0.01	0.00	0.00	0.01	0.00	0.00	0.00	0.00	0.00	0.00
Fe3+	0.02	0.03	0.02	0.02	0.02	0.02	0.02	0.02	0.02	0.02	0.02	0.02	0.02	0.02	0.02	0.02	0.02	0.03
Mg	0.01	0.00	0.04	0.02	0.02	0.02	0.02	0.01	0.01	0.01	0.02	0.01	0.01	0.01	0.01	0.01	0.01	0.01
Ca	0.86	0.90	0.89	0.85	0.88	0.83	0.84	0.86	0.88	0.87	0.85	0.84	0.84	0.87	0.88	0.86	0.86	0.87
Sr	0.00	0.00	0.00	0.00	0.00	0.00	0.00	0.00	0.00	0.00	0.00	0.00	0.00	0.00	0.00	0.00	0.00	0.00
Ba	0.00	0.00	0.00	0.00	0.00	0.00	0.00	0.00	0.00	0.00	0.00	0.00	0.00	0.00	0.00	0.00	0.00	0.00
Na	0.20	0.15	0.14	0.21	0.20	0.21	0.19	0.18	0.18	0.18	0.18	0.19	0.17	0.17	0.17	0.18	0.18	0.17
K	0.00	0.00	0.00	0.00	0.00	0.00	0.00	0.00	0.00	0.00	0.00	0.00	0.00	0.00	0.00	0.00	0.00	0.00
Sum (cat)	5.04	5.02	5.03	5.03	5.04	5.02	5.02	5.02	5.03	5.03	5.02	5.02	5.01	5.03	5.03	5.02	5.02	5.02
Ab	18.79	14.13	13.73	19.46	18.24	19.66	18.32	17.17	16.90	17.41	17.88	17.96	16.87	16.70	16.30	17.38	17.00	16.29
An	80.98	85.58	86.06	80.31	81.77	80.09	81.47	82.40	82.95	82.44	82.04	81.80	83.04	83.03	83.58	82.54	82.86	83.40
Or	0.23	0.23	0.22	0.17	0.00	0.25	0.21	0.16	0.15	0.16	0.08	0.22	0.00	0.18	0.11	0.08	0.08	0.31

* Measurement used in core to rim comparisons

APPENDIX E. Continues…

Grain	PL-2				GM2	GM3	Incl.
Spot	plg194	plg195	plg196	plg197	plg191	plg198	plg189
Location	Core*	Mid	Mid	Rim*			
SiO_2	45.81	46.26	45.83	46.48	46.27	51.71	49.74
TiO_2	0.09	0.01	0.00	0.07	0.07	0.00	0.09
Al_2O_3	33.75	33.50	33.42	32.83	32.69	29.20	30.07
Fe_2O_3	0.46	0.55	0.46	0.54	0.88	1.00	1.02
MgO	0.13	0.12	0.17	0.17	0.06	0.09	0.09
CaO	17.71	17.27	17.12	16.92	17.09	13.89	14.18
SrO	0.00	0.00	0.00	0.00	0.08	0.03	0.00
BaO	0.04	0.00	0.10	0.09	0.00	0.00	0.07
Na_2O	1.32	1.67	1.56	1.88	2.03	4.47	3.81
K_2O	0.04	0.02	0.00	0.05	0.05	0.18	0.11
Total	99.34	99.39	98.68	99.03	99.22	100.57	99.18
Si	2.13	2.14	2.14	2.16	2.15	2.36	2.30
Ti	0.00	0.00	0.00	0.00	0.00	0.00	0.00
Fe3+	0.02	0.02	0.02	0.02	0.03	0.03	0.04
Mg	0.01	0.01	0.01	0.01	0.00	0.01	0.01
Ca	0.88	0.86	0.86	0.84	0.85	0.68	0.70
Sr	0.00	0.00	0.00	0.00	0.00	0.00	0.00
Ba	0.00	0.00	0.00	0.00	0.00	0.00	0.00
Na	0.12	0.15	0.14	0.17	0.18	0.40	0.34
K	0.00	0.00	0.00	0.00	0.00	0.01	0.01
Sum (cat)	5.00	5.01	5.01	5.01	5.03	5.05	5.03
Ab	11.81	14.88	14.16	16.64	17.57	36.41	32.44
An	87.86	85.02	85.66	82.91	81.91	62.54	66.79
Or	0.26	0.10	0.00	0.29	0.31	0.96	0.64

* Measurement used in core to rim comparisons

APPENDIX F. Microprobe analyses of groundmass plagioclase grains of sample AL-T042.

Grain	GM6		GM7		GM8		GM10		GM11		GM12	
Spot	456	457	plg458	plg459	plg460	plg461	plg465	plg466	plg468	plg470	plg471	plg472
Location												
SiO_2	47.87	48.38	48.33	48.50	47.56	46.29	48.15	47.29	48.18	48.29	48.40	48.31
TiO_2	0.29	0.00	0.03	0.00	0.02	0.00	0.06	0.00	0.02	0.00	0.00	0.10
Al_2O_3	31.08	31.02	30.38	30.81	31.23	32.49	30.18	31.22	30.83	30.49	30.42	30.57
Fe_2O_3	0.91	1.07	1.18	1.20	1.17	1.17	0.96	1.05	1.03	0.90	0.92	1.10
MgO	0.26	0.25	0.30	0.19	0.23	0.09	0.41	0.26	0.31	0.33	0.29	0.29
CaO	17.52	16.69	16.20	16.42	16.00	17.99	15.87	16.98	17.02	16.37	16.75	16.45
SrO	0.00	0.00	0.00	0.00	0.00	0.00	0.00	0.02	0.00	0.00	0.00	0.00
BaO	0.10	0.05	0.05	0.00	0.07	0.13	0.17	0.02	0.08	0.17	0.10	0.13
Na_2O	2.59	2.67	3.02	2.76	2.49	1.82	3.02	2.35	2.67	2.70	2.78	2.78
K_2O	0.05	0.09	0.09	0.02	0.03	0.00	0.03	0.03	0.05	0.05	0.00	0.04
Total	100.69	100.21	99.58	99.89	98.81	99.97	98.85	99.23	100.19	99.29	99.67	99.76
Si	2.20	2.23	2.24	2.24	2.22	2.15	2.25	2.20	2.22	2.24	2.24	2.24
Ti	0.01	0.00	0.00	0.00	0.00	0.00	0.00	0.00	0.00	0.00	0.00	0.00
Fe3+	0.03	0.04	0.04	0.04	0.04	0.04	0.03	0.04	0.04	0.03	0.03	0.04
Mg	0.02	0.02	0.02	0.01	0.02	0.01	0.03	0.02	0.02	0.02	0.02	0.02
Ca	0.86	0.82	0.81	0.81	0.80	0.89	0.79	0.85	0.84	0.82	0.83	0.82
Sr	0.00	0.00	0.00	0.00	0.00	0.00	0.00	0.00	0.00	0.00	0.00	0.00
Ba	0.00	0.00	0.00	0.00	0.00	0.00	0.00	0.00	0.00	0.00	0.00	0.00
Na	0.23	0.24	0.27	0.25	0.23	0.16	0.27	0.21	0.24	0.24	0.25	0.25
K	0.00	0.01	0.01	0.00	0.00	0.00	0.00	0.00	0.00	0.00	0.00	0.00
Sum (cat)	5.05	5.03	5.05	5.03	5.02	5.03	5.04	5.03	5.04	5.03	5.04	5.03
Ab	21.02	22.34	25.08	23.33	21.92	15.42	25.46	19.96	22.00	22.84	23.04	23.30
An	78.52	77.06	74.32	76.55	77.79	84.35	74.06	79.78	77.59	76.58	76.79	76.24
Or	0.29	0.52	0.51	0.13	0.18	0.01	0.19	0.16	0.28	0.29	0.00	0.24